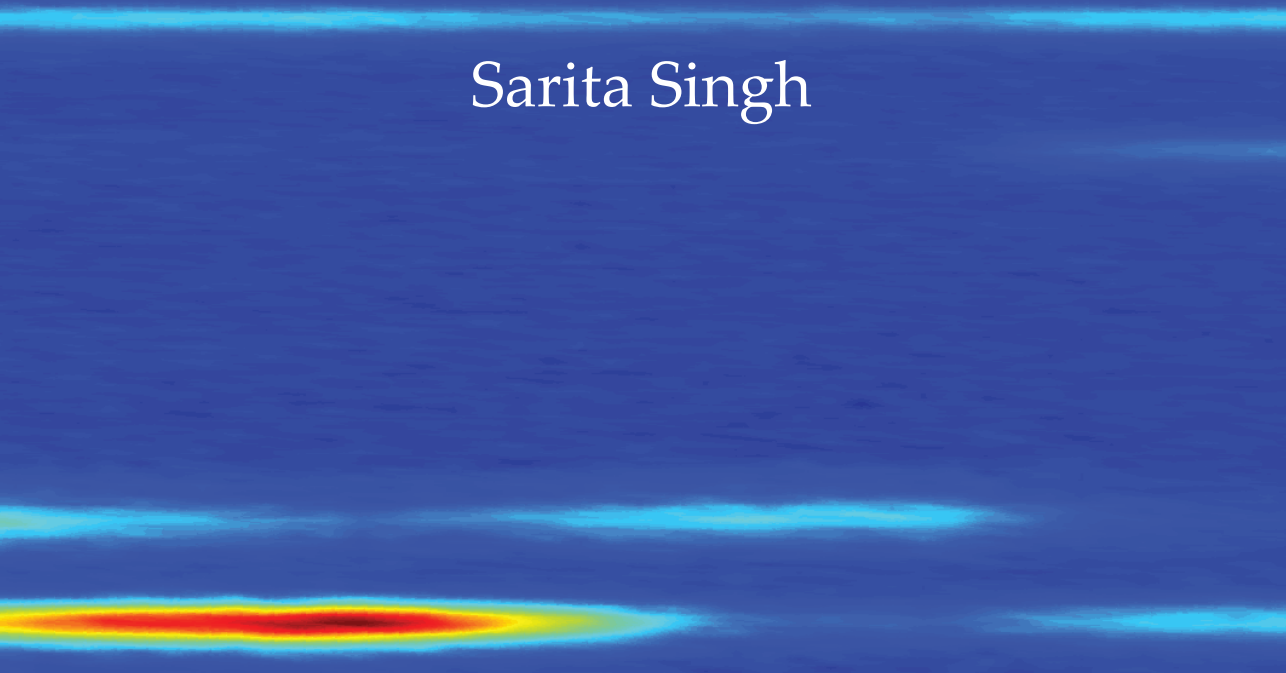


HYDROGEN STORAGE
IN
NANOSTRUCTURED
LIGHT METAL HYDRIDES

by

Sarita Singh

The background of the cover is a deep blue. It features several horizontal bands of light. A prominent, bright yellow and orange glowing spot is located near the bottom center, with a soft, cyan-colored glow extending horizontally from it. Above this, there are several thinner, horizontal bands of cyan light, spaced out vertically.

HYDROGEN STORAGE
IN
NANOSTRUCTURED LIGHT METAL HYDRIDES

This work is part of the Sustainable Hydrogen Program of the Delft Center of Sustainable Energy.

HYDROGEN STORAGE
IN
NANOSTRUCTURED LIGHT METAL HYDRIDES

PROEFSCHRIFT

ter verkrijging van de graad van doctor
aan de Technische Universiteit Delft,
op gezag van de Rector Magnificus prof. dr. ir. J.T. Fokkema,
voorzitter van het College voor Promoties,
in het openbaar te verdedigen op woensdag 6 mei 2009 om 10.00 uur

door

Sarita SINGH

Master of Science in Physics, Indian Institute of Technology Madras
geboren te Haridwar, India

DIT PROEFSCHRIFT IS GOEDGEKEURD DOOR DE PROMOTOR:

Prof. dr. F. M. Mulder

COPROMOTOR:

Dr. S.W.H. Eijt

SAMENSTELLING PROMOTIECOMMISSIE:

Rector Magnificus	Voorzitter
Prof. dr. F.M. Mulder	Technische Universiteit Delft, promotor
Dr. S.W.H. Eijt	Technische Universiteit Delft, copromotor
Prof. dr. B. Dam	Technische Universiteit Delft
Prof. dr. J.J.C. Geerlings	Technische Universiteit Delft
Prof. dr. P.H.L. Notten	Technische Universiteit Eindhoven
Prof. dr. I.M. de Schepper	Technische Universiteit Delft
Prof. dr. A. Schmidt-Ott	Technische Universiteit Delft
Prof. dr. E.H. Brück	Technische Universiteit Delft, reservelid

KEYWORDS:

Hydrogen storage, neutron diffraction, grain refinement, hydrogen vacancy, phase transformation, density functional theory.

COVER:

Neutron diffraction patterns showing the development of different phases upon heating and deuterium loading of TiCl_3 -catalyzed NaAlH_4 over time.

THIS RESEARCH WAS CARRIED OUT AT:

Fundamental Aspects of Materials and Energy
Department Radiation, Radionuclides & Reactors
Faculty of Applied Sciences
Delft University of Technology

Copyright ©2009 S. Singh

ISBN 978 90 902 4112 8

Printed in the Netherlands by Ipskamp Drukkers

To my parents

for believing in my decisions which made everything possible

Table of contents

List of abbreviations and symbols	xi
Acknowledgments	xix
1 Introduction	1
1.1 A history of hydrogen for energy	2
1.2 Need for a hydrogen economy	5
1.3 Hydrogen storage challenges	7
1.4 Aim of this thesis	9
2 Methods	15
2.1 Ball milling	15
2.2 Thin film synthesis	17
2.2.1 Sputtered deposition	17
2.2.2 Pulsed laser deposition	19
2.3 X-ray diffraction	21
2.4 Electron microscopy	23
2.5 Hydrogen release and uptake	25
2.6 Neutron diffraction	26
2.6.1 Coherent and incoherent scattering	30
2.6.2 Elastic scattering	31
2.6.3 Neutron diffractometer	34
2.6.4 GSAS	36
2.7 Ab initio calculations	39
2.7.1 Density functional theory	40
2.8 Positron depth profiling	43

3	Mg thin films	49
3.1	Experimental details	50
3.2	Plasma sputter deposited films	52
3.2.1	Structural characterization	52
3.2.2	Pd as a hydrogen splitter at the surface	54
3.2.3	Pd reduces hydrogen sorption temperatures	55
3.2.4	Storage properties	58
3.2.5	Positron analysis	60
3.3	Pulsed laser deposited films	64
3.3.1	XRD characterization	64
3.3.2	Microstructure studies	67
3.4	Conclusions	71
4	Catalyzed and uncatalyzed NaAlH₄	73
4.1	Experimental details	75
4.2	Results	77
4.2.1	Uncatalyzed NaAlH ₄	77
4.2.2	Catalyzed NaAlH ₄	81
4.3	Discussion	85
4.3.1	Effect of grain sizes on reversibility	85
4.3.2	Hydrogen vacancy formation	86
4.3.3	Grain refinement by the Ti _x Al _{1-x} and NaCl particles	89
4.3.4	Comparison with Ti-metal catalyzed NaAlH ₄	91
4.3.5	Hydrogen-deuterium exchange in NaH	94
4.4	Conclusions	95
5	Ab initio calculations on NaH	97
5.1	Computational procedure	98
5.2	Results and discussion	100
5.2.1	Migration energies and diffusion coefficients	100
5.2.2	Formation energies for a variety of defects	105
5.2.3	Mechanism for abundant vacancies in nano-NaH	107
5.3	Conclusions	111

6	Si destabilized MgH₂	113
6.1	Experimental description	116
6.2	Powder samples	117
6.3	Thin film samples	120
6.3.1	Mg ₂ Si formation in H ₂ and He atmospheres	120
6.3.2	Different pathways for Mg ₂ Si formation	123
6.3.3	Possible mechanism for the irreversibility of Mg ₂ Si	126
6.4	Conclusions	127
7	TiF₃ catalyzed MgH₂	129
7.1	Experimental procedure	130
7.2	Results	132
7.2.1	In situ neutron diffraction on TiF ₃ catalyzed Mg	132
7.3	Discussion	140
7.3.1	Role of MgF ₂ as a grain refiner	140
7.3.2	Deuterium vacancies during desorption in MgD _x	140
7.4	Conclusions	141
A	Fitted patterns on catalyzed NaAlH₄	143
B	TiF₃ catalyzed MgD₂: Fitted patterns	147
	Summary	150
	Samenvatting	156
	Bibliography	163
	List of publications	177
	About the author	179

List of abbreviations and symbols

Abbreviations

2D	Two dimensional
3D	Three dimensional
AFC	Alkaline fuel cell
bcc	Body centered cubic
CIF	Crystallographic information file
DFT	Density functional theory
DIFC	Diffractometer constant
DOE	Department of Energy
DOS	Density-of-states
EIA	Energy Information Administration
EOS	Equation of state
fcc	Face centered cubic
FIB	Focused ion beam
GE	General Electric
GEM	GEneral Materials
GGA	Generalized gradient approximation
GM	General Motors
GSAS	General structure analysis system
hcp	Hexagonal closed packed
HRTEM	High resolution TEM
IAHE	International Association of Hydrogen Energy
ICSD	Inorganic crystal structure database
IEA	International Energy Agency
LDA	Local density approximation
LPG	Liquefied petroleum gas
NHA	National Hydrogen Association
OECD	Organization for Economic Co-operation and Development
OPEC	Organization of the Petroleum Exporting Countries
o-Ps	Ortho-positronium
PAW	Projector-augmented wave
PEM	Proton exchange membrane
PLD	Pulsed laser deposition

ppm	Parts per million
PP	Pseudopotential
PSD	Plasma sputter deposition
PVD	Physical vapor deposition
QMS	Quadrupole mass spectrometer
rpm	Revolutions per minute
RT	Room temperature
SAD	Selected area diffraction
sc	Simple cubic
SE	Schrödinger equation
SEM	Scanning electron microscope
TEM	Transmission electron microscopy
TOF	Time-of-flight
US-PP	Ultra-soft pseudopotentials
VASP	Vienna ab initio simulation package
VEP	Variable energy positron
XAFS	X-ray absorption fine structure
XRD	X-ray diffraction

Chemical notation

Al	Aluminum
Al(BH ₄) ₃	Aluminum tris(tetrahydridoborate)
Al ₂ O ₃	Alumina
Ar	Argon
Au	Gold
BaReH ₉	Barium rhenium nonahydride
Cl	Chlorine
Co	Cobalt
Cu	Copper
CH ₄	Methane
CsCl	Cesium chloride
D	Deuterium atom
D ₂	Deuterium
Ga	Gallium
H	Hydrogen atom
H ₂	Hydrogen
H ₂ O	Water
He	Helium
KBH ₄	Potassium tetrahydridoborate
LaNi ₅ H ₆	Lanthanum nickel hydride
Li	Lithium
LiH	Lithium hydride

LiAlH_4	Lithium aluminum hydride
LiBH_4	Lithium tetrahydridoborate
LiTiO_x	Lithium titanium oxide
Mg	Magnesium
MgD_2	Magnesium deuteride
MgF_2	Magnesium fluoride
MgH_2	Magnesium hydride
Mg_2Ni	Magnesium nickel
MgO	Magnesium oxide
MgPd	Magnesium palladium
Mg_2Pd	Dimagnesium monopalladium
Mg_2Si	Magnesium silicide
Mg_2FeH_6	Magnesium iron hydride
Mg_2NiH_4	Magnesium nickel hydride
Na	Sodium
NaAlH_4	Sodium aluminum tetrahydride
Na_3AlH_6	Sodium aluminum hexahydride
NaBH_4	Sodium tetrahydridoborate
NaCl	Sodium chloride
NaH	Sodium hydride
Nb	Niobium
Nb_2O_5	Niobium oxide
Nd	Neodymium
Nd:YAG	Neodymium-doped yttrium aluminum garnet
NO_x	Nitrogen oxide
O	Oxygen atom
O_2	Oxygen
Pd	Palladium
PdAg	Palladium silver
$\text{PdH}_{0.7}$	Palladium hydride
Si	Silicon
Ta	Tantalum
Ti	Titanium
TiAl_3	Titanium aluminide
TiCl_3	Titanium chloride
TiF_3	Titanium fluoride
TiH_2	Titanium hydride
$\text{Ti}(\text{OBU})_4$	Tetrabutyl titanate
V	Vanadium
V_2O_5	Vanadium oxide
W	Tungsten
$\text{Y}_3\text{Al}_5\text{O}_{12}$	Yttrium aluminum garnet

Fundamental constants

c	Speed of light
h	Planck's constant
\hbar	Planck's constant divided by 2π
k_B	Boltzmann constant
N_A	Avogadro's constant

Greek symbols

Γ	Number of transitions per second between the states
δ	Dirac delta function
ϵ	Exchange correlation energy per electron
θ	Scattering angle
κ	Bulk modulus
λ	Wavelength
μ	Chemical potential
ν_0	Vibrational frequency
ζ	Diffusion correlation factor depends on the unit cell geometry
π	"Pi", the ratio of a circle's circumference to its diameter
ρ	Particle density
σ	Scattering cross-section
σ_{tot}	Total scattering cross-section
τ	Kinetic energy
Φ	Flux of incoming neutrons
χ	Concentration of defects
ψ	Wave function
Ψ	Total wave function
ω	Vibrational frequency multiplied by 2π
Ω	Solid angle in a scattering system

Latin symbols

$\mathbf{a}_1, \mathbf{a}_2, \mathbf{a}_3$	Basis vectors of a unit cell
b	Scattering length of a bound nuclei
$\mathbf{b}_1, \mathbf{b}_2, \mathbf{b}_3$	Reciprocal vectors of a unit cell
d	Interplanar spacing in a crystal
\mathbf{d}	Position vector of atoms within a unit cell
D	Diffusion coefficient
D_0	Pre-exponential factor in diffusion equation
e	Electron

e^+	Positron
E	Energy
E^f	Formation energy of a defect
ΔE_S	Energy window for the S parameter
ΔE_W	Energy window for the W parameter
f	Electron form factor
F	Structure factor of a unit cell
g	Grain size
G	Universal functional of electron density
\mathbf{G}	Reciprocal lattice vector
\hat{H}	Hamiltonian operator
ΔH	Enthalpy change
I	Number of detected neutrons per second
J_∞	Equilibrium hydrogen permeation flux
k	Force constant
\mathbf{k}	Wave vector
K	Scherrer constant
l_1, l_2, l_3	Integer multipliers of the lattice vectors
\mathbf{l}	Lattice vector of a crystal lattice
L	Distance between the moderator source and the detector
L_i	Distance between the moderator source and the sample
L_f	Distance between the sample and the detector
m	Mass
m_0	Rest mass
M	Molecular mass
n	Integer
n_a	Number of atoms
N	Number of nuclei
p	Pressure
\mathbf{p}	Momentum
q	Charge
\mathbf{Q}	Scattering vector
\mathbf{r}	Space variable
R	Radius of a grain
\mathbf{R}	Position vector of an atom in a crystal
R_w	Weighted residual in Rietveld refinement
s	Distance of an equilibrium hydrogen atom to a vacancy position
S	Shape parameter in positron analysis
\mathbf{S}	Spin of the nucleus
T	Temperature
t	Time variable
t_1, t_2, t_3	Integer multipliers of the reciprocal lattice vectors
\mathbf{u}	Thermal displacement of an atom
U	Exponent in Debye-Waller factor for isotropic thermal movement

U_{iso}	Parameter in GSAS, equals to U
v	Volume of a unit cell per atom
v_0	Volume of a unit cell
V	Interaction potential of a nucleus with another nucleus or electron
V_{bias}	Bias voltage
W	Wing parameter in positron analysis
x_d, y_d, z_d	Coordinates of an atom in a unit cell
X	Peak shape (broadening) parameter in XRD
X, Y, Z	Global coordinates
Z	Atomic number

Subscripts

c	Related to hydrogen content
cal	Related to calculated intensity
coh	Related to coherent scattering
d	Related to index of nucleus
eff	Related to effective interaction potential
f	Related to final stage in a neutron scattering event
F	Related to Fermi energy
g	Related to Band gap
H	Related to Hydrogen
hkl	Related to Miller indices
i	Related to initial stage in a neutron scattering event
I	Related to interstitial hydrogen
in	Related to input in VASP
$incoh$	Related to incoherent scattering
int	Related to interface
l	Related to index of unit cell in real space
m	Related to migration of an atom
n	Related to neutron
N	Related to number of nuclei
obs	Related to observed Intensity
out	Related to output in VASP
V	Related to hydrogen vacancy
x	Real-valued stoichiometric number
xc	Related to exchange correlation energy

Acknowledgments

Preparing this thesis involved many people—and I feel indebted to all of them. My first thanks go to Stephan Eijt for inviting me to pursue this PhD at the department of Radiation, Reactors & Radionuclides. His guidance, valuable suggestions, and appreciation gave me confidence and improved the quality of this project. I feel glad that I had the opportunity to work with Fokko Mulder. It was truly a joyful and unique learning experience. Fokko's enthusiasm, detail orientation, politeness, and cheerfulness frequently rejuvenated my interest in research. Thank you Fokko for becoming my promotor. I am grateful to the members of my examination committee for the time they dedicated reading the thesis and their valuable comments.

I am thankful to our management assistants Marianne van Baaren, Nicole Banga, and Ellen Tettelaar for taking care of all administrative tasks, which allowed me to fully concentrate on my work. I thank Walter Legerstee for solving the technical issues that I came across during the experiments. Many thanks go to Vasili Svechnikov for performing TEM measurements, the results of which put an attribute to my research work. I acknowledge the help I received from Jouke Heringa in computer related issues. I thank to Marnix Wagemaker for his help at ISIS during GEM experiments and the fruitful discussions he provided. I appreciate Yulia's helpful nature, which made me adjust quickly in my new environment when I started my PhD. Thank you Leon for your assistance in generating Matlab graphs as well as for your friendship. Further, I am thankful to Anna for refreshing the atmosphere in the office with her charming smile. *Hartelijk bedankt Lucas voor jou hulp in de vertaling van de samenvatting van deze proefschrift in het Nederlands.*

Thank you, my dear friends, Emanuela, Carmen & Carlos, Reshmi & Biju, and Marcela & Wijnand for making my stay in Delft pleasant by just being there. I cherish the time we spent together—the nice dinners, the many laughs, the games, and enjoyable outings.

I am thankful to Prof. G. Srinivasan from Raman Research Institute in Bangalore and Prof. V. Balakrishnan from Indian Institute of Technology Madras for their motivating lectures, encouraging discussions, recommendations, and confidence in me and my work.

I thank Thomas' family—his parents, Yvonne, Shahram, Yonas, and Helene—for providing me a comfortable at-home feeling far away from my native home. *Danke schön* Thomas for your company, patience, emotional support, and particularly your crucial suggestions on this book.

Last but not least, I express my gratitude to my parents for the reason I mentioned in my dedication—and for many more. I thank my brothers Akshay and Jitendra for their love, care, and constant feedback, which helped me grow professionally. I am pleased to mention my nephew Akash and niece Tanya for bringing happiness into my life at every moment I think of them.

Delft, February 2009

1

Introduction

Hydrogen is the simplest element consisting of only one proton and one electron. It is represented by the letter “H”. Hydrogen gas consists of diatomic molecules, where each of the molecules comprises two hydrogen atoms, commonly expressed as H_2 . Hydrogen exists as a gas at standard temperature and pressure. It is a colorless, odorless, tasteless gas, and it is lighter than air. Hydrogen is the most abundant element in the universe. On earth, it is mostly bound in compounds such as water, i.e., H_2O , or hydrocarbons like natural gas, which consists primarily of methane (CH_4). Hydrogen is also found in biomass, which includes all plants and animals. However, H_2 as a gas is not abundant on earth.

Like natural gas, hydrogen is an energy carrier. It can store and deliver energy in an easily usable form by burning with oxygen. Burning of hydrogen with air gives water as a by product, making it a clean fuel. Because of its high energy content, hydrogen has the potential to power cars, trucks, buses and other vehicles, homes, offices, factories, and even portable electronic equipment, such as laptops and computers. Realizing the potential of hydrogen as an energy carrier requires many discoveries, which started with the discovery of hydrogen itself.

1.1 A history of hydrogen for energy

Hydrogen was first identified by British scientist Henry Cavendish in 1766, and he called it *inflammable air*, a gas forming water (H_2O) when burned [1]. In 1783, a French chemist Antoine Lavoisier reproduced Cavendish's findings that water is produced on burning the *inflammable air*, and named the gas as *Hydrogen* [2,3]. The name Hydrogen was derived from the Greek words—*hydro* and *genes*, meaning *water* and *born of*, respectively. The discovery that hydrogen weighs fourteen times lighter than air made scientists interested to use hydrogen as a buoyant in aeronautical balloons. Alexandre Cesar Charles, a French scientist, used hydrogen to fill a balloon for a manned flight in the same year, i.e., 1783. This flight was the first manned flight in a hydrogen filled balloon [4].

In 1800, the splitting of water into H_2 and O_2 with electricity was discovered by William Nicholson, an English chemist, by placing the leads from a battery into H_2O , while attempting to reproduce the electric battery invented by the Italian physicist Alessandro Volta. This phenomenon was named as *electrolysis*. Nicholson became the first man to produce a chemical reaction by electricity [5]. This discovery forced Sir William Grove to think reverse of the electrolysis, to generate electricity from the reaction of O_2 with H_2 , should also be possible. His thought led to the discovery of the first *fuel cell* in 1839, which later made him famous as the Father of the Fuel Cell. However, the term *fuel cell* was later coined in 1889 by chemists Ludwig Mond and Charles Langer, as they attempted to build the first practical device using air and industrial coal gas [4,6].

In 1923, a paper by the Scottish scientist J.B.S. Haldane ignited a practical interest in hydrogen as a fuel in Europe after World War I. This paper offered the first proposal of the hydrogen-based renewable energy economy. Haldane emphasized the probable scarcity of fossil fuels and the eventual necessity of an alternative source of energy at a time when the use of fossil fuels, especially coal was popular [7]. He also pointed out that liquid hydrogen produces three times as much heat per pound as petrol (hydrocarbon fuel). He also mentioned that hydrogen would be a clean fuel—without any emission of smoke. Only later it became clear that burning H_2 in air can produce NO_x as a pollutant.

In the following years the interest in hydrogen as a fuel grew even further. The German engineer Rudolf Erren converted trucks, buses, submarines and internal combustion engines to run on hydrogen. At that time, hydrogen was a popular supplement fuel in large dirigibles in both Germany and England [3,4]. German Ferdinand von Zeppelin promoted the idea of rigid airships lifted by hydrogen that later were called Zeppelins. In 1931, an airship named *Hindenburg*, which was inflated by hydrogen, was built. After ten successful trans-Atlantic flights from Germany to the United States, the *Hindenburg* met a disaster. It burned into flames while landing in Lakehurst, Naval Air Station in Manchester Township, New Jersey, United States, on May 6, 1937. This accident claimed the life of thirty-six people. This disaster created a negative public image of hydrogen gas as being extremely dangerous. However, the most recent analysis of the fire mentions that the fabric covering the airship was the cause for the fire rather than the hydrogen gas [8,9].

During World War II, the Australian government considered the use of industrial hydrogen to meet the increasing fuel demand and mitigate the risk of being cut-off of the fossil fuel supply. However, this interest did not survive for long. The Allied victory made cheap oil and gasoline available again, and this led to the death of the interest in hydrogen as fuel [3].

Around 1950, the interest in hydrogen revived again in the context of fuel cells. In 1959, Francis Thomas Bacon built the *Bacon Cell*, which was capable of producing 6 kW of power and enough to power a welding machine. Bacon played a major role in the development of a fuel cell. He implemented a number of modifications to the original design of the fuel cell by Grove. He replaced the platinum electrodes with less expensive nickel gauze electrodes. He also substituted the sulphuric acid electrolyte with aqueous potassium hydroxide, a substance less corrosive to the electrodes [10]. It was the first alkaline fuel cell (AFC). In late 1959, Harry Karl Ihrig, an engineer for the Allis—Chalmers Manufacturing Company, demonstrated the first fuel cell-powered vehicle [4].

Beginning in the late 1950s and early 1960s, interest in the fuel cell renewed. NASA (National Aeronautics and Space Administration) wanted

to power a series of upcoming manned space flights. Batteries, solar energy, and nuclear power had already been ruled out due to heavy weight, high cost, and high risk, respectively. The fuel cell was considered as a possible solution for an alternative power source by NASA. Sponsorships by NASA for the efforts to develop a practical working fuel cells that could be used during the space flights, resulted into the development of the first proton exchange membrane (PEM) fuel cell. GE (General Electric) scientists, Willard Thomas Grubb and Leonard Niedrach, modified the original fuel cell design by using a sulphonated polystyrene ion-exchange membrane as the electrolyte, and depositing platinum onto this membrane, respectively. This modified fuel cell ultimately became known as the *Grubb-Niedrach fuel cell*. GE and NASA developed this technology together resulting in its use on the Gemini space project, which was the first commercial use of a fuel cell.

In the early 1960s, the Bacon patents for the AFC were licensed by the aircraft engine manufacturer Pratt & Whitney. Pratt & Whitney improved the original Bacon design by reducing the weight and designing a longer-lasting fuel cell than the GE PEM design. This improvement resulted in Pratt & Whitney winning a contract from NASA to supply these fuel cells to the Apollo spacecraft. Alkali cells have since been used on most subsequent manned United States space missions [11].

The idea of a *hydrogen economy* was developed already in the 1970s by John O'M. Bockris, an Australian electrochemist, who was working as a consultant with GM (General Motors). His ambitious energy concept involved that the cities of the United States could be supplied with energy derived from the sun and the energy stored using hydrogen. However, GM did not pursue the technology to any significant degree. Nevertheless, Bockris continued his campaign, and the phrase *hydrogen economy*, became an important concept [3].

Roger Evan Billings is another important figure in developing the hydrogen energy. In 1966, at the age of only 16 years Roger Billings modified a car model of Ford to run on hydrogen and converted many late model automobiles to run on hydrogen using their internal combustion engines. Billing is still actively participating in hydrogen energy development [12].

Further, the fuel crisis in 1973 raised the scientific interest in hydrogen. This led to the creation of organizations such as the International Association for Hydrogen Energy (IAHE) in 1974 and the National Hydrogen Association (NHA) in 1989 [4]. By the early 1980s, the hydrogen economy was thought to be *on its way*, but the interest in hydrogen disappeared the following decade after a significant drop in the oil prices [3]. During the next decade, the hydrogen research continued to develop slowly.

In the last decade, issues like global warming, growing energy demand, and dependence on imported oil gained political attention and pushed the hydrogen research further. The next sections will highlight in more detail the need of a hydrogen economy, current developments and the remaining challenges mainly in the hydrogen storage research, related to this thesis.

1.2 Need for a hydrogen economy

As mentioned earlier, fossil fuels in the form of coal, oil, and natural gas are the major sources to satisfy energy needs of our society since the industrial revolution, i.e., the 18th century. Further, the world's energy demand for energy is increasing, projected to be doubled by 2030 [13] (see Figure 1.1), mainly due to the industrialization of developing countries such as China and India. In addition, fossil fuels are finite reserves that are progressively difficult to recover. The use of fossil fuels for energy needs in the future endangers the environment, as burning of fossil fuels produces green house gases that result into global warming. Further, most countries cannot produce enough oil to meet demands, so they import it from oil-rich countries—OPEC (Organization of the Petroleum Exporting Countries), creating an economic political dependence. These are some key factors which lead countries throughout the world to look for alternative energy resources that are renewable, abundant, secure, environmentally benign, and cost effective.

One of the solutions to deal with the above mentioned issues is to move to renewable energy resources such as solar, wind, hydro, and geothermal power energy. In view of the intrinsic intermittent nature

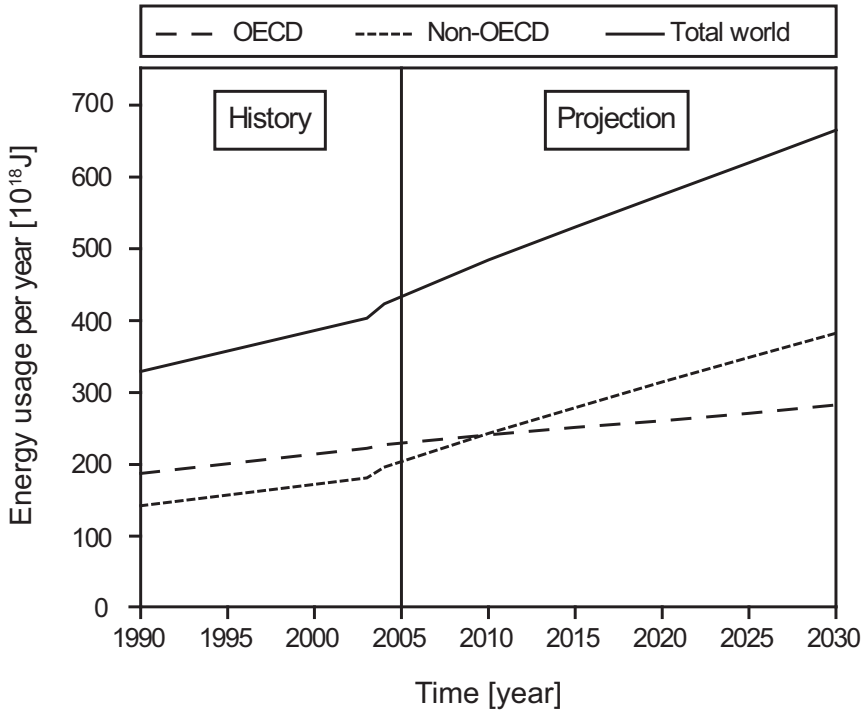


FIGURE 1.1 – Estimated growth of demand of energy by the world population [13]. OECD stands for Organization for Economic Co-operation and Development.

of these sources, a fuel as energy carrier and effective energy storage before use of the energy is required. Hydrogen is attractive as a clean fuel (exhaust water only) because of its high energy content and because it can be produced from only water H_2O , which is abundant, and energy. Only 8 kg of hydrogen, equivalent to 24 kg of petrol, is needed for the combustion engine version in on-board vehicles to cover 400–500 km of distance without refilling the tank [14]. However, hydrogen is a gas at ambient temperature and pressures, and 8 kg of hydrogen occupy a volume of 90 m^3 , corresponding to a balloon of roughly 6 m in diameter. This poses a challenge to use it for on-board applications in practice, because compact hydrogen storage is required [14].

1.3 Hydrogen storage challenges

One of main challenges to move to the hydrogen economy is to store it in a compact, safe, energy efficient, and cost effective way. Hydrogen can be stored in a number of ways such as in tanks as compressed gas (>400 bar) or as a liquid. Hydrogen can also be stored in materials, and is then subsequently released upon heating the materials. Storing hydrogen in a solid is very attractive because in this way larger quantities of hydrogen can be stored in smaller volumes at low pressures and at temperatures close to room temperature. Metal hydrides can be used for hydrogen storage. A number of metal hydrides exist such as ionic hydrides (LiH, MgH₂, and NaH), complex hydrides (Mg₂NiH₄, NaAlH₄), metallic interstitial hydrides (PdH_{0.7}, LaNi₅H₆), and chemical hydrides (NaBH₄). A good metal hydride should possess a number of qualities such as a high hydrogen content (expressed in wt.%), fast reversible H₂ absorption, operating temperatures not far from ambient, safe operation conditions, and cost effectiveness for commercial considerations. One of the most basic requirements is to have a high hydrogen content, which is satisfied by light-element (low-Z) hydrides, making them potential candidates for hydrogen storage (see Figure 1.2). MgH₂ and NaAlH₄ are among the potential hydrides which possess a high hydrogen content. MgH₂ shows 7.6 wt.% of hydrogen storage capacity, and NaAlH₄ can store up to 5.5 wt.% of hydrogen [15].

Potential candidates and practical issues

Despite of a number of advantages such as high hydrogen content, cheap cost, easy availability, and easy manufacturing, pure MgH₂ can not be used for practical application because of its slow sorption kinetics and high operational temperature, i.e., >280 °C. A significant progress has been made in recent years to improve the sorption kinetics in MgH₂ by making nano-crystalline particles in combination with suitable catalysts¹ [16–20]. Further, MgH₂ also shows a long-term cycling stability up to 2000 cycles [21]. However, the high desorption temperatures of MgH₂ urges

¹MgH₂ shows superior kinetics upon addition of Nb, V, Nb₂O₅, or V₂O₅ as a catalyst.

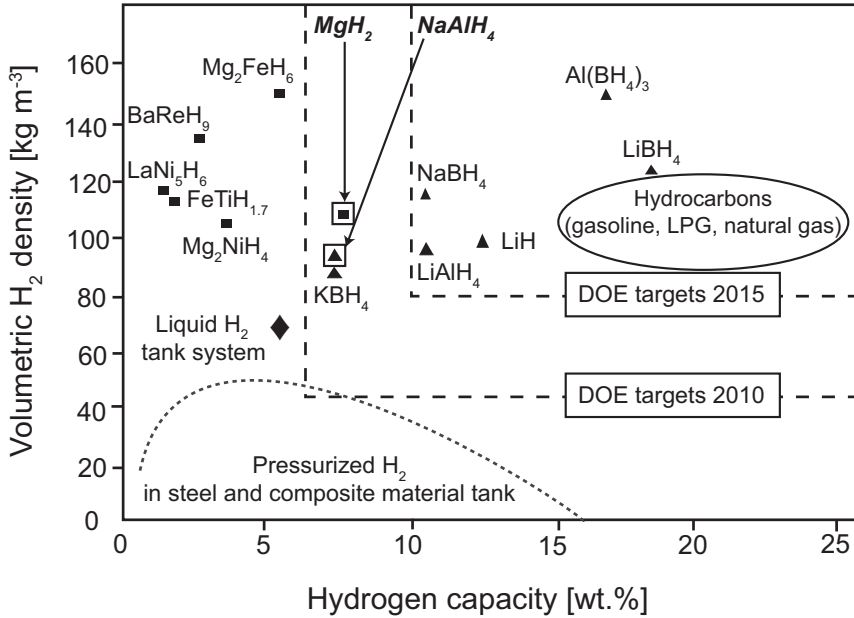


FIGURE 1.2 – A comparison of metal hydrides, pressurized tanks, liquid hydrogen tanks, and hydrocarbons is presented [15]. MgH_2 and $NaAlH_4$ are examples of a few potential candidates for hydrogen storage because of their relatively high hydrogen capacity. LPG stands for liquefied petroleum gas. The US Department of Energy (DOE) material targets for 2010 and 2015 are shown by dashed lines. The DOE material targets do not include the weight of the tank containing the metal hydrides.

one to look for systems which can be operated at lower temperatures while still having the high hydrogen content. Such an approach leads, for example, to different compounds like $NaAlH_4$, which shows a reversible capacity of 4.5 wt.% at temperatures in the range of 80–150 °C with the addition of suitable catalysts² [22,23].

Another approach to deal with the high desorption temperature of MgH_2 is to combine MgH_2 with other binary hydrides or elements which

² $NaAlH_4$ is irreversible without addition of a catalyst. Among many different catalysts, Ti-based compounds make the reaction reversible.

can lead to a significant increase in the equilibrium pressure, i.e., lowering of the overall enthalpy for dehydrogenation [24]. Such a second approach to address the thermodynamic constraints is to combine, for example, MgH_2 with Si. The enthalpy of formation is reduced because now Mg_2Si is formed upon H_2 release. The desorption of MgH_2 in the presence of Si indeed leads to increased equilibrium H_2 pressure at 300 °C, but at the expense of a certain decrease in the hydrogen capacity to 5.0 wt.% [24].

1.4 Aim of this thesis

In these two promising approaches, many light metal hydrides nevertheless suffer from slow reaction kinetics, making it difficult to use them for applications. It is important to know the factors which affect the reaction kinetics in order to improve them. Several factors which can influence the reaction kinetics, such as the dimensions of particles and grain sizes, defects like atom vacancies and grain boundaries, and appropriate catalysts and their homogeneous dispersion. For example, the presence of a hydrogen bond splitter facilitates the reaction kinetics. Further, nano-dimension (<150 nm) grains provide a shorter diffusion path for H atoms, as compared to micro-dimension grains (≥ 1 μm) distances. This results in relatively fast sorption. In addition to the smaller grain sizes, vacancies and grain boundaries further facilitate the diffusion in metals (solids).

Grain refinement and vacancies in catalyzed light metal hydrides

A homogeneous mixing of the catalysts and the reduction of particles and grains to nano-dimensions (<150 nm) can be achieved simultaneously using high energy ball milling. However, as will be shown in this thesis and was previously shown for MgH_2 in [20, 25], some of the hydrides grow in sizes during hydrogen cycling although the initial particle (grain) sizes are nanoscopic. Because the nanoscale dimensions of particles then disappear, this will present a barrier on H_2 cycling, and may affect the reaction kinetics. Therefore, a mechanism is needed, which can facilitate the maintenance of grain sizes to a nano-dimension during H_2 cycling.

One promising mechanism by which various additives could control the grain growth during the hydrogen cycling is presented in this thesis. In particular, two model systems MgH_2 and NaAlH_4 were investigated. The presented mechanism to arrest the grain sizes can probably be applicable to the more general field of metal hydrides for reversible hydrogen storage.

In the field of metal hydrides, a well established concept for the role of the catalysts is that they help in splitting the hydrogen bond at the surface of the material. It is thus intrinsically assumed that breaking hydrogen bonds is the rate limiting step in the sorption kinetics. If the (de)hydrogenation kinetics is dependent only on the hydrogen splitting at the surface, the addition of a hydrogen splitter alone would be sufficient to improve the reaction kinetics. Transition metals are known to act as catalysts, and are known to be good hydrogen molecule splitters. Interestingly, there is no unique catalyst, i.e., hydrogen splitter for all light metal hydrides. Different metal hydrides require different catalysts. For example, TiCl_3 shows superior catalytic activity for NaAlH_4 by making the reaction reversible and increasing the kinetics simultaneously. That not just any hydride forming transition metal can be used may indicate that these catalysts (additives) play an *additional* role besides dissociating H_2 during sorption reactions.

Grain refiner An *additional* role of the catalyst as a *grain refiner* is introduced in this thesis. It is suggested that the added catalysts (additives) form a new compound (alloy) by reacting with the other elements available. Subsequently, these alloys act as nucleation centers for the phases (metal or metal hydride) formed during H_2 sorption, and in this way restrict the growth of crystallites. The phase that acts as a nucleation center is known as the *grain refiner*, and the process is called grain refinement [26,27]. One of the prerequisites of the grain refining action to occur is to have a good structural and chemical lattice matching between the nucleus and the growing phase (metal or metal hydride).

Such additional formation makes it very likely that only a certain group of catalysts will work for a certain (complex) metal hydride. Not

every catalyst will give rise to an alloy which shares the same crystallographic structure with the hydride or with the other occurring phases during the hydrogen cycling. Besides a good lattice matching, a sufficient concentration and a good dispersion of these nucleation centers is required to have an effective grain refining action. Further, the resulting size of the metal or metal hydride phase depends on the amount of nucleation centers. A high density of nucleation centers leads to finer grains.

Hydrogen vacancies Due to the altered characteristics such as the surface to volume ratios and the influence of interface and surface energies, the thermodynamics of H₂ sorption in small crystallites may be altered [20,28]. For this reason, depending on gas (H₂ or D₂) pressure and temperature, small crystallites may contain hydrogen vacancies, which further facilitate the reaction kinetics. A possible origin of these vacancies can be related to interfaces, nanostructure, or the catalyst. Therefore, grain refiners facilitate the reversibility by keeping crystallites small, reducing the diffusion path and in addition improve diffusion by providing vacancies and shorter diffusion path in the nano-sized crystallites (<150 nm).

Synopsis

The structural evolution at the nanoscale was investigated during hydrogen release and uptake for light-weight metal hydrides using advanced characterization techniques and theoretical studies. In particular MgH₂ and NaAlH₄ were considered to be the model systems. Advanced analysis methods such as X-ray and neutron diffraction, electron microscopy, and positron depth profiling were applied. Moreover, ab initio calculations based on density functional theory were performed. A basic introduction of the techniques and methods used for the work is presented in Chapter 2.

Pd-capped Mg thin film studies show that the Pd catalyst acts as hydrogen bond splitter. The impact of the presence of a Pd cap-layer on the hydrogen sorption kinetics and temperatures of uptake and release is

much higher than that of the nano-columnar grain structure. A martensitic like phase transformation from Mg to MgH_2 occurs with an orientation relationship of $\text{Mg} (0002) \parallel \text{MgH}_2 (110)$. Additionally, electronic structure changes of metal hydride thin films used as hydrogen switchable mirrors and hydrogen sensors can be obtained using the positron depth profiling technique.

The following chapters show results and discussion to support the ideas that the catalyst acts as grain refiner for TiCl_3 -catalyzed NaAlH_4 , Nb_2O_5 -catalyzed and Si-destabilized MgH_2 , and TiF_3 -catalyzed MgD_2 . Further, this study also shows experimentally observed hydrogen vacancy formation in Na_3AlH_6 , NaH , and in MgD_2 nano-crystallites. Ab initio calculations show that vacancies increase the reaction kinetics by decreasing the migration barriers; and consequently increase the diffusion. A model of the interface of NaH with NaCl , the latter acting as a nucleation center, was evaluated as one way to explain the large amount of hydrogen vacancies in nano- NaH observed experimentally in TiCl_3 -doped NaAlH_4 upon hydrogen cycling. The calculated low interface energies support the view that NaH grows easily on NaCl nucleation centers, and assists the idea of the role of NaCl as grain refiner for NaH . Additionally, local transformations associated with the solid state reactions for Mg-Si bilayer thin films capped with Pd were also studied.

In conclusion, this study shows that key ingredients to improve the reaction reversibility and kinetics are the maintenance of crystallite sizes to the nanoscale and the presence of vacancies during hydrogen cycling. Therefore, a right choice of a catalyst, which from its reaction products can provide a grain refining action, is needed for light-metal hydrides to improve the reaction kinetics.

2

Methods

Tailoring the particle size to nano-dimensions is one of the possible ways to overcome the barriers, such as slow reaction kinetics and irreversibility, for practical applications of hydrogen storage materials. Ball milling is a commonly used technique to achieve nanoscale particle as well as grain sizes. The technique also allows an easy mixing with catalysts, and enables scaling up to industrial applications. Thin film synthesis is another technique to achieve nanostructured materials. Additionally, thin films offer a number of advantages such as a control on the interface, a control over the layer thickness and a flexibility to tailor both the composition and the degree of crystallization. Both methods, ball milling and thin film synthesis, have been used to prepare materials, and a number of techniques were used to study these samples for this research.

2.1 Ball milling

The technique involves crushing and disintegration of powders by high energy collisions with the grinding balls in the grinding bowl of a planetary ball mill. The grinding bowl, containing the grinding balls and the material to be ground, rotates about its own axis on a main supporting

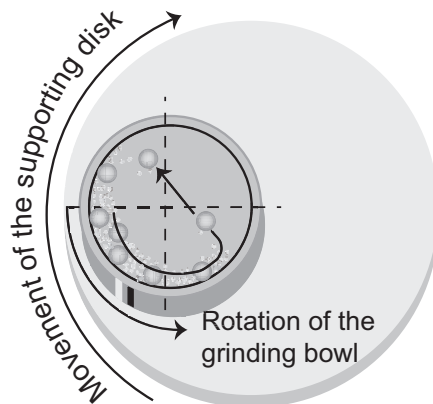


FIGURE 2.1 – Schematic diagram showing the working principle of ball milling [29].

disc, which is rotating rapidly in the opposite direction (see Figure 2.1). The motion results into large centrifugal forces which act upon the grinding balls and the material. In planetary action, the centrifugal forces alternately add and subtract. With this configuration, the centrifugal force causes the material and grinding balls to separate from the inner wall of the grinding bowl at a certain speed. The grinding balls cross the bowl with a high speed and hit the opposite bowl wall covered with the material, and grind the material due to the impact against the inner wall. The reduction of particle and grain sizes in the powder is mainly due to the frictional effect, caused by the movement of balls along the inner walls of the grinding bowl, and the impact effect, caused by balls hitting the opposite wall of the grinding bowl [29]. The resulting average size depends on the number of balls, the size of the balls, the rotational speed, and the time of grinding. These parameters should be chosen carefully in order to obtain the desired sizes.

A Fritsch Pulversette 6 planetary monomill was used to prepare nanostructured powders and a homogeneous mixing of catalysts. A stainless steel bowl of 80 ml and 32 stainless steel balls with a diameter of 10 mm were used. A sufficient amount of the powder to be ground (2–3 g) was

placed on top of the grinding balls in the bowl. The assembly of the closed bowl, containing balls and the powder to be ground, was weighed in order to set a counterweight to compensate for the mass imbalance before the milling. The powder was ground for a period for 60 min with a 15 min pause time after 15 min rotation with a rotational speed of 400 rpm.

The handling of all powders was done in the glove box containing Argon (Ar) as a working inert gas with the O₂ and H₂O content of ≤ 0.1 ppm. All powders (except the hydrides) and equipment such as balls, bowl, and spatula, etc., were baked out in a vacuum oven at 60 °C for a few hours before bringing them into the glove box. The lid of the bottle (empty or filled with powders) was opened slightly before keeping it in the antechamber, and flushing was done slowly. All bottles in the glove box containing powders were closed tightly and further sealed with a Parafilm (around the lid) to make sure that they are sealed after use.

After the milling process, the bowl was emptied in the glove box. For further cleaning, 2–3 g of Alumina or aluminum oxide (Al₂O₃) powder (0.5 μm)¹ was milled for 10 min with the same number of balls at 400 rpm. After the milling, the bowl was emptied in the glove box or fume hood, and further washed with water.

TiCl₃-catalyzed and uncatalyzed NaAlH₄ samples were prepared in the laboratory of Prof. Dr. J. Huot, Université du Québec à Trois Rivières, Québec, Canada using Spex 8000 and similar procedures (see Section 4.1).

2.2 Thin film synthesis

Two types of film deposition methods, plasma sputter deposition and pulsed laser deposition techniques, were used to prepare the films.

2.2.1 Sputtered deposition

Plasma sputter deposition (PSD) is a physical vapor deposition (PVD) method. PSD is a very versatile tool to control the layer thickness, which

¹For a better cleaning, a crystallite size of Al₂O₃ powder of ≥ 1 μm is recommended.

depends on the preparation conditions [30]. In this technique, ejection of atoms occurs from a target upon collision of energetic noble gas ions, and these ejected atoms travel and are deposited onto a substrate placed opposite of the target (see Figure 2.2). In sputter deposition, a noble gas such as Ar is ionized by electrons, which are emitted from a filament. These ions will bombard the target, which is at a high negative potential, resulting into ejection of atoms from the target. The removed atoms, having substantial kinetic energies, are deposited on the substrate maintained at a relatively positive potential. The ejected atoms have a wide distribution of energy, typically as high as a few of electron volts. Not all ejected ions reach the substrate, only ions with sufficient energy will reach the substrate. The energy with which these ions arrive at the substrate depends on the distance to the target in combination with the working Ar pressure during the process.

Figure 2.2 shows the setup used to prepare the sputtered thin films. An Ar plasma at a pressure in the range of typically $(1-3) \times 10^{-6}$ bar was created using a bundle of electrons, which were emitted from a tungsten (W) filament using a current of 3.5 A. A voltage of 70 V was used on the magnet coils to straighten the ejected electrons into a bundle. A high *negative* potential was imposed on a target up to -500 to -1000 V, and the voltage on the substrate was in the range of 0 to -200 V i.e., at a potential relatively positive to the target potential. The temperature at the substrate was in the range of approximately $30-50$ °C depending on the deposition conditions. The distance between the target and the substrate was maintained to 10 mm. The application of -500 V for 5 min gives a thickness of $50-100$ nm of Palladium (Pd) depending on the Ar pressure. These thicknesses were different for other target materials such as Magnesium (Mg) and Silicon (Si) targets (see Ref. [31]).

The cleaning process of a target was performed before each film deposition using Ar bombardment; the substrate was screened by a shutter. After cleaning the target, the shutter was removed and a film of desired material was deposited on the substrate.

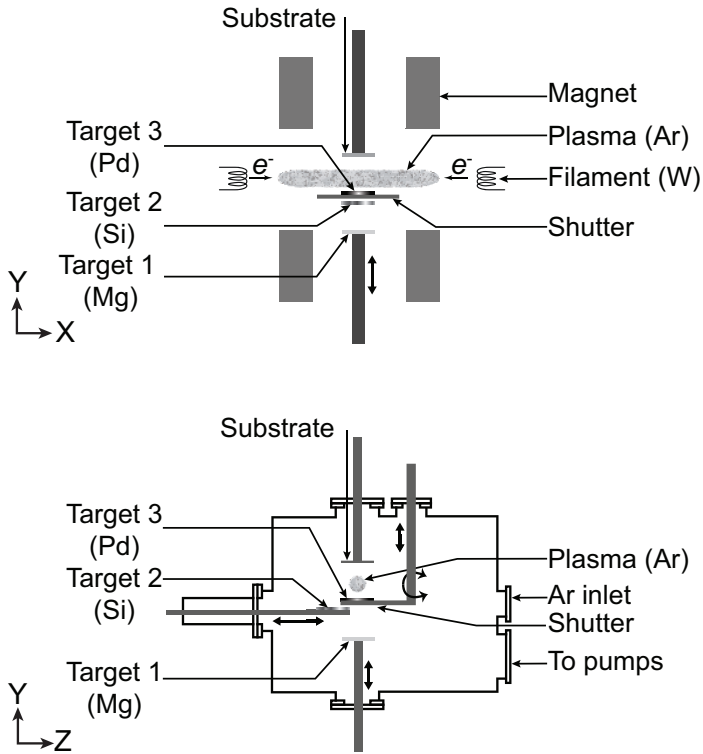


FIGURE 2.2 – Schematic diagram of plasma sputter deposition setup.

2.2.2 Pulsed laser deposition

Pulsed laser deposition (PLD) technique is one of the newer techniques for depositing thin films. The PLD technique differs from sputtering in two main features, namely (i) the high energy of the evaporated species involves both neutral atoms and ions; and (ii) the discontinuity of the deposition process corresponding to high instantaneous deposition rates [32]. Thus, laser deposition favors the formation of non-equilibrium films, as previously also observed for metal hydride films [33, 34]. The PLD configuration contains a high-power laser located outside the vacuum deposition chamber. External lenses are used to focus the laser beam onto the target surface, which acts as an evaporation source. A solid state

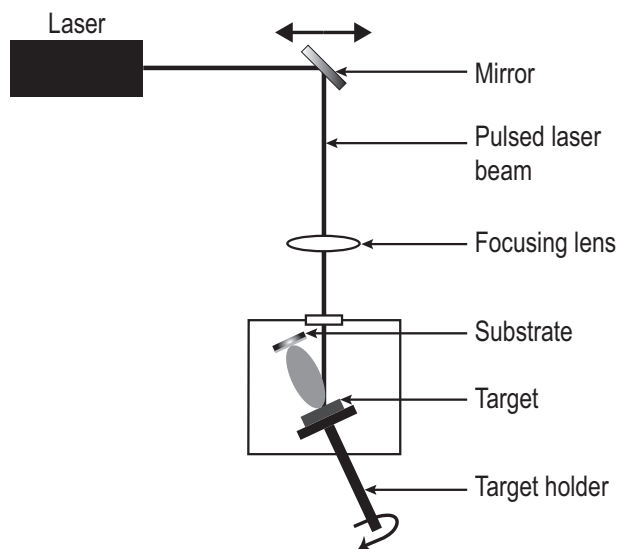


FIGURE 2.3 – Illustration of the pulsed laser deposition setup.

Nd^{3+} :YAG (1064 nm) or $\text{Nd}:\text{Y}_3\text{Al}_5\text{O}_{12}$ (Neodymium-doped yttrium aluminum garnet) laser is used for PLD. The YAG laser can deliver up to roughly 2 J pulse^{-1} at a pulse repetition rate of close to 30 Hz. The energy of the laser beam absorbed by the material is converted into thermal, chemical, and mechanical energy, resulting into electronic excitation of target atoms, ablation, and plasma formation. Evaporated species such as neutral atoms, molecules, electrons, ions, atom clusters, micro sized particulates, and molten droplets form a plume above the target. The plume is highly directional, and its contents are pushed to the substrate and form a film after condensation [32].

An in-house built PLD setup (see Figure 2.3) was used.² The setup contains a Surelite pulsed Q-switched Nd: YAG laser, producing laser pulses of 5–7 ns with an incident energy of $0.45 \text{ J pulse}^{-1}$. An Ar pressure in the chamber was maintained in the range of $(1\text{--}4)\times 10^{-7}$ bar to get an appropriate cone of the plasma plume. The laser pulses are redi-

²The setup allows to deposit two films simultaneously.

rected via a mirror through a focusing lens to hit the Mg target covering an area of about 0.05 cm^2 . A plasma plume was emitted from the target. The evaporated target particles subsequently condense on a Si (100) substrate positioned opposite the target. The distance between the target and the substrate was maintained to 30 mm, and the Mg deposition speed was 0.64 mg h^{-1} . The deposition time of 45 min resulted in $1 \mu\text{m}$ thick Mg films. The temperature at the substrate was monitored, and found to remain within $T \approx 30\text{--}40 \text{ }^\circ\text{C}$ only throughout the deposition process. The vacuum pump was switched-off after 10–15 min of stopping the laser so that the target has time to cool down and the chances of oxidation reduce. The laser head could be moved horizontally in order to achieve a homogeneous thickness of the film. Furthermore, the target holder could be rotated such that subsequent laser pulses hit the target at different positions, preventing crater formation resulting from the severe local heating and melting of the target material.

2.3 X-ray diffraction

X-ray diffraction (XRD) is a non-destructive technique, and it gives information about the crystal structure, chemical composition, and physical properties for powder as well as thin film samples. This technique involves elastic interaction of X-rays with the electron cloud around an atom. The X-rays are scattered from the regular array of atoms in the material and can interfere with each other either constructively or destructively. The interference is constructive, when the path difference is an integral multiple of λ , i.e., Bragg's law (Equation (2.1)) is satisfied, and a diffraction pattern characteristic to the material is obtained. Bragg's law treats the lattice planes of atoms as mirror that reflect the incident rays. Bragg's law reads

$$n\lambda = 2d_{hkl} \sin \theta, \quad (2.1)$$

where n is an integer, λ is the wavelength of the radiation (X-rays in this case), d_{hkl} is the interplanar spacing for a lattice plane with Miller indices hkl , and 2θ is the angle between the transmitted and scattered beam directions (see Figure 2.4). Constructive interference will occur only

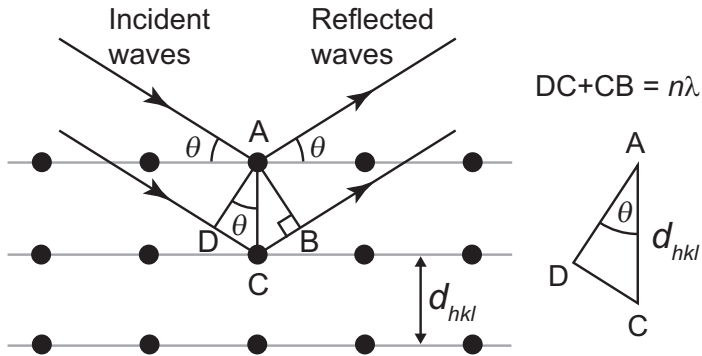


FIGURE 2.4 – Schematic showing Bragg's Law.

when the path difference between the waves scattered from successive layers of atoms is a multiple of the wavelength of the incident beam, and gives rise to *Bragg reflections* only in certain well defined directions. For example, if a single crystal is placed in the beam, then the scattered beams are observed in any directions for which Bragg's Law is satisfied by some set of Bragg planes.

A XRD sample holder having a Kapton covering, with a thickness of approximately $25 \mu\text{m}$, was used to avoid air contact with the sample. The Kapton covering was fixed using a two component glue after a thorough cleaning of all the parts using ethanol. Subsequently, the sample holder was checked for an air tight closing. For XRD, all samples were handled in a glove box containing Ar as the working gas. The powder was leveled using a glass plate. Most of the samples were characterized using an Bruker-AXS Type D5005 diffractometer with the $\text{Cu K}\alpha$ (1.54 \AA) wavelength at the department of DelftChemTech at Delft University of Technology.

A few samples were characterized using $\text{Co K}\alpha$ (1.79 \AA) with a similar type of diffractometer at the Department of Mechanical, Maritime and Materials Engineering at Delft University of Technology. For this research, XRD was mainly done to confirm the structure and phases present in a sample. All XRD diffraction data were treated with Rietveld refinement using an interface software program [35]. Mostly, samples were

measured in the 2θ range of $25\text{--}85^\circ$ with a step size of 0.05° . Further, information about the particle sizes were also obtained from peak broadening using a formula (Equation (2.2)), where centidegree was converted to radians, based on the Scherrer's equation,

$$g = \frac{18000K\lambda}{X\pi}, \quad (2.2)$$

where g is the grain or crystallite size in \AA , λ is the wavelength of X-rays in \AA , K is the Scherrer constant, and X is the profile coefficient in centidegree, which was used to fit the broadening of the peak shape. In this approach, however, the effect of strains on the line broadening is taken care of by another dependence of broadening on the d -spacing. Strain broadening is linear in d -spacing while crystallite size broadening varies with d^2 .

2.4 Electron microscopy

Electron microscopy is based on the interaction of an electron beam with the material to be investigated, and gives local information about the structure, morphology, and composition of the material. Electron microscopy comprises of different methods, which are used on the basis of the question to be answered. Techniques like transmission electron microscopy (TEM) and selected area diffraction (SAD) are used to learn about the structure of a sample at the microscopic scale. Transmission electron microscope can be used to obtain information in real space or imaging mode and reciprocal space or diffraction mode, almost simultaneously, making TEM a special technique to study materials on nanoscale dimension. The electron interactions with matter are classified as elastic interactions and inelastic interactions. In elastic interactions, no transfer of energy from the electron to the sample occurs. In this case, the electron either passes without any interaction (direct beam) or is scattered by the positive potential inside the electron cloud (diffracted beam).

Transmission electron microscopy

TEM utilizes the signals from elastically scattered electrons—either in the direct or diffracted beams. There are different use of transmission electron microscope such as bright field TEM and dark field TEM, high resolution TEM (HRTEM), and SAD mode. Bright or Dark field TEM are used to detect the crystalline areas, defects and grain boundaries, phase analysis and particle size. HRTEM is a good tool for a direct visualization of the local atomic scale structures and defects.

In this study, both bright and dark field TEM experiments were carried out on a number of samples, thin films as well as powders, using a Philips CM30T microscope at 300 kV. Thin film samples were glued with the epoxy glue in between 2 silicon (or glass) plates, and this sandwiched type formation was thinned down by polishing with 15, 6, 3, 1, and 0.5 μm grade sandpaper. Focused ion beam (FIB) specimens (initial dimensions: 15 μm \times 5 μm) were cut with ions at 30 kV, with the final specimen thickness 100–120 nm. The cut specimens were placed with a micro-manipulator onto a carbon holey grid and examined in TEM. Further, powder specimens were dispersed ultrasonically in 70% ethanol, and then dropped onto the holey carbon grid.

Selected area diffraction

SAD gives local insights into the lattice parameter and crystal symmetry, crystal orientation, and phase analysis. The diffraction mode can be achieved by using a diffraction lens in the transmission electron microscope. SAD, similar to XRD, is caused by constructive interference of scattered waves, and based on the fundamental Bragg's Law. However, SAD differs from XRD in many terms such as the involved wavelength of electrons, i.e., 0.0197 Å for 300 keV electrons, is much shorter than that of X-rays. The diffraction angles in electron diffraction are, therefore, very small i.e., 0–2°, while XRD involves a range of 0–180°. Electrons interact with both the nucleus and the electrons of the scattering atoms through Coulomb forces, resulting in a stronger interaction of electrons with matter than X-rays. This leads to high intensity diffracted electron

beams, and the exposure times in the order of a few seconds only, while it usually takes minutes or hours to obtain an XRD diffraction pattern. SAD patterns can, therefore, directly be seen on the viewing screen of the electron microscope. Thus, orienting a crystal along a direction can easily be achieved by tilting the specimen, while observing the corresponding changes in the SAD pattern simultaneously. However, the strong interaction also has its disadvantages, as it leads to multiple scattering, and influences the intensities of the reflections. These effects make structure determination from SAD more difficult and less reliable than that from XRD data.

A similar microscope, i.e., CM30T microscope was used for SAD experiments to study the samples, and images were obtained on cross-sections of the films using a beam spot size equivalent to about the thickness of the film.

2.5 Hydrogen release and uptake

Hydrogen desorption measurements were carried out to quantify the released hydrogen from metal hydrides using an in-house built setup called HYDRA (see Figure 2.5). The valve 4 divides the setup into its charging and discharging compartments. The sample was placed in the sample cell, which contains a sample holder that is in contact with an electrical heater (480 °C) and cooling system (−173 °C) using liquid nitrogen. The heater is isolated from the outer atmosphere by vacuum. The temperature of sample can be varied by using the heater and liquid nitrogen, and is monitored by using a K-type (Chromel—Alumel) thermocouple. A gas inlet was used to charge the sample. The maximum gas pressure which can be applied using this setup is up to 10 bar, and can be measured using the pressure meter *M0* ranging from 1 to 120 bar. The setup has two sets of rotary pumps and turbo(molecular) pumps to approach the vacuum down to 10^{-3} mbar and in the range of 10^{-4} — 10^{-10} mbar, respectively. The released hydrogen gas was detected using a quadrupole mass spectrometer, which was tuned to the mass of desired ions (hydrogen in this case) allowing accurate determination of the amount of released hydro-

gen gas. Simultaneously, the pressure of the released hydrogen gas was monitored using pressure meters $M1$ ranging from 10^{-4} to 0.1 mbar and $M2$ ranging from 0.1 to 1000 mbar. The released hydrogen was allowed to pass through a Pd filter to separate the hydrogen gas from the other possibly released gases such as H_2O or O_2 upon heating the metal hydride, and was further detected in the quadrupole mass spectrometer. The quadrupole mass spectrometer filters ions based on their mass-to-charge ratio. The amount of hydrogen atoms desorbed from the metal hydride can, therefore, be sensitively determined by quadrupole mass spectrometer. The hydrogen content H_c (in wt.%) of the metal hydride can be subsequently determined using the formula

$$H_c = \left(\frac{M_H \cdot (N_H / N_A)}{m} \right) \times 100, \quad (2.3)$$

where M_H is the molecular mass of hydrogen in g mol^{-1} , N_H is the total number of released hydrogen atoms, N_A is Avogadro's number (6.0223×10^{23} atoms per mole), and m is the initial mass of the metal hydride sample.

2.6 Neutron diffraction

Neutron diffraction experiments can be used to investigate crystal structures in a similar manner as X-ray diffraction. Like X-rays, they see individual atoms, but they see each atom and its isotope roughly equally clearly, independent of the atomic number Z . Neutrons interact with the nucleus of the atom as their neutrality allows them to penetrate inside the atoms, while X-rays interact with the electrons in the atom and see the shape of the electron cloud. The decision to use neutrons rather than X-rays depends on the atoms involved for structural studies. The property of neutrons to interact with the nuclei rather than the number of electrons in the electron cloud make them perfect to probe hydrogen, enabling them to investigate the hydrogen storage materials, and "see" hydrogen next to heavier elements.

Besides a number of advantages of neutrons over other techniques, neutron scattering techniques have some limitations such as in general

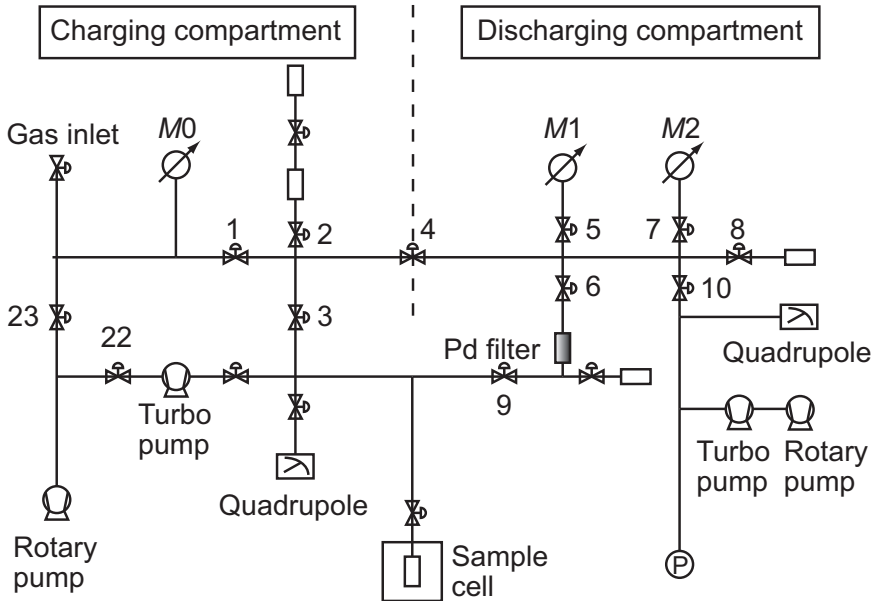


FIGURE 2.5 – Schematic illustration of the HYDRA setup showing its charging and discharging compartments.

neutrons are difficult to produce as compared to X-rays. This results in a relatively limited neutron flux that is available from neutron sources. As a consequence grams of sample are needed, and measurements can take minutes in favorable circumstances, but hours or up to days in less favorable circumstances.

In neutron diffraction, the neutron interacts with the nucleus of atoms elastically with no energy transfer from neutrons to the sample during the process. However, diffraction involves a transfer in the momentum to the lattice and the long range order of atoms in the material. In the diffraction experiment, a neutron beam irradiates the material that is under investigation. These neutrons interact with the atoms of the material and some of the neutrons get scattered by the nucleus. Mathematically, a neutron with a wave vector \mathbf{k}_i and energy E_i incident on the sample, and

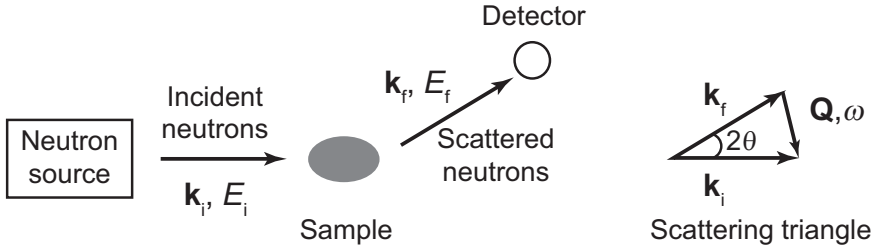


FIGURE 2.6 – Schematic illustration describing a neutron scattering event.

the neutron wavelength can be deduced using the expression

$$\lambda_i = \frac{2\pi}{|\mathbf{k}_i|}. \quad (2.4)$$

After the scattering event, the neutron is depicted with the vector \mathbf{k}_f with the energy E_f . The key variables in a neutron scattering experiment are the momentum and energy transfer³ of the neutron to the target material, which is represented as

$$\hbar\omega = E_i - E_f = \frac{\hbar^2}{2m_n} (k_i^2 - k_f^2), \quad (2.5)$$

$$\hbar\mathbf{Q} = \hbar(\mathbf{k}_i - \mathbf{k}_f), \quad (2.6)$$

where m_n is the mass of neutron, \hbar is Planck's constant divided by 2π , the quantity \mathbf{Q} is the scattering vector. The vector relationship between \mathbf{Q} , \mathbf{k}_i , and \mathbf{k}_f can be illustrated in the so-called scattering triangle (see Figure 2.6). The scattered neutrons are captured in a detector, which is at a certain angle placed relatively far from the sample, making a solid angle $d\Omega$ (see Figure 2.6). In the scattering measurements, the quantity that is measured is the partial differential cross-section, which gives the fraction of neutrons of incident energy E_i scattered into an element of solid angle

³For diffraction, there is no change in energy of the neutron, i.e., no energy transfer.

$d\Omega$ with an energy between E_f and $E_f + dE_f$. Mathematically, the partial differential cross-section is denoted as

$$\frac{d^2\sigma}{d\Omega dE_f} = \frac{I}{\Phi dE_f d\Omega}, \quad (2.7)$$

where I is the number of scattered neutrons per second and Φ is flux of the incident neutrons. The partial differential cross-section includes also the inelastic events.

The number of elastically⁴ scattered neutrons into the solid angle $d\Omega$ counted in the detector is given in terms of differential cross-section

$$\frac{d\sigma}{d\Omega} = \int_0^\infty \left(\frac{d^2\sigma}{d\Omega dE_f} \right) dE_f = \frac{I}{\Phi d\Omega}, \quad (2.8)$$

which is obtained by integrating Equation (2.7). Further, the total scattering cross-section, a fraction of the total number of neutrons scattered per second in all directions, is defined as

$$\sigma_{\text{tot}} = \int_{\text{all directions}} \left(\frac{d\sigma}{d\Omega} \right) d\Omega. \quad (2.9)$$

For elastic scattering, the differential cross-section can be calculated by knowing the probability of a transition from the state defined by the wave vector \mathbf{k}_i to the state defined by the wave vector \mathbf{k}_f . This probability is given by Fermi's golden rule

$$\Gamma_{\mathbf{k}_i \rightarrow \mathbf{k}_f} = \frac{2\pi}{\hbar} \left| \int \psi_{\mathbf{k}_f}^* V(\mathbf{r}) \psi_{\mathbf{k}_i} d\mathbf{r} \right|^2 \rho_{\mathbf{k}_f}(E), \quad (2.10)$$

where $\Gamma_{\mathbf{k}_i \rightarrow \mathbf{k}_f}$ are the transitions per second from the initial to the final stage, $V(\mathbf{r})$ is the interaction potential that causes the transition, in this case the interaction between the incident neutron and the target sample, and $\rho_{\mathbf{k}_f}(E)$ is the density of final scattering states per unit energy range.

Now, Equation 2.8 can be rewritten as

$$\left(\frac{d\sigma}{d\Omega} \right)_{\mathbf{k}_i \rightarrow \mathbf{k}_f} = \frac{\Gamma_{\mathbf{k}_i \rightarrow \mathbf{k}_f}}{\Phi d\Omega}. \quad (2.11)$$

⁴No transfer of energy to the target sample.

2.6.1 Coherent and incoherent scattering

The neutron-nucleus scattering is isotropic, and can be characterized by a single parameter, i.e., the scattering length b .⁵ The scattering length b can be complex, and the sign of the real part, negative or positive, depends on the type of nucleus and the energy of the incident neutron in the scattering process. The imaginary part of b represents absorption, capture of thermal neutrons, which is often, but not always, very small.

Generally, not only different atoms have different scattering lengths, but also each isotope has different scattering lengths. Additionally, the scattering length depends on the spin of the neutron and the nuclear isotope (the latter can be zero). The neutron has a spin $1/2$, and suppose the spin of a nucleus is \mathbf{S} . Then every non-zero spin nucleus has two values of the scattering length, i.e., $\mathbf{S} + 1/2$ or $\mathbf{S} - 1/2$. However, for the nucleus with a zero spin, the neutron-nucleus system can only have spin $1/2$, i.e., one value of the scattering length.

The interaction potential $V(\mathbf{r})$ due to the l th nucleus for the case of scattering due to more than one nuclei arranged in a rigid array is given as

$$V(\mathbf{r}) = \frac{2\pi\hbar^2}{m_n} \sum_l b_l \delta(\mathbf{r} - \mathbf{R}_l), \quad (2.12)$$

where N is the number of nuclei arranged in a rigid array, \mathbf{R}_l is the position vector of the l th nucleus, and b_l is the scattering length of the l th nucleus. Using Equation (2.10), Equation (2.11), and Equation (2.12), the differential cross-section can be written as the sum two terms

$$\frac{d\sigma}{d\Omega} = \left(\frac{d\sigma}{d\Omega} \right)_{\text{coh}} + \left(\frac{d\sigma}{d\Omega} \right)_{\text{incoh}}, \quad (2.13)$$

where the *coherent* cross-section is

$$\left(\frac{d\sigma}{d\Omega} \right)_{\text{coh}} = \left| \overline{b_l} \right|^2 \left| \sum_l \exp(i\mathbf{Q} \cdot \mathbf{R}_l) \right|^2, \quad (2.14)$$

⁵In XRD, b is replaced by an electronic form factor $f(\mathbf{Q})$.

and the *incoherent* cross-section is

$$\left(\frac{d\sigma}{d\Omega}\right)_{\text{incoh}} = \sum_l \left[\overline{|b_l|^2} - |\overline{b_l}|^2 \right], \quad (2.15)$$

where $(d\sigma/d\Omega)_{\text{incoh}}$ is the differential cross-section for *coherent* scattering and $(d\sigma/d\Omega)_{\text{coh}}$ is the differential cross-section for *incoherent* scattering. Coherent scattering involves a strong interference between waves scattered from each nucleus present in the crystal that have a well defined $\overline{b_l}$. The coherent scattering will then show strong constructive and destructive interferences resulting in e.g., Bragg peaks. This scattering potential is proportional to \overline{b} , thus the coherent scattering cross-section is proportional to $|\overline{b}|^2$. On the other hand, there is no constructive or destructive interference in the incoherent scattering at all because it depends on the deviations of the scattering length from the average.

2.6.2 Elastic scattering

In order to evaluate Equation (2.14), a number of terms related to crystal lattices and their reciprocal lattices is required before dealing with the coherent scattering for a rigid perfect crystal. Repetition of a unit cell periodically in space leads to construction of a perfect crystal. The unit cell, the building block of the crystal, can be defined by the set of three non-coplanar *basis vectors* \mathbf{a}_1 , \mathbf{a}_2 , and \mathbf{a}_3 and has a volume $v_0 = |\mathbf{a}_1 \cdot (\mathbf{a}_2 \times \mathbf{a}_3)|$. The lattice vector corresponds to the directions in the crystal, and is denoted as follows

$$\mathbf{l} = l_1\mathbf{a}_1 + l_2\mathbf{a}_2 + l_3\mathbf{a}_3, \quad (2.16)$$

where l_1 , l_2 , and l_3 are integers, known as cell indices. For the unit cell containing just one lattice site, every site in the crystal can be given by the lattice vectors \mathbf{l} ($\mathbf{R}_l = \mathbf{l}$). For more atoms in the unit cell, the positions of the atoms within a unit cell can be denoted by vectors \mathbf{d} as

$$\mathbf{R}_{ld} = \mathbf{l} + \mathbf{d}, \quad (2.17)$$

where \mathbf{d} is the position vector to the d th atom within the l th cell, where each unit cell contains n_a atoms.

For every crystal defined by a vector \mathbf{l} as in Equation (2.16), a reciprocal lattice with vectors \mathbf{G} can be defined in such a way that

$$\exp(i\mathbf{G} \cdot \mathbf{l}) = 1 \quad \forall \mathbf{l}, \quad (2.18)$$

while \mathbf{G} can be written as

$$\mathbf{G} = t_1\mathbf{b}_1 + t_2\mathbf{b}_2 + t_3\mathbf{b}_3, \quad (2.19)$$

where $t_1, t_2,$ and t_3 are the integers, and $\mathbf{b}_1, \mathbf{b}_2,$ and \mathbf{b}_3 are the basic vectors of the reciprocal lattice given by

$$\mathbf{b}_1 = 2\pi \frac{(\mathbf{a}_2 \times \mathbf{a}_3)}{v_0}, \quad \mathbf{b}_2 = 2\pi \frac{(\mathbf{a}_3 \times \mathbf{a}_1)}{v_0}, \quad \mathbf{b}_3 = 2\pi \frac{(\mathbf{a}_1 \times \mathbf{a}_2)}{v_0}. \quad (2.20)$$

From Equation (2.20), the volume of the unit cell of the reciprocal lattice can be given as

$$|\mathbf{b}_1 \cdot (\mathbf{b}_2 \times \mathbf{b}_3)| = \frac{(2\pi)^3}{v_0}. \quad (2.21)$$

Using the terms defined in Equation (2.16), Equation (2.19), and Equation (2.21), Equation (2.14) can be re-written as

$$\left(\frac{d\sigma}{d\Omega} \right)_{\text{coh}} = N \frac{(2\pi)^3}{v_0} \sum_{\mathbf{G}} \delta(\mathbf{Q} - \mathbf{G}) |F_N(\mathbf{Q})|^2, \quad (2.22)$$

where $F_N(\mathbf{Q})$ is the nuclear structure factor of the unit cell, which is defined as

$$F_N(\mathbf{Q}) = \sum_d \bar{b}_d \exp(i\mathbf{Q} \cdot \mathbf{d}). \quad (2.23)$$

For crystals for the study, the Debye-Waller factors should be considered, as the position of atoms are shifted from their equilibrium position at the temperature above $T = 0$ K. This shift in position due to thermal motion is given by a time-dependent term as follows

$$\mathbf{R}_{ld} = \mathbf{d} + \mathbf{l} + \mathbf{u} \begin{pmatrix} l \\ d \end{pmatrix}, \quad (2.24)$$

where \mathbf{d} is the position vector to the d th atom within the l th cell, where the each unit cell contains n_a atoms, and \mathbf{u} is the displacement from the equilibrium position.

The last term in Equation 2.24 is taken as the thermal average of the thermal displacement, and results as an extra factor in the structure factor. The Debye-Waller factor for an isotropic thermal movement is described as

$$\exp[-2U(\mathbf{Q})], \quad (2.25)$$

where $2U(\mathbf{Q})$ is given as

$$2U(\mathbf{Q}) = \langle [\mathbf{Q} \cdot \mathbf{u}]^2 \rangle = \frac{1}{3} \mathbf{Q}^2 \langle u_i^2 \rangle. \quad (2.26)$$

The structure factor in the Equation (2.23) can now be written as

$$F_N(\mathbf{Q}) = \sum_d \bar{b}_d \exp(i\mathbf{Q} \cdot \mathbf{d}) \exp[-U_d(\mathbf{Q})], \quad (2.27)$$

with

$$U_d(\mathbf{Q}) = \frac{1}{2} \left\langle \left[\mathbf{Q} \cdot \mathbf{u} \begin{pmatrix} l \\ d \end{pmatrix} \right]^2 \right\rangle. \quad (2.28)$$

The nuclear structure factor contain information about the intensity of hkl reflection. This means that the intensity depends on the content of the unit cell. The atomic positions in the unit cell can be defined as $\mathbf{d} = x_d \mathbf{a}_1 + y_d \mathbf{a}_2 + z_d \mathbf{a}_3$ ($0 \leq x_d, y_d, z_d \leq 1$). Now, the structure factor, i.e., Equation (2.27), can be re-written as

$$F(\mathbf{Q} = \mathbf{G}) = \sum_{d=1}^{n_a} \bar{b}_d(\mathbf{G}) \exp(i2\pi(hx_d + ky_d + lz_d)) \exp[-U_d(\mathbf{Q})].$$

The structure factor can become zero for certain positions (x_d, y_d, z_d) and certain values of hkl , and there will not be neutron scattering for those set of values, but the Laue's conditions are still fulfilled [36,37].

It can be deduced from the Equation (2.1) that two ways can be used in order to probe the reciprocal space. First method involves a monochromatic beam of neutrons of the known wavelength, λ , which incidents on the sample. The elastically scattered neutrons are measured as a function of scattering angle, 2θ . The second method is known as the time-of-flight (TOF), in which the sample is irradiated with a pulsed *white* beam containing neutrons of many different wavelengths. The neutrons travel a known distance, L , from a source to the sample to the (fixed) detector, which is positioned at an angle 2θ , and their arrival times at the detector are recorded. From θ , L , and the arrival times t , the wavelength λ can be calculated.

2.6.3 Neutron diffractometer

A neutron diffractometer, the GEneral Materials diffractometer (GEM) (see Figure 2.8) at the ISIS Facility, Oxfordshire, United Kingdom (UK), was used in order to study the crystallographic positions of the atoms within the unit cell of a crystalline material. GEM is the most advanced TOF materials neutron diffractometer in the world at the moment [38]. Neutrons are produced at ISIS by the spallation process. This process involves a spallation neutron source, a tantalum target, which is bombarded by pulses of highly energetic protons from a powerful accelerator. The neutrons are emitted from the highly excited nuclei of the target atoms, and a neutron pulse is emitted as a result of the collision along with a modest heat production in the neutron target. Each high energy proton bombarded to the target results in the production of approximately 15 neutrons on average. Neutrons that are produced in this process generally have high energies and velocities, and are slowed down using hydrogenous moderators around the target making them useful for condensed matter studies. The high energy neutrons repeatedly collide with the hydrogen nuclei and exploits the large scattering cross-section of hydrogen for the slowing down of neutrons. These neutrons with reduced energy, but still in short intense pulses. The so-called moderated neutrons are guided to the instruments that are grouped around the target [39].

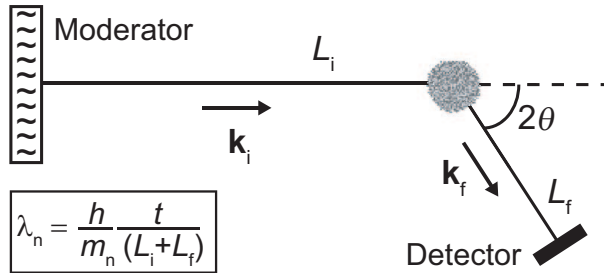


FIGURE 2.7 – Schematic of a neutron diffractometer for a pulsed (accelerator-based) neutron source [39].

Figure 2.7 shows a schematic diagram of a typical pulsed neutron diffractometer at a pulsed neutron source. The TOF technique does not require the use of a monochromator as it involves the determination of the wavelength of the neutrons. The neutrons travel a known distance $L = L_i + L_f$, from the source to the sample to the detector, which is fixed. The detector is positioned at an angle 2θ , and the arrival times of neutrons are recorded at the detector. In other words, the differential cross-section is measured as a function of \mathbf{Q} with the detector at a fixed scattering angle, 2θ , and \mathbf{Q} (or d -spacing) is scanned for a wide range of wavelengths for incident neutrons.

GEM combines an extraordinary neutron count rate with a very large \mathbf{Q} range. GEM has very good resolution in the backward angle detectors with $\Delta\mathbf{Q}/\mathbf{Q} = 0.2 - 0.3\%$ because of its relatively long incident flight path of 17 m and the use of large 2θ . GEM has 7290 neutron detectors, which are fixed, and grouped into 7 banks, each with a different range of accessible d -spacing (see Figure 2.8). Due to the high signal to noise ratios, it is possible to work with fully protonated materials although these give a high diffraction background due to incoherently scattered neutrons. For a diffractometer like GEM, the inelastic scattering is assumed to be relatively small and has no influence on the data analysis because it gives a smooth and low background. The ISIS website provides more information on the neutron scattering technique and the different types

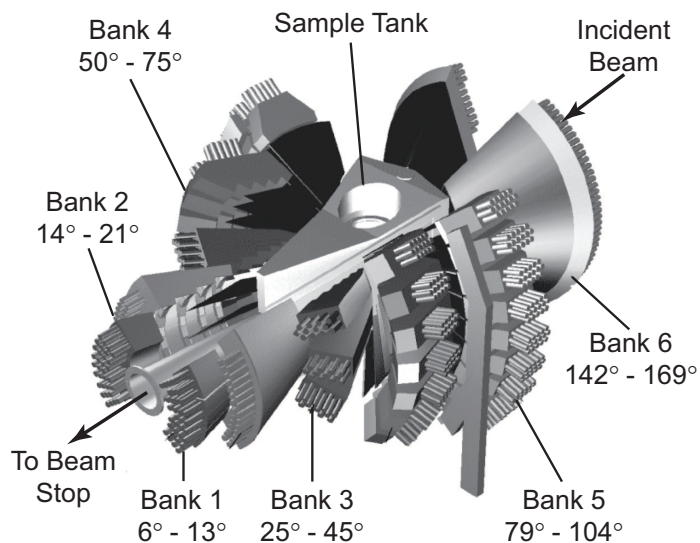


FIGURE 2.8 – GEM diffractometer at ISIS, Oxfordshire, UK [39]. The picture is taken from the ISIS website and slightly modified.

of instruments at the ISIS facility [39]. The obtained neutron diffraction patterns were analyzed using Rietveld refinement, and information about the hydrogen occupancy and grain sizes was subsequently extracted.

2.6.4 GSAS

GSAS (General Structure Analysis System) [35] is a software package, and is used with the EXPGUI interface. GSAS is used to fit a structural model of the crystal structure to a measured X-ray and/or neutron diffraction data set using the Rietveld method. The Rietveld method, can also be called structure refinement method; it uses a least-squares approach to fit a structural model to a measured powder diffraction data profile. Rietveld analysis is a powerful tool to determine the structural parameters, the relative amounts of the crystallographic phases, and the crystallite sizes that can be extracted from the peak broadening.

A known crystal structure is required, which contains information about the structural parameters such as its unit cell, the atom positions, occupancy, space group, and thermal parameters. Further, a variety of instrumental parameters that describe the experimental conditions such as peak broadening, position of the sample, etc. are also required. A number of background functions can be used to fit the background with an adjustable number of terms. Different background functions are developed and have a different theory to fit different shapes. However, the first function "Chebyshev polynomial" is a good option for the vast majority of Rietveld refinements. Subsequently, the software is allowed to optimize (refine) a small subset of these parameters—a minimal number of parameters to fit the diffraction pattern. Additional relevant parameters can thereafter be selected to be refined, until a good fit is obtained. The goodness of fit can be determined by the reduced chi-square value and more exactly by the weighted residual for powder diffraction R_w . The residual is a measure of the agreement between the crystallographic model and the experimental diffraction data. For a good fit, the value should be less than 0.04. R_w can be represented as follows

$$R_w = \left(\frac{\sum w (|I_{\text{obs}}| - |I_{\text{cal}}|)^2}{\sum w |I_{\text{obs}}|^2} \right)^{\frac{1}{2}}, \quad (2.29)$$

where I_{obs} is the observed intensity and I_{cal} is the calculated intensity.

In practice, for the fitting, after creation of the GSAS experiment file using EXPGUI, a fair amount of information about the sample was provided before starting the refinement. For each phase, a "Crystallographic Information File (CIF)" which contained information about unit cell parameters, the space group, atom positions, and thermal parameter for atoms was added in the "Phase" panel, by clicking on the button "Add Phase". Afterward, a diffraction data set was loaded using a histogram by clicking "Add Histogram" in the "Histogram" panel. For GEM neutron data analysis, three histograms were added in the following sequence detector Bank 4: Histogram 1; Bank 5: Histogram 2; Bank 6: Histogram 3.⁶

⁶Please see Figure 2.8 for the range of banks.

To load a histogram, two types of files are loaded. The first is a file containing the powder diffraction data, often called a GSAS raw data file (usually using the extension .RAW, .GSA or .GSAS) and the second file is an instrument parameter file (.INS or .INST) that defines what type of data is included in the raw file (X-ray or neutron, constant wavelength or time of flight, etc.) as well as the starting values for the diffractometer constants and peak shape parameters. The first function "Chebyshev polynomial" was used to fit the background functions. After the insertion of phases, histograms, and the background function, the fitting was started.

First, the background was fitted using an appropriate number of terms. After the background function fit, the position of peaks were fitted. The lattice parameters were refined in order to fit the position of peaks to the observed data. An instrumental parameter "difc", was included to compensate for the offset in the peak location. Constraints on the "difc" were forced in such a way that difc should be the same for all phases in one histogram, and should maintain a certain ratio to other histograms. Technically, DIFC (diffractometer constant) is related to the effective path length of the neutrons in GEM. Slight variation of the sample position causes significant changes in DIFC for the different banks. For GEM data, the bank 4 (50°—75°): bank 5 (79°—104°): bank 6 (142°—169°)::10.094: 9.08: 4.0 should maintain this ratio while fitting all histograms at one time. In the case of multiple phases, phase fractions were refined with respect to one phase fraction, i.e., one phase was given a fixed value and the other present phases were allowed to vary. However, the fraction of one phase should be the same in all histograms, therefore, a constraint was set in such a way that one phase will have one value in all histograms.

After varying a set of parameters, the fit showed that the profile shape did not fit well to the simulated data, indicating that the peak shape (broadening) parameter needed to be fit. For the GEM data, "gam-2" was allowed to vary, while for the laboratory X-ray diffractometer the X was varied to get the peak shape right.⁷ These parameters are related to a particle size broadening. Further, fitting of thermal parameters and

⁷Type 2 profile function was used.

the hydrogen site occupancy improved the fit further. These parameters influence the intensity of the peaks. The temperature factors are related to the vibrational amplitude of the atoms around their equilibrium position. The parameter " U_{iso} " in GSAS equals $U(\mathbf{Q})$ which occurs in the Debye-Waller factor (see Equations (2.25) and (2.26)), and is used to express the isotropic thermal motion of an atom. This is proportional to $\langle u^2 \rangle$ and has \AA^2 as a unit, where $\langle u^2 \rangle$ is the mean square displacement of an atom. The co-ordinate positions of atoms, which influence the peak intensity, were not needed to vary.⁸

2.7 Ab initio calculations

Ab initio calculations predict the physical properties of a system from the knowledge of only the constituent atoms and their positions. The change in the positions of the atomic nuclei leads to a corresponding change in the energy of a system giving information about the equilibrium or ground state geometry of the system. The energy of a system in electronic structure calculations can be calculated by solving the time-independent Schrödinger equation (SE)

$$\hat{H}\psi = E\psi, \quad (2.30)$$

where \hat{H} is a Hamiltonian operator, ψ is a wave function, and E are the energy eigen values. However, solving the Schrödinger equation for many electron systems is a computationally intensive process. The density functional theory (DFT), developed by Kohn and Sham [40], is based on the theory of Hohenberg and Kohn [41], and helps to solve this N -body Schrödinger equation. The theory is based on the electron density distribution $\rho(\mathbf{r})$ over position vector \mathbf{r} , instead of the many-electron wave function $\Psi(\mathbf{r}_1, \mathbf{r}_2, \mathbf{r}_3, \dots)$, where Ψ is the total wave function. This theory involves some specific approximations in order to solve the Hamiltonian equation. The Born-Oppenheimer approximation [42] is one of them, based on the fact that the mass of nuclei and electrons have a large difference and the nuclei can be considered stationary. The difference in the

⁸See the GSAS manual for details [35].

masses allows to split the Hamiltonian into nuclear and electronic parts, and to represent the wave function as the product of the electronic and nuclear parts. Consequently, the Schrödinger equation can be separated into nuclear and electronic parts. The electronic Schrödinger equation is solved as a function of the nuclear coordinates in order to find the relaxed atomic positions at equilibrium such as around vacancies and interfaces, or the local force constants related to lattice vibrations.

2.7.1 Density functional theory

Hohenberg and Kohn [41] derived that the ground-state energy of a system in the presence of static external potential $V(\mathbf{r})$, i.e., due to the atomic nuclei can be written as

$$E[\rho(\mathbf{r})] = \int V(\mathbf{r})\rho(\mathbf{r})\,d\mathbf{r} + \frac{1}{2} \int \int \frac{\rho(\mathbf{r})\rho(\mathbf{r}')}{|\mathbf{r}-\mathbf{r}'|} d\mathbf{r}d\mathbf{r}' + G[\rho(\mathbf{r})], \quad (2.31)$$

where $\rho(\mathbf{r})$ is the density and $G[\rho(\mathbf{r})]$ is a universal functional of the density [41]. Kohn and Sham wrote the term $F[\rho]$ in two parts

$$G[\rho(\mathbf{r})] \equiv \tau[\rho(\mathbf{r})] + E_{\text{xc}}[\rho(\mathbf{r})], \quad (2.32)$$

where $\tau[\rho(\mathbf{r})]$ is the kinetic energy of a system of non-interacting electrons with density $\rho(\mathbf{r})$, and $E_{\text{xc}}[\rho(\mathbf{r})]$ is the exchange and correlation energy of an interacting system with electron density $\rho(\mathbf{r})$ [40].

Kohn-Sham suggested that $\rho(\mathbf{r})$ can be calculated using the following equation

$$\rho(\mathbf{r}) = \sum_{j=1}^N \psi_j^*(\mathbf{r})\psi_j(\mathbf{r}), \quad (2.33)$$

and the wave function can be obtained by solving the one-particle SE

$$\left[-\frac{\hbar^2}{2m} \nabla^2 + V_{\text{eff}}(\mathbf{r}) \right] \psi_j(\mathbf{r}) = \epsilon_j \psi_j(\mathbf{r}), \quad (2.34)$$

where $V_{\text{eff}}(\mathbf{r})$ is given as

$$V_{\text{eff}}(\mathbf{r}) = V(\mathbf{r}) + \int \frac{\rho(\mathbf{r}')}{|\mathbf{r} - \mathbf{r}'|} d\mathbf{r}' + V_{\text{xc}}(\mathbf{r}), \quad (2.35)$$

where $V_{\text{xc}}(\mathbf{r})$ is the exchange-correlation (xc) potential [43] expressed as

$$V_{\text{xc}}(\mathbf{r}) = \frac{\delta E_{\text{xc}}}{\delta \rho(\mathbf{r})}. \quad (2.36)$$

In order to express E_{xc} energy as a functional of the density, the DFT requires an approximation such as the local density approximation (LDA) or the generalized gradient approximation (GGA).

The LDA assumes that the electron density is varying slowly [40], and the energy is a functional of local electron density only

$$E_{\text{xc}}^{\text{LDA}} = \int \rho(\mathbf{r}) \epsilon_{\text{xc}}(\rho) d\mathbf{r}, \quad (2.37)$$

where $\epsilon_{\text{xc}}(\rho) d\mathbf{r}$ is the exchange and correlation energy per electron of a uniform electron gas density (ρ).

The GGA has made an extension to the LDA by considering also the gradient of the electron density. Therefore, GGA is a functional of density and the density gradient. Mathematically, GGA exchange-correlation energies can be written as

$$E_{\text{xc}}^{\text{GGA}} = E_{\text{xc}}[\rho(\mathbf{r}), \nabla \rho(\mathbf{r})]. \quad (2.38)$$

VASP

VASP (Vienna Ab-initio Simulation Package) [44] is one of the packages used to solve Kohn-Sham equations (one-electron SE). Basically, VASP deals with different types of algorithms to achieve the energy minimization. Generally, there is one overall outer loop in the main part of the program in which the charge density is optimized with respect to convergence in the energy, and one inner loop in which the wave functions are calculated. The working of VASP can be explained as described in the flow chart (see Figure 2.9).

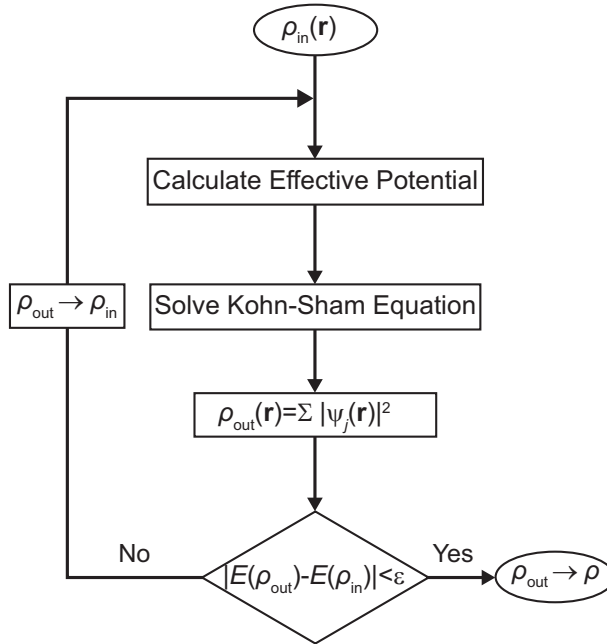


FIGURE 2.9 – A flow chart showing the successive steps in VASP and the criterion for convergence of the calculations.

VASP uses a number of input files and writes the results in output files [44]. POSCAR, POTCAR, KPOINTS, and INCAR are the files, which are necessary for all calculations. The POSCAR file contains the information about the unit cell, i.e., the lattice parameter, the lattice vectors, atomic coordinates, and the number of atoms, for each atomic species, in the unit cell. The POSCAR files gives an option to specify if a selective number of atoms should be move by mentioning *selective dynamics* before the atomic coordinate positions.⁹

The POTCAR file contains the pseudopotential for each atom present in the periodic table. VASP uses ultra-soft Vanderbilt pseudopotentials (US-PP) or the projector-augmented wave (PAW) method to describe the interaction between the ions and electrons. VASP uses periodic bound-

⁹See the VASP manual for details [44].

ary conditions on the unit cell or supercell. The KPOINTS file defines the \mathbf{k} -point grid over which the wave-functions are solved within the first Brillouin Zone using the Bloch's theorem. The number of the \mathbf{k} -points in the reciprocal unit cell is important for the accuracy of calculation, and depends on the nature of the system. A metallic system requires substantially larger \mathbf{k} -points grid than that for semiconductors or insulators. The number of \mathbf{k} -points also depends on the smearing method that is used, once not all methods converge at the same speed. In addition the error is not transferable at all, i.e., a $9 \times 9 \times 9$ \mathbf{k} -points grid leads to a completely different error for face-centered cubic (fcc), body-centered cubic (bcc), and simple cubic (sc). Therefore, absolute convergence with respect to the number of \mathbf{k} -points is necessary [44].

The INCAR file is the central input file of VASP, which determines what needs to be done, for example, in the calculations with or without ionic relaxation. After performing a calculation, output files are written, such as OSZICAR, CONTCAR, and DOSCAR containing information about the total energies, relaxed coordinates, and density of states, respectively.

2.8 Positron depth profiling

The positron (e^+) is the antiparticle of the electron, and is, therefore, also called antielectron. The positron has an electric charge of $+e$, a spin of $1/2$, and the same mass as an electron. Collimated, monoenergetic beams of positrons, with energies ranging from electron volts to kilo electron volts are very useful to study a set of key properties in condensed matter physics. When a low-energy (up to tens of keV) positron interacts with condensed matter, annihilation with an electron occurs in the sub-nanosecond timescale, resulting most often in the production of two gamma ray photons, which can be detected. This timescale gives access to important physical phenomena. The positron observables are reflected in the temporal, spatial and energetic distributions of the annihilation radiation. Before a positron reaches the annihilation stage, it undergoes a number of steps after implantation in a material.

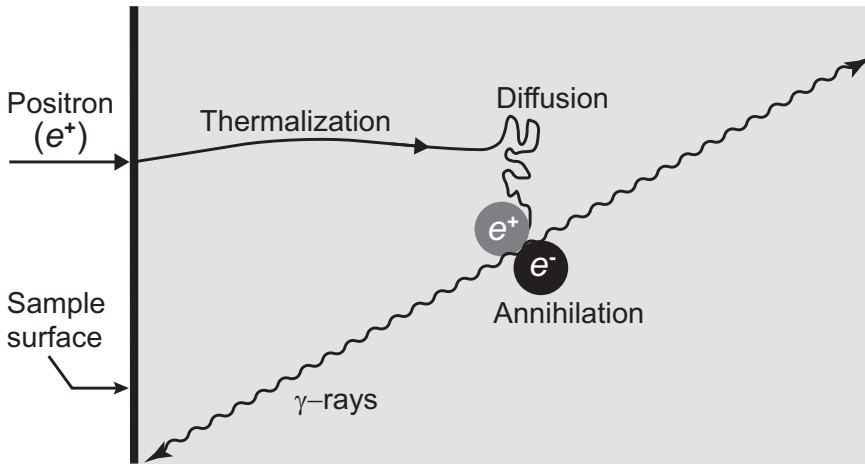


FIGURE 2.10 – Schematic diagram showing the positron annihilation process in the sample [46].

First, positrons lose their energy rapidly to electron excitations, including target atom ionizations and collective plasmon-like process, until they reach thermal equilibrium with the sample, reached usually within a few picoseconds. Then the positron continues to move based on quantum diffusion at or around thermal equilibrium. The diffusing positrons can get trapped in lattice defects which are attractive potential wells [45]. The ultimate fate for all positrons is to annihilate with an electron, resulting in two gamma-rays (see Figure 2.10). The annihilation event obeys conservation of the momentum and energy, resulting in two gamma-rays with a total energy equivalent to 1022 keV in the center-of-mass coordinate system based on the mass-energy equivalence. Therefore, the annihilation produces energy in the form of the two gamma-rays, each of 511 keV, emitted in opposite directions to conserve the momentum, which is zero in the center-of-mass frame.

However, the electron has some momentum in the laboratory coordinate system, as it is orbiting an atom resulting a Doppler shift in the energy and momentum of the gamma-ray, while a thermal positron carries a very low (negligible) momentum. This leads to a shift of opposite

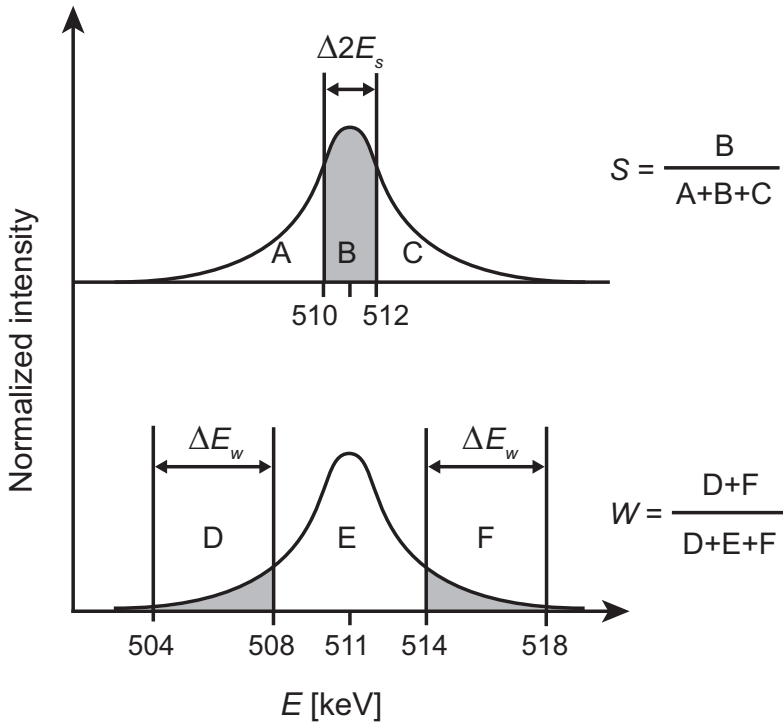


FIGURE 2.11 – Schematic representation of the definition of the shape (S) and wing (W) parameters [47].

sign in the energy of the two gamma-rays proportional to the momentum of the electron, leading to a Doppler-shift broadening of the 511 keV annihilation photo-peak. The energy spectrum of the emitted gamma-rays, which carries information about the electron momentum distribution, is collected during the experiment. Positron annihilation in single crystals provides a direct image of the electronic structure of metals and semi-conductors, nano-crystals, near interfaces and surfaces upon annihilation with electrons. The positive charge of positron makes it, furthermore, sensitive to detect atomic scale defects. Vacancy concentrations of suitable defects in which the positron can settle can be detected down to the *ppm* scale. Its incident kinetic implantation energy can easily be tuned, enabling depth-profiling studies of a large variety of sub-micron thin films.

Positrons are non-destructive, allowing in situ studies on a wide range of materials with respect to temperature.

The positron Doppler broadening of annihilation radiation (511 keV) was measured at the VEP (Variable Energy Positron) beam in-house built setup using positrons with a kinetic energy in the range of 0–25 keV. Positrons are produced using a ^{22}Na source and moderated using tungsten foils. Energy windows of $|\delta E| < 0.88$ keV and 2.57 keV $< |\delta E| < 6.62$ keV were used in the Doppler broadened 511 keV photo peak for *S* and *W*, respectively [48,49] (see Figure 2.11). Since the *S* is the signature of relatively low momentum electrons, it provides a measure of annihilation with valence electrons, providing sensitivity to the electronic structure and the presence of vacancies. *W* indicates larger deviations of the photon energy, i.e., the annihilation electron momentum is larger, therefore, *W* is a measure for positron annihilation with semi core electrons, providing chemical sensitivity to the positron trapping site via detection of deeper lying core electrons orbitals.

3

Mg thin films

The reduction in the particle and crystallite size of metal hydrides to the nanoscale has a significant effect on the kinetics of hydrogen uptake and release. Further, the addition of catalysts can improve the reaction kinetics significantly. Thin film synthesis can be used to achieve films containing nano-dimension crystallites besides ball milling. For example, Higuchi et al. [50,51] reported that Mg thin films prepared using magnetron sputtering grow in the form of columns. Their study provided clear indications that Pd facilitates the dissociation of H₂ at the surface, and lowers the hydrogen desorption temperatures significantly. Further, they also showed that the lowest desorption temperatures were observed for a sandwiched configuration of Mg films in between two Pd layers. That configuration also showed a columnar growth, but with narrower columns as compared to the case of a single top layered Pd film. They suggested that higher stress levels might have occurred due to the multilayer systems, and are responsible for the low desorption temperatures.

Therefore, it is important to investigate and clarify the role of the Pd catalyst and of the nanostructures on the sorption temperatures and kinetics during hydrogen cycling, as described in this chapter. Further, the structural transformations upon hydrogenation of Mg thin films capped with Pd are also studied in this chapter. The films were synthesized

using two different deposition methods, namely PSD and PLD. TEM, SAD, and XRD reveal the formation of MgPd and Mg₂Si (magnesium silicide) alloys, and further show the details of the phase transformation of (hexagonal closed-packed) hcp-Mg to rutile-MgH₂. The hydrogen sorption studies show that the Mg films can be loaded up to 4 wt.% already at 200 °C for an applied pressure of 2.5 bar for 2 h. The full capacity of 7.6 wt.% can be reached with the application of 10 bar pressure for 24 h at this low temperature. Additionally, the hydrogen sorption studies also revealed a peeling-off of the Pd-cap layer at temperatures higher than 250 °C, leading to a significant decrease in the apparent storage capacity. This indicates the importance of the Pd catalyst for the hydrogen sorption process. Further, the permeation studies showed that the hydrogen transport kinetics is rate limited by the dissociation of hydrogen molecules at the sample surface, and indicate that the Pd catalyst acts as a H₂ splitter at the surface. Moreover, the change in the electronic structure upon hydrogenation can be extracted from positron studies, which also showed the occurrence of Mg-Pd alloy formation and the hcp-Mg to rutile-MgH₂ transformation.

3.1 Experimental details

Mg thin films with a thickness of around 0.5 and 1 μm were deposited using PSD and PLD techniques. In the PSD, Argon gas and a mixture of Ar + H₂ gases, within a pressure range from (1–3) × 10⁻⁶ bar, were used for the plasma, which was created using an electron gun. Hereafter, a high negative potential on the target, -1000 V and -500 V on Mg (99.9%) and on Pd targets, respectively, was applied. During the sputtering, heavy Ar⁺ ions hit the target, knock out Mg atoms and deposit these on the substrate (For details, see Section 2.2.1). A Pd target was placed on the top of the shutter to enable the deposition of a Pd thin film on top of the Mg film in the same set up, avoiding possible oxidation [30]. The films were deposited on a Si (100) or on a glass substrate. PLD, the other technique, was used to deposit Mg films on a Si (100) substrate positioned opposite the target (For details, see Section 2.2.2). After deposition of Mg

films, the samples were transferred to the PSD setup for capping the Mg films with a Pd layer with a thickness of about about 50—100 nm.

The as prepared PLD films were characterized by X-ray diffraction with the Cu K_{α} wavelength, 1.54 Å, using a Bruker-AXS Type D5005 diffractometer. Co K_{α} radiation, wavelength of 1.79 Å, was used to characterize the sputter deposited films using another Bruker-AXS Type D5005 diffractometer. Cross-sectional TEM was carried out on selected films to study the structural properties of the films using a Philips CM30T microscope at 300 kV. Additionally, SAD images were obtained on cross-sections of the films using a beam spot size equivalent to about the thickness of the film.

Hydrogen permeation experiments were carried out to study the hydrogen kinetics and permeation through the films using a standard hydrogen permeation set up with a quadrupole mass spectrometer (QMS), a Pfeiffer QME 200, as a sensitive hydrogen detector. For these experiments, films were prepared on a highly permeable 50 μm thick PdAg25 substrate instead of Si (001).

Hydrogen loading was carried out in a hydrogen oven in the pressure range of 2.5 to 10 bar and at temperatures ranging from 25 to 400 °C for 2 to 24 h. The thicknesses of the sputter deposited films were determined using a Dektak-8 profilometer with an accuracy of roughly 0.05 μm . The known film thickness and area were used to determine the amount of Mg deposited, needed in the extraction of its hydrogen capacity. The densities of these flat films were assumed to be 1.7 g cm^{-3} , i.e., close to the density of bulk Mg. The weight of these films was also checked by weighing a few selected samples before and after the deposition. The deposited amount of Mg for laser deposited films with an area of 1.3 cm^2 , on the other hand, was only determined using the weighing method directly, within an accuracy of 0.015 mg for Mg films with a typically weight of 0.20 mg. Their partially porous character and the presence of micron scale chunk particles on top of these films prohibits a reliable use of the first method. The hydrogen contents of the loaded films were obtained from subsequent hydrogen desorption measurements using the HYDRA setup (see Section 2.5). Hydrogen desorption spectra and the main desorption

temperatures were determined in heating runs using a linear variation of sample temperature at roughly $5\text{ }^{\circ}\text{C min}^{-1}$, carried out in a vacuum of approximately 10^{-7} bar. The composition of the gas released from the sample was regularly checked and determined using a QMS.

The positron Doppler broadening of annihilation radiation (511 keV) was measured using positrons with a kinetic energy in the range of 0–25 keV (see Section 2.8). The S parameter depth profiles were analyzed using the VEPFIT software package. This program solves the full positron implantation-diffusion problem for a system of layers, and the calculated S curves were fitted to the experimental data. The fitting parameters such as the S parameter of the respective layer, the thickness of the film, and the positron diffusion length for each layer with a given mass density were allowed to vary.

3.2 Plasma sputter deposited films

3.2.1 Structural characterization

The films were characterized after the preparation by XRD using Co K_{α} radiation. Generally, the sputtered films (using Ar gas plasma) show a preferred orientation of hexagonal \mathbf{a}_3 -axis, Mg (0002), perpendicular to the Si (001) substrate. This confirms that the Mg films grow according to the commonly observed growth mode with the Mg hexagonal basal plane parallel to the Si substrate plane [52,53]. Microstructural properties of the films were studied using TEM. Figure 3.1 shows a cross-sectional TEM image of a sputtered film before hydrogenation. The boundary between the Mg and Pd layers is very apparent. A clear columnar structure is visible for the sample in Figure 3.1, which extends throughout the film thickness. Each column contains grain boundary defects, while the columns have a number of different orientations, discernible by gray shading of columns, relative to each other. This small variation in the orientation of the columns relative to each other leads to a small spread in the corresponding diffraction spots in SAD. These different orientations could be caused by rotations of the columns during the growth of the films, indicating the presence of open space between the columns enabling such

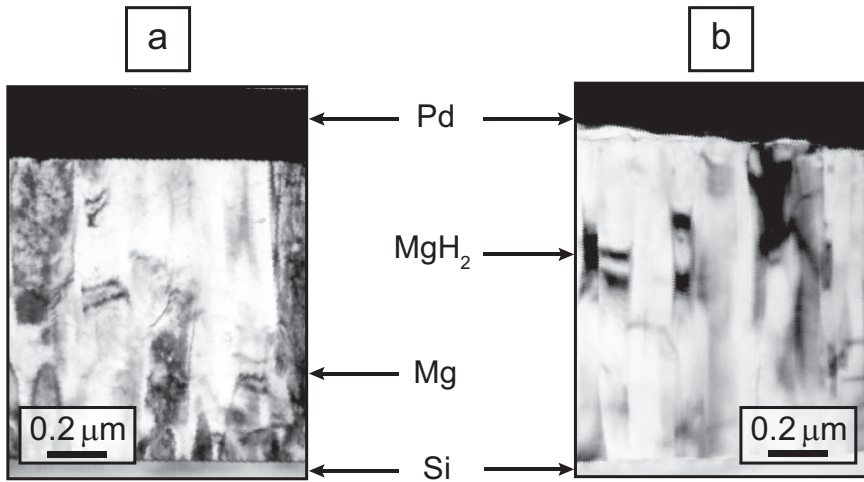


FIGURE 3.1 – Cross-sectional TEM images of (a) as prepared; and (b) hydrogenated Mg films on a silicon (001) substrate prepared in the same batch by plasma sputtered deposition using an argon gas plasma.

motions. Sputtered films were hydrogenated at 200 °C at 2.5 bar of hydrogen pressure in an oven for 2 h. The hydrogenation resulted in a clear reduction of defects and release of stresses during the phase transformation of the hcp-Mg to the tetragonal (rutile)-MgH₂, leading to a better visibility of the columns (Figure 3.1)

Likely, this is caused by the passage of the Mg and MgH₂ phase boundary, leading to a recrystallization and a relaxation of the crystal structure, and a corresponding removal of crystal lattice defects. Inelastic neutron scattering measurements on ball milled MgH₂ powder showed a similar result, i.e., a release of stresses of ball milled Mg powder upon hydrogenation [54]. The XRD showed that a martensitic-like phase transformation from Mg to MgH₂ occurs with an orientation relationship of Mg (0002) || MgH₂ (110), similar to as mentioned by Higuchi et al. [51]. SAD on sputtered films before and after hydrogenation confirms the formation of rutile-MgH₂ upon hydrogenation of Mg films. The SAD diffraction patterns (not shown) show a series of spots, corresponding to grains having different orientations (of the order of ten). This is caused by (a)

the three orientations defined by symmetry in which the hcp-Mg (0002) structure converts into the rutile-MgH₂ (110); (b) small rotations of individual columns relative to each other; and (c) loss of epitaxy relative to the Si (001) substrate, as also observed for PLD films (see section 3.3.2).

3.2.2 Pd as a hydrogen splitter at the surface

Hydrogen permeation experiments were carried out on the sputter deposited Mg films to reveal the nature of the hydrogen kinetics, surface or diffusion controlled, and the effects of Pd capping Mg films. The time-resolved permeation (not shown) through Mg films on PdAg25 substrates was followed upon application of a hydrogen pressure of approximately 50 mbar on the upper Mg side of the films. The study demonstrated that the presence of a Pd capping layer improves the hydrogen kinetics and permeation substantially [30]. Notably, the use of Pd cap layer showed an increase in the observed equilibrium fluxes J_{∞} by a factor of the order of 10^3 compared to bare Mg films.

At 250 °C, the hydrogen permeation through the activated nanostructured Mg layers stabilized within less than 500 s to reach its equilibrium flux J_{∞} , which is 4 times faster than without a Pd cap layer. The hydrogen transport kinetics for both bare Mg films as well as for Pd capped Mg films was observed to be rate-limited by the hydrogen dissociation at the sample surfaces. Namely, the equilibrium flux J_{∞} showed a power law dependence on the applied hydrogen pressure p on one side of the film, with an exponent typically close to 1 (for example, see Figure 3.2(a)). Bare Mg films showed a similar behavior as shown in Figure 3.2(a), however, with largely reduced equilibrium fluxes J_{∞} at the applied temperatures above 300 °C.

The PdAg25 substrates, on the other hand, showed a very fast hydrogen transport kinetics, limited by diffusion through the film; the permeation here follows a power law dependence with an exponent of close to 1/2 (see Figure 3.2(b)), obeying Sievert's law [55]. The Mg films were apparently too thin to show kinetics limited by diffusion, and kinetics is limited by the surface dissociation (H₂ splitting) process.

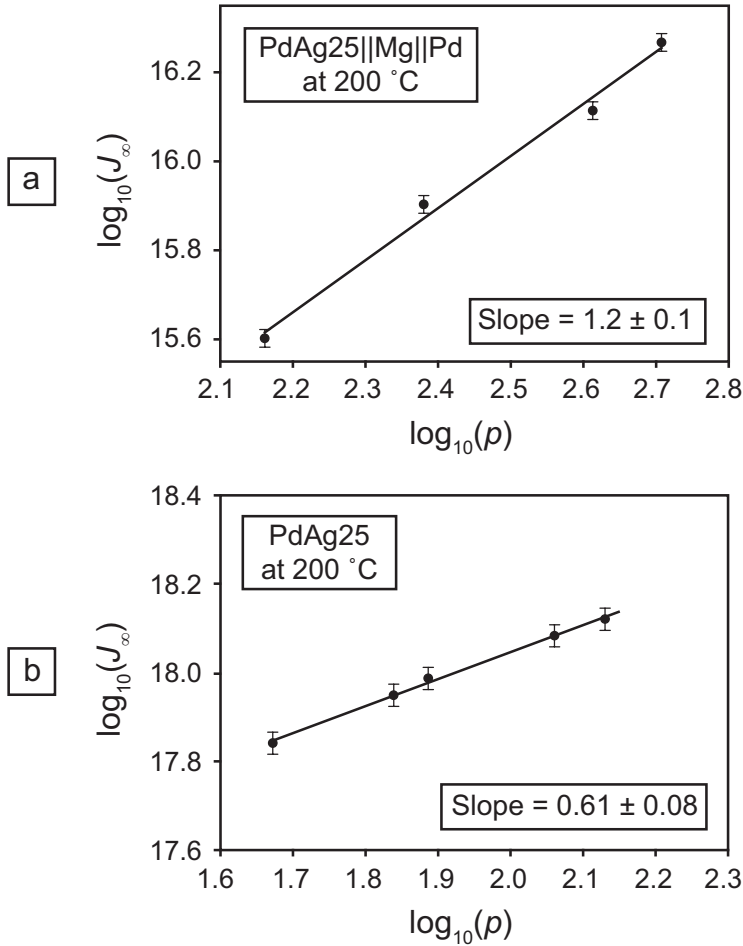


FIGURE 3.2 – Equilibrium hydrogen permeation flux (J_∞ in hydrogen molecules $\text{cm}^{-2} \text{s}^{-1}$) plotted against equilibrium hydrogen pressure (p in mbar) at a temperature of 200 °C for (a) a PdAg25|Mg|Pd multi-layer; and (b) a bare PdAg25 substrate. The membranes were externally activated.

3.2.3 Pd reduces hydrogen sorption temperatures

Further, a number of samples were studied for which hydrogen was incorporated into the films during the sputter deposition. This was achieved

by using a gas mixture of Ar and H₂ having a ratio of 1:1 at a pressure range between $(1-3) \times 10^{-6}$ bar. Electron microscopy images showed that the films contain generally more grains, while keeping the columnar growth. Furthermore, the average width of the columns decreases from 100 nm to 40 nm upon application of a bias voltage on the substrate in the range between 0 to -100 V. These changes are attributed to resputtering of Mg atoms during deposition of the films.

This seems to be consistent with a reorientation of the grains from the preferred Mg (0002) growth to a preferred Mg (10 $\bar{1}$ 0) orientation observed for samples prepared at the highest applied bias voltage of -100 V, as shown in Figure 3.3. The XRD pattern for samples prepared using a mixed Ar + H₂ plasma clearly show the presence of a MgH₂(110) diffraction peak besides the stronger Mg (0002) peak, showing that the reactive sputtering leads to incorporation of hydrogen in the films.

The area of MgH₂ (110) peak, nevertheless, reduces significantly relative to the area of Mg (0002) peak in the bias voltage range from 0 to -75 V. Figure 3.4(a) shows that this is consistent with the incorporated hydrogen fraction (in wt.%) determined in the subsequent hydrogen desorption experiments. The figure shows a substantial decrease in the hydrogen fraction from 3.0 wt.% (at 0 V) to 0.2 wt.% (for bias voltages larger than -25 V). The 3.0 wt.% is equivalent to $x \approx 0.8$ on the average for the MgH_x film. The increased width of the Mg (0002) diffraction peak in this high voltage range indicates that this is accompanied by a reduction in Mg grain sizes. SAD images confirmed these structural changes, as at 0 V a polycrystalline character is observed, while at -75 V partial amorphization occurs. The combination of these observations shows the importance of the resputtering process. This possibly enables the easier escape of hydrogen from these films through the presence of defects and a larger amount of grain boundaries.

The more polycrystalline character of the film has a significant impact on the hydrogen desorption temperature for bare Mg films (see Figure 3.4(b)), resulting in a systematic reduction from 410 °C down to 370 °C upon increasing the applied substrate bias voltage. Such easier hydrogen desorption can originate from modifications at the sample surface and

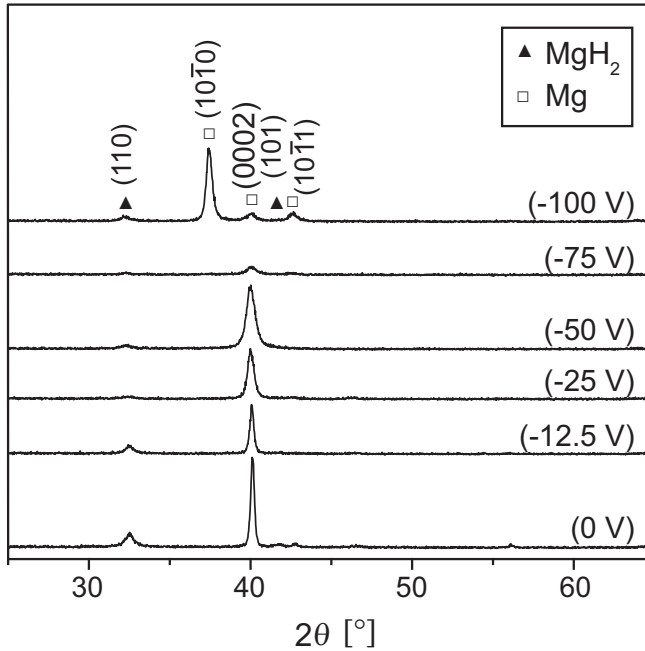


FIGURE 3.3 – XRD patterns (using Co $K\alpha$) of Mg films prepared using reactive Ar and H_2 sputtering at different bias voltages on the substrate, showing the presence of both MgH_2 and Mg diffraction peaks.

at the grain boundaries. The presence of a large amount of defects is most likely affecting the hydrogen migration energy, which may attain a lower value. Consequently, hydrogen desorption can occur at the lower observed temperatures.

Capping the film with a Pd top layer, on the other hand, has a far more important effect on the hydrogen desorption temperature. The latter decreases to about $200\text{ }^\circ\text{C}$, and remains nearly independent of applied substrate bias voltage. This clearly shows that, for these $1\text{ }\mu\text{m}$ thin Mg films, the catalytic activity of the Pd cap layer is the dominant factor in determining the hydrogen kinetics and sorption temperatures rather than the nanostructured character of the film.

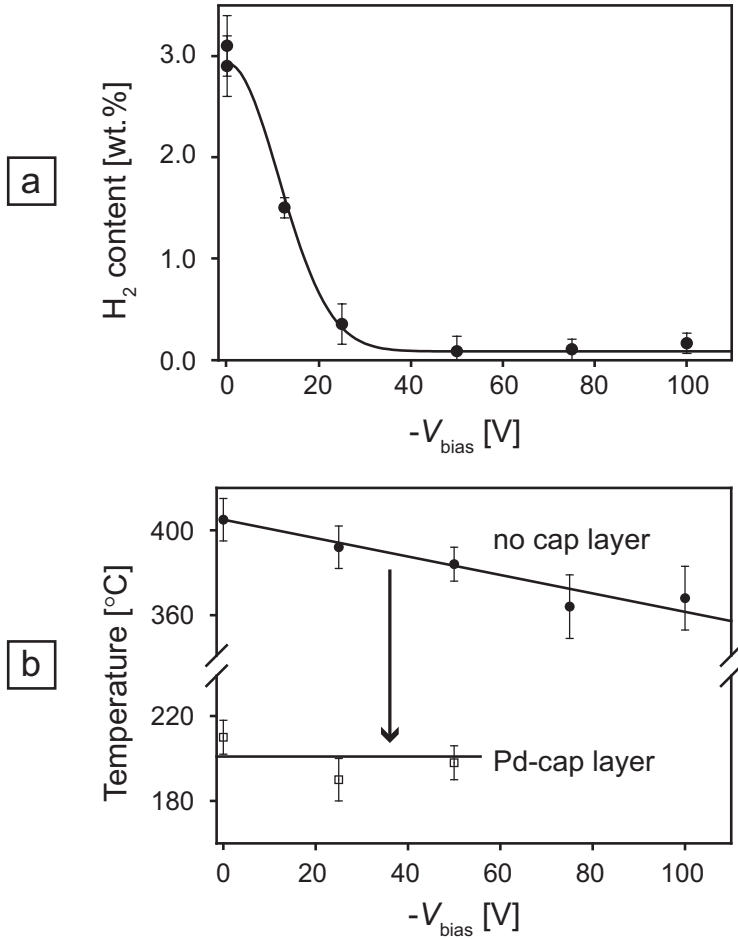


FIGURE 3.4 – (a) Hydrogen fraction (in wt.%) incorporated in Mg films during plasma deposition using a mixed Ar and H₂ plasma; and (b) hydrogen desorption temperature versus substrate bias voltage for bare and Pd-capped sputter deposited Mg films prepared using a mixed Ar and H₂ plasma.

3.2.4 Storage properties

Hydrogen loading of sputter deposited films were done at various temperatures in the range of 25–400 °C under 2.5 bar hydrogen pressure for

2 h in an oven to investigate the role of the Pd-cap layer further, using similarly prepared pristine samples for each loading temperature. For a few films, a hydrogen pressure of 10 bar was used at 24 h for the loading. Subsequently, the absorbed hydrogen fraction was determined by hydrogen desorption measurements. Figures 3.4(b) and 3.5 show the presence of the Pd catalyst reduces the onset of the hydrogen release and uptake temperatures to 200 °C.

A maximum hydrogen capacity was already achieved at 220 °C under 2.5 bar of hydrogen pressure for 2 h. The theoretical maximum of the hydrogen capacity of 7.6 wt.% was achieved at 220 °C using 10 bar hydrogen pressure for 24 h, corresponding to a full conversion of Mg to MgH₂. Loading at 280 °C or higher, on the other hand, reduces the reversible hydrogen fraction significantly (see Figure 3.5). This reduction in the hydrogen fraction at higher temperature might have resulted because of the partial detachment of Pd layer from the Mg layer, which was observed for temperatures above 270 °C, as shown in the optical microscope image (see Figure 3.6).

This delamination of the Pd layer might have been caused because of the difference in the thermal coefficients of expansion of the Pd and Mg [56]. The major cause for the delamination, however, seems to be the large expansion in volume of close to 31% for the Mg film upon hydrogenation, and the release of the corresponding build up of stresses at the MgH₂-Pd interface. This was verified in a reference experiment, in which samples prepared in the same batch were exposed to 2.5 bar of pressure in different gas atmospheres, hydrogen and (inert) He, at 250 °C for 3 h.

A clear delamination of the layer was observed in the case of the hydrogen exposed sample, while the helium (He) exposed sample did not show any sign of delamination. This is also confirmed by positron studies on such types of films (see Section 3.2.5). Clearly, after the detachment of the Pd layer, the hydrogen molecules need to dissociate at the Mg surface rather than at a neat Pd surface. Therefore, the hydrogen gas has to overcome a correspondingly larger energy barrier in order to dissociate, leading to the observed lower absorbed hydrogen fraction, or, equivalently, higher loading temperatures (see Figure 3.5). These observations

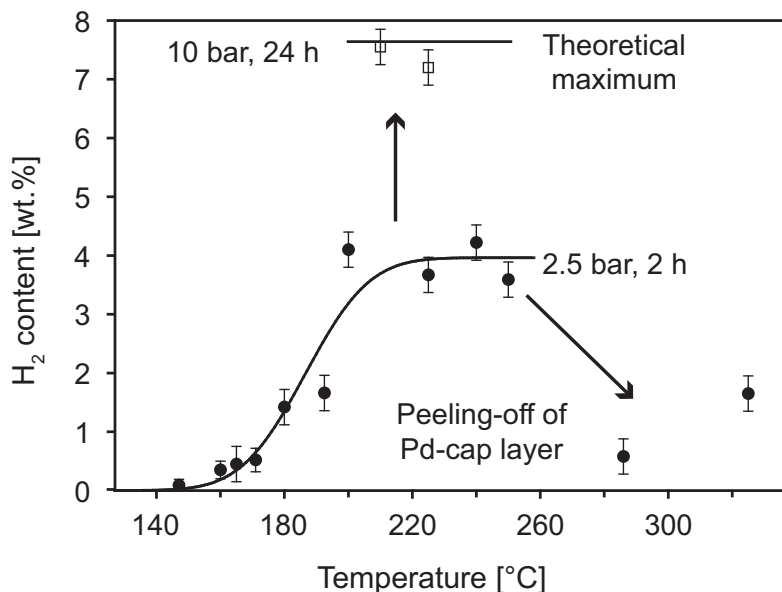


FIGURE 3.5 – Hydrogen uptake for sputter deposited Pd-capped Mg films over a range of loading temperatures, showing that the maximum uptake of approximately 7.6 wt.% (MgH_x , $x \approx 2$) is reached at 220 °C and 10 bar. Heating above 250 °C resulted in a lower hydrogen uptake due to peeling-off of the Pd cap layer.

show that the Pd cap layer plays an important role as a catalyst to dissociate H_2 molecules at the sample surfaces, leading to significantly reduced sorption temperatures.

3.2.5 Positron analysis

Positron studies were performed to investigate the metal (Mg) to insulator (MgH_2) electronic structure transition. Positron depth-profiling studies were carried out on as prepared and hydrogenated Pd-capped Mg films prepared on a glass substrate. Additionally, this study gave an insight in the partial delamination of Pd-cap layers at higher temperatures and in the Pd-Mg alloy (Mg_2Pd) formation.



FIGURE 3.6 – Optical microscope image of a sample heated to 300 °C showing the peeling-off of the Pd cap layer.

Metal to insulator transition

Figure 3.7(a) shows a representative positron depth profile of the Doppler S parameter for as deposited and hydrogenated Mg thin films. The three regions correspond to the 5 nm Pd cap layer, the nearly 500 nm Mg metal (hydride) layer, and the glass substrate. Upon hydrogenation, a large change in the S parameter in the second layer occurs, which is associated with the formation of the metal hydride. The solid lines in Figure 3.7(a) represent the fit using VEPFIT analysis [57] of the Doppler depth profiles.

Figure 3.7 shows that the S parameter decreases substantially upon loading of Mg films with hydrogen i.e., upon formation of MgH_2 . Notably, the W parameter stays nearly constant upon hydrogenation. The $S - W$ values return to their original values upon low temperature loading and subsequent desorption. The large reduction in Doppler S parameter upon hydrogen loading of Mg is mainly due to the metal (Mg) to insulator (MgH_2) electronic structure transition. The electronic state of valence electrons will be different for Mg and MgH_2 phases. Based on a Compton scattering study on Mg and MgH_2 powders [58], the reduction is primarily related to the change in valence electron momentum distributions of the bulk metal and metal hydride systems, as supported by

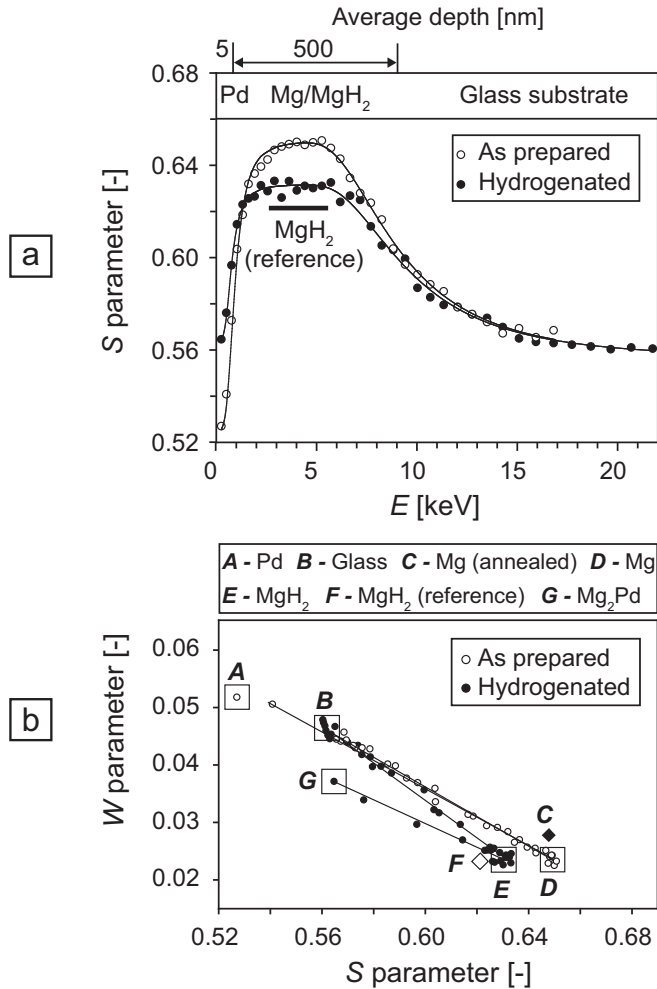


FIGURE 3.7 – (a) Doppler S parameter depth profiles for as deposited Pd capped Mg films and subsequent hydrogen loading. The decrease in the S parameter value shows the metal (Mg) to insulator (MgH₂) transition; and (b) corresponding $S - W$ parameter diagram. The $S - W$ point for MgH₂ (reference) was estimated, see text, while the $S - W$ point for Mg (reference) was obtained on a well-annealed Mg bulk sample.

the calculated momentum distributions of valence electrons in Mg and MgH₂. The fraction of valence electrons in the experimental momentum interval of $|\mathbf{p}| < 3.5 \times 10^{-3}m_0c$ ($|\delta E_S| < 0.88$ keV), used in the Doppler study, is estimated from the calculations about 7% lower for MgH₂ relative to Mg [59]. The estimation was done using the theoretical momentum distributions convoluted with the resolution of 1.2 keV of the Doppler broadening measurements. This is close to the decrease of about 4.5% seen in positron experiments as discussed below.

This difference can be discerned in the depth profile, as can be seen in the S and W parameter. Figure 3.7 shows a large change in the S parameter $\Delta S = -0.03 S$, while the W parameter $\Delta W = 0$ remains nearly constant. The estimated change in Doppler S parameter for the complete transformation of Mg to MgH₂ is $\Delta S = -0.045 S$, since a phase fraction of approximately 63% (5 wt.% hydrogen loading) of the Mg film only was converted to MgH₂. This fraction was extracted from the XRD on Pd-capped Mg films before and after hydrogenation. The value of $\Delta S = -0.045 S$ is close to the reduction of about 5% reported by Checchetto et al. [60]. The remaining difference with $\Delta S = -0.07 S$ estimated from the ab initio calculations can be related to the details of the spatial overlap of the positron wave function with the valence electron orbitals, which are not included in these calculations, or to positron trapping in small vacancy clusters at the boundaries of columns in the Mg films. Positron trapping in hydrogen vacancies in the MgH₂ cannot strictly be excluded at this point, although the hydrogen vacancy formation energy for MgH₂ is relatively high, 1.6 eV for a neutral vacancy [61]. Therefore, appreciable vacancy concentrations in MgH₂ are not expected in the temperature interval considered in this study.

MgPd alloy formation

Further, the positron studies gave additional information about the formation of Mg-Pd alloy at the Mg-Pd interface. The XRD patterns on the same film showed the formation of Mg₂Pd due to Pd diffusion into the underlying Mg, occurring already at temperatures of 210 °C. Positron depth-profiles and $S - W$ diagrams on the thin film samples show a cor-

responding large shift in the $S - W$ parameters at low positron implantation depths from the Pd toward the Mg–Pd characteristic $S - W$ point (Figures 3.7 and 3.8, points *A* and *G*), revealing the cap layer transformation to Mg_2Pd .

Further, a high fraction of ortho-positronium (o-Ps) with a slow decay with positron implantation energy was observed for the samples which were loaded at 230 °C and unloaded up to 330 °C. The o-Ps was formed at the interface of Pd cap and Mg layer [59]. This indicates that a partial delamination of the 5 nm cap layer occurred for hydrogen cycling in the higher temperature range around 300 °C, leading to a loss of its catalytic activity and an incomplete desorption of hydrogen from the metal hydride layer. In summary, positron depth profiling, therefore, not only provides insight in the role and transformation of the catalyst used to promote hydrogen storage in metal hydrides, but may also be helpful for in situ monitoring of the catalyst and metal hydride layers [62].

3.3 Pulsed laser deposited films

3.3.1 XRD characterization

Pulsed laser deposition method is another technique, which was used to prepare Mg films of similar thickness ($1\mu m$). XRD measurements on as prepared laser deposited Mg films show three diffraction peaks corresponding to the Mg (0002), Mg ($10\bar{1}1$), and Mg ($10\bar{1}0$) orientations (see Figure 3.9), while a single Mg (0002) diffraction peak was observed for sputter deposited Mg films. This indicates that laser deposited films are textured in nature with differently oriented grains in which the (0002), ($10\bar{1}1$), ($10\bar{1}0$) crystal planes are parallel to the silicon (001) substrate, respectively. Apparently, the energetically ejected material and the discontinuity of the laser deposition process give rise to such textured films. Subsequently, the Pd-capped films were loaded at 250 °C and 2.5 bar for 10 h. The XRD studies (see Figure 3.9) showed only MgH_2 peaks upon hydrogenation, indicating the full transformation of the Mg crystallites into MgH_2 under these loading conditions. In contrast, the XRD pattern of films that were hydrogenated at 150 °C and 2.5 bar for 10 h showed

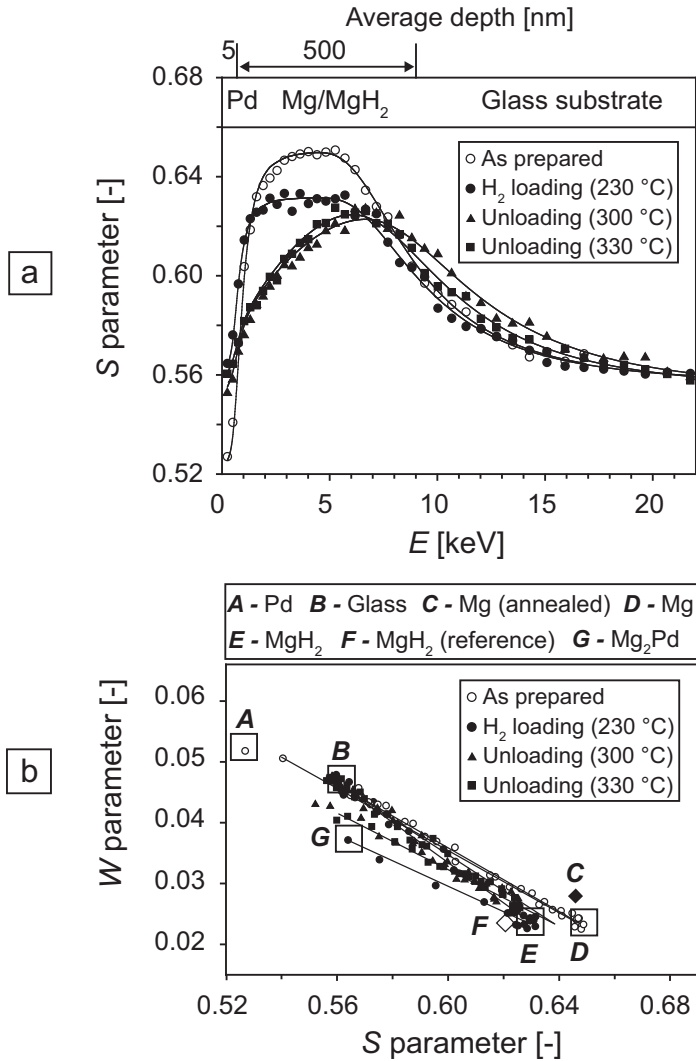


FIGURE 3.8 – (a) Doppler S parameter depth profiles for a Pd-cap Mg film for a selected sample before and after H₂ loading, and subsequent desorption up to 300 and 330 °C; and (b) the corresponding S – W parameter diagram.

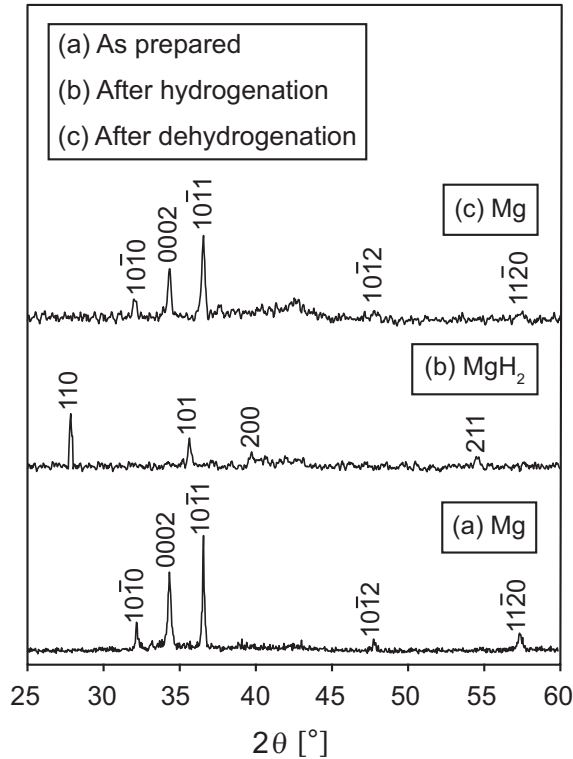


FIGURE 3.9 – XRD patterns (using $\text{Cu K}\alpha$) of laser deposited (a) as prepared Mg film; (b) MgH_2 film obtained by hydrogenation at 250°C and 2.5 bar for 10 h; and (c) after dehydrogenation, showing that the original Mg structure is retrieved.

a weak Mg (0002) peak along with MgH_2 peaks. This indicates that Mg was transformed only partially into MgH_2 under these loading conditions. Dehydrogenation up to 300°C of the films, which were loaded at 250°C , resulted in a transformation back to the original Mg structure (see Figure 3.9), suggesting that H_2 cycling is feasible. However, the absorbed H_2 content reduced close to 30% after only a few cycles. This is likely related to the onset of detachment of the top Pd layer, observed previously for the sputtered deposited films (see Figure 3.6 and 3.5), inducing a clear shift in the H_2 sorption temperatures to higher values.

3.3.2 Microstructure studies

Electron microscopy showed that laser deposited Mg films grow in quite a similar manner as sputter deposited films, showing a similar columnar structure extending throughout the thickness of the films (see Figure 3.10). The laser deposited Pd-capped Mg films showed a thick MgO layer at the interface of Mg and Pd. The latter was formed during the transfer of Mg film samples from a PLD setup to the sputter deposition setup to deposit the Pd cap layer. Such a thick MgO layer acts in general as an undesirable barrier to hydrogen absorption. Figure 3.10 shows a penetration of Pd in some parts of the film due to porosity of the deposited Mg film. Additionally, the laser deposited Mg films showed the presence of large chunks on the surface of the film, which were created along with the atomically dispersed evaporation plume when the laser beam hit the target material. Subsequently, these chunks were deposited on the substrate or films, as was also observed in scanning electron microscope (SEM) imaging of as prepared Mg films, similar to the study of Mosaner et al. [33]. The crystal structure and composition of the chunks and their behavior toward hydrogen absorption could not be determined in the electron microscopy studies. The density of the chunks can be reduced significantly by increasing the distance between the target and the substrate, as observed in SEM images (not shown).

Additionally, a variety of grains with slightly different orientations is present inside the film (see Figures 3.10 and 3.11). Furthermore, Figure 3.10(a) shows the presence of strains in the columns, and the columns are less well defined as compared to sputter deposited films (Figure 3.1). Still, these columns contain a significant number of polycrystalline and grain boundary defects. These defects may facilitate hydrogen absorption because they may reduce the migration energy, as discussed for the sputter deposited films prepared under an application of substrate bias voltage in section 3.2.3. Figure 3.10 shows that the columns are better visible after hydrogenation at 250 °C at 2.5 bar for 10 h, which is similar to the sputter deposited films. This is caused by release of stresses in the film during the transformation of the hcp-Mg into tetragonal MgH₂. After hydrogenation, electron microscopy studies on a typical laser deposited film

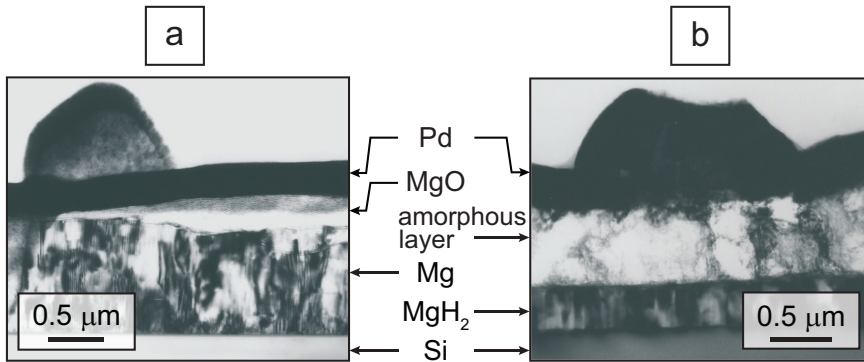


FIGURE 3.10 – TEM micrographs of (a) as prepared; and (b) hydrogenated Pd-capped Mg film prepared in the same batch by PLD in an argon atmosphere.

showed a two-layer structure instead of a single MgH₂ layer (Figure 3.10). SAD confirms that the bottom layer close to the silicon substrate consists of MgH₂ only. The intermediate layer shows some amorphous structure; the SAD images suggest that this layer might be a mixture of MgH₂ crystallites, Mg, and MgO phases.

MgPd alloy formation

The SAD images in Figure 3.11 reveal the presence of a series of weak diffraction spots, indicating the presence of an additional phase having a lattice parameter of 3 Å in the intermediate layer. The most probable phase giving rise to these spots is (body-centered cubic) bcc-MgPd having the CsCl crystal structure ($Pm\bar{3}m$) with a reported lattice parameter of 3.17 Å [63]. The MgPd phase is different from the Mg₂Pd phase observed for PSD films (see Section 3.2.5). This difference may arise due to different conditions such as the applied pressure, the temperature, and the amount of the Pd and Mg in the film. As mentioned earlier, Pd penetrates in parts of the laser deposited film through the pores. Apparently, intermixing of Pd and Mg leads to subsequent MgPd alloy formation.

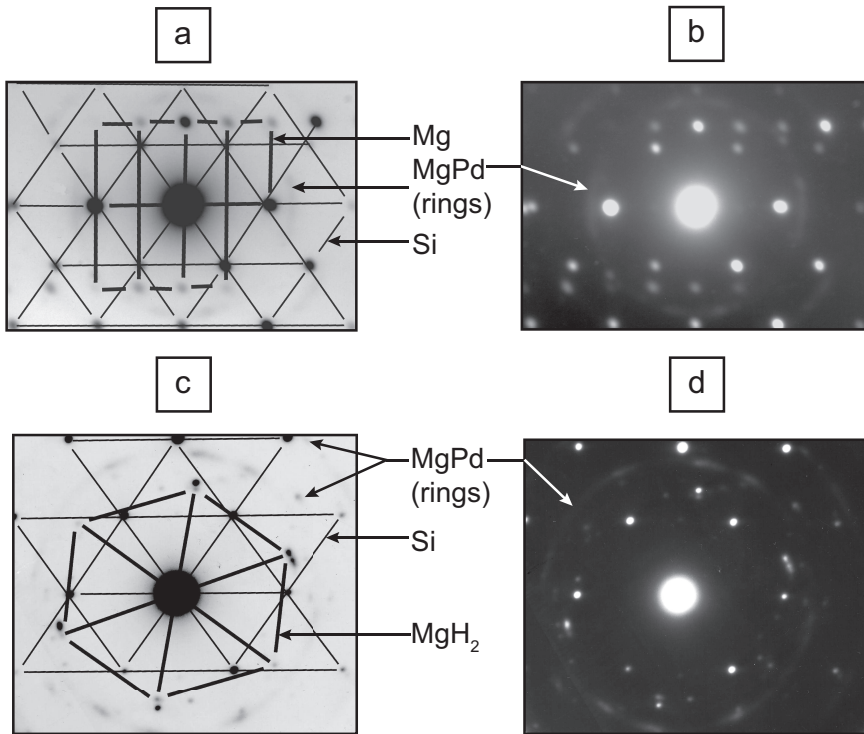


FIGURE 3.11 – SAD images of laser deposited films. (a) and (b) as prepared Mg film; (c) and (d) hydrogenated film, revealing the presence of MgH₂ and weak spots of bcc-MgPd formed in the intermediate layer of the hydrogenated film.

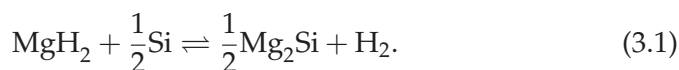
The diffraction pattern in Figure 3.11 of an as-prepared film corresponds to nearly single crystalline hcp-Mg with a small spread of diffraction spots. The latter suggests that the columns are slightly rotated with respect to each other, as found previously for the sputter deposited films. SAD on the hydrogenated Mg films shows diffraction spots from MgH₂, a trivial contribution from the Si (001) substrate, and weak spots from the bcc MgPd phase (see Figure 3.11). SAD at a significantly narrower focus of the incident electron beam, enabling to selectively probe the 150 nm thin bottom layer was also performed. This demonstrated that the bottom layer consists of fully hydrogenated MgH₂ (110). The SAD results

show that the hcp-Mg structure is rearranged into the tetragonal MgH_2 structure obeying closely the orientation relationship $[2\bar{1}10] \text{Mg} \parallel [111] \text{Si} \parallel [111] \text{MgH}_2$; $\text{Mg} (0002) \parallel \text{Si} (002) \parallel \text{MgH}_2 (110)$ upon hydrogenation. Furthermore, Figure 3.11 shows that hydrogenation is accompanied by a loss of epitaxy, as the $\text{MgH}_2 (110)$ plane is not exactly parallel to the $\text{Si} (002)$ plane, while the $[111] \text{MgH}_2$ direction stays nearly parallel to $[111] \text{Si}$.

There are indications that the two-layer structure (see Figure 3.10) with a bottom layer consisting of ordered MgH_2 is related to a possible start of the hydrogenation process at the interface of the Mg film with the Si substrate. Such a hydrogenation process starting at the interface with the substrate recently was observed for Mg_2Ni layers [64, 65]. This process involves dissociation of hydrogen molecules at the Pd surface, and a subsequent diffusion of hydrogen atoms through the Mg film to the Si substrate, enabling the nucleation of the MgH_2 phase at the Mg–Si interface.

Mg_2Si alloy formation

The formation of a Mg_2Si phase was also observed at the Mg–Si interface in this type of films (see Figure 3.12) at higher temperatures. An XRD pattern was obtained for a sample in which the Mg film was peeled-off from the $\text{Si} (001)$ substrate upon hydrogen desorption up to 400°C , which shows clearly the presence of Mg_2Si . Mg_2Si formation at Mg–Si interfaces reportedly may occur for temperatures above roughly 200°C [66, 67]. Mg_2Si itself is, in principle, an interesting system for hydrogen storage, as was recently suggested by Vajo et al. [24]. The low formation of enthalpy $\Delta H = -36.4 \text{ kJ mol}^{-1} \text{H}_2$ in the reaction (see Equation (3.1)) infers that hydrogen plateau pressures of the order of 1 bar could be reached near room temperature (see Chapter 6)



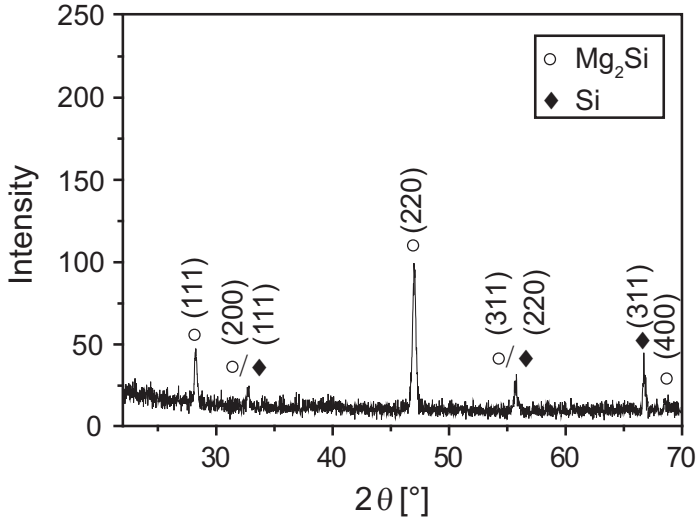


FIGURE 3.12 – XRD pattern (using Co $K\alpha$) for a sample for which the Mg film was peeled-off from the substrate during H_2 desorption up to 400 °C, showing the formation of Mg_2Si at the Mg–Si interface.

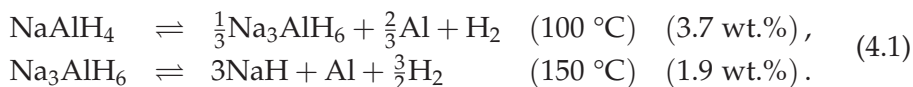
3.4 Conclusions

Pd-cap layers play a key role as a catalyst in enhancing the rate-limiting dissociation of H_2 molecules at the sample surface of Mg films, lowering the H_2 sorption temperatures significantly. While the desorption temperatures decrease with a reduction in column width for bare Mg films, the use of a Pd-cap layer is the dominant factor in determining the H_2 kinetics and H_2 sorption temperatures. H_2 cycling studies on PLD films showed that the maximum absorbed hydrogen fraction reduces clearly within a few H_2 cycles only, which relates to the observed delamination of the Pd layer. The formation of Mg–Pd and Mg–Si alloys was observed at the Pd–Mg and Mg–Si interfaces for temperatures above 200 °C, resulting in the formation of Mg_2Pd , bcc-MgPd and Mg_2Si , which may possibly affect the hydrogenation processes. Further, positron studies on the PSD films confirm the Mg (metal) to MgH_2 (insulator) transformation, and reveal the delamination of ultra-thin Pd-cap layers and Mg–Pd alloys formation.

4

Catalyzed and uncatalyzed NaAlH₄

rystallites of nano-size dimensions reduce the required transport distances of hydrogen and metal ions. Further, the presence of vacancy-related defects may facilitate the diffusion of atoms in metal hydrides. Therefore, one possible approach to improve the reversibility of the sorption reactions is the maintenance of crystallite sizes to the nanoscale during hydrogen cycling. Further, the presence of high vacancy concentrations is expected to improve the reaction kinetics in light-metal hydrides. NaAlH₄, catalyzed with titanium (Ti) metal and Ti based compounds such as TiCl₃ and Ti(OBu)₄, is known to show a relatively large reversible hydrogen capacity, practically: 4.5 wt.%, at a moderately low operating temperature (150 °C) [14, 22, 23, 68–71]. NaAlH₄ releases hydrogen in two steps (see Equation (4.1)) upon heating, involving an intermediate phase Na₃AlH₆ (sodium aluminum hexahydride) in the first step, and NaH (sodium hydride) in the second step, with the formation of Al (aluminum) in both steps:



The significance of the role of these catalysts is well known, but the mechanism by which these catalysts enhance the cycling kinetics of hydrogen and reversibility of reaction has been, and still is, an intriguing

question [72,73]. A number of different theories about the possible local environment and the role of Ti have been suggested [74,75]. It is indicated that Ti dwells on the surface of the material enabling dissociation of hydrogen molecules, and substitutes for Na possibly facilitating the decomposition reactions. It may attract a large number of H atoms [76–78] or induces an increased hydrogen vacancy formation [79–81]. However, previous studies established firmly that Ti is in an environment of Al atoms [74,75]. Possible mechanisms to be considered should, therefore, be consistent with this finding.

In order to reveal information on the mechanism on a microscopic level, an in situ neutron diffraction approach was used. An essential aspect is that the reversibility of reactions requires a migration of hydrogen and metal species over distances typically of the order of the sizes of the crystallites. Small crystallite sizes, therefore, may clearly facilitate the mass transport of hydrogen (H), Al, and sodium (Na) atoms, yielding Na_3AlH_6 and NaAlH_4 in the absorption reactions. Thus, it is important to study the evolution of grain sizes for the catalyzed and the uncatalyzed NaAlH_4 . Protonated catalyzed NaAlH_4 were compared with uncatalyzed NaAlH_4 using in situ neutron diffraction, and the phase transformations during hydrogen release and deuterium reloading were studied.

Based on the experimental results, an interesting large reduction of particle sizes was observed in the catalyzed material. A probable mechanism by which the TiCl_3 enhances the reversibility and cycling kinetics is suggested in this chapter. In this mechanism, the importance of grain refinement, the phenomenon of maintaining crystallite sizes small down to nanometer during the cycling process, is discussed. Further, the detected hydrogen site occupation provides new insights into the hydrogen migration through the mixed phase structures. In particular, quantitative information on hydrogen-vacancy formation and hydrogen-deuterium exchange was deduced from the Rietveld analysis of the neutron scattering data. Pronounced hydrogen vacancy formation was observed which can play a crucial role in the hydrogen diffusion and possibly also the Al and Na diffusion through the particles during hydrogen release and D_2 uptake. The in situ neutron diffraction study on TiCl_3 -

catalyzed NaAlH_4 [82] revealed that crystallite sizes of Na_3AlH_6 (approximately 200 nm), NaH and Al (approximately 120 nm) remain small during hydrogen cycling, in striking contrast to the large sizes ($\geq 1 \mu\text{m}$) observed for uncatalyzed NaAlH_4 . The maintenance of small crystallite sizes is caused by grain refinement, i.e., arresting grain sizes, induced by the formed TiAl_x and NaCl (sodium chloride) compounds, acting as nucleation centers for Al and NaH, respectively. Interestingly, TiAl_3 and Al share the same Al lattice planes in their crystallographic structure with only a small lattice mismatch, a prerequisite for effective grain refinement. A similar structure match occurs for NaCl and NaH. Moreover, the neutron study revealed significant hydrogen vacancy formation in both Na_3AlH_6 and NaH upon decomposition of TiCl_3 -catalyzed NaAlH_4 . A clear, unexpected and interesting H-D exchange in NaH_{1-x} was observed upon reloading of Na_3AlH_6 with deuterium. This chapter emphasizes the importance of grain refining for achieving reversibility and faster kinetics of the hydrogen sorption processes, with a crucial additional role played by the catalyst besides being a splitter for hydrogen molecules.

4.1 Experimental details

A catalyzed sample was prepared by ball milling protonated NaAlH_4 and 2 mol% TiCl_3 powders with a purity of 99.9999% in a Spex 8000 apparatus for 15 min. Both, NaAlH_4 and TiCl_3 , were obtained from Sigma Aldrich. A high energy milling was used, which ensures that 15 min was sufficient for a good distribution of the catalyst with a minimum amount of NaAlH_4 decomposition. The alanate was ball milled with a ball to powder mass ratio of 10:1. As a reference, an uncatalyzed NaAlH_4 powder was prepared in the same manner without addition of TiCl_3 . Both samples were loaded into quartz tubes under an argon atmosphere, which were subsequently connected to a gas-handling system for use in the in situ neutron diffraction measurements at GEM diffractometer, ISIS, Oxfordshire, UK.

In the neutron studies, the catalyzed and uncatalyzed NaAlH_4 were heated until the hydrogen release started. A constant flow of hydrogen gas at a pressure of 1–2 bar was maintained during hydrogen desorp-

tion at 100 °C in the catalyzed NaAlH₄ in order to work under realistic pressure conditions relevant for future applications. In the uncatalyzed NaAlH₄, a similar approach was taken, but the sample needed higher temperatures for the first decomposition step to start, accompanying the observed melting of NaAlH₄ phase, in contrast to the catalyzed NaAlH₄. Additionally, a sudden increase in the hydrogen release rate occurred after the onset of the first decomposition step, which did not allow the maintenance of a controlled hydrogen flow.

Deuterium gas was used to study the reloading behavior in the catalyzed and uncatalyzed NaAlH₄. For the catalyzed NaAlH₄, a deuterium pressure of 10 bar was applied after the first decomposition at 100 °C to monitor the D₂ uptake by Na₃AlH_{6-x} by exchanging H₂ and D₂, or by filling hydrogen vacancies in the structure. After the completion of the second decomposition step, involving the formation of NaH and Al from Na₃AlH₆, a 10 bar D₂ was applied at 150 °C for reloading. Na₃Al(H,D)₆ was formed from NaH with Al upon the addition of D₂ at 150 °C. Subsequently, Na(H,D) and Al were formed upon the decomposition of Na₃Al(H,D)₆ at 150 °C.

A neutron diffraction pattern was acquired at every 10 min during the procedures described above [38], amounting to a total of 89 spectra for the catalyzed and 30 spectra for the uncatalyzed NaAlH₄. All diffraction spectra were fitted by Rietveld refinement analysis using the GSAS and the Sequentz programs [35, 83]. The patterns collected in the different detector banks were fitted simultaneously, and the phase fractions, lattice parameters, hydrogen site occupancies, and line widths were allowed to vary freely. The grain sizes were calculated directly from the broadening of the fitted profile using an equation based on Scherrer's formula. In this way, the extracted grain sizes from the diffraction line broadening for the catalyzed and uncatalyzed NaAlH₄ crystallites after the ball milling found to be the same, i.e., approximately 110 nm.

Additionally, as a reference, protonated NaAlH₄ was ball milled with 2 mol% Ti metal powder in a Spex 8000 apparatus for 120 min. This longer milling time was needed because the Ti-metal is less brittle than TiCl₃. After the ball milling, grain sizes of NaAlH₄ were approximately

50 nm extracted from the diffraction line broadening. Ex situ X-ray diffraction was performed on the Ti-catalyzed sample using a Bruker-AXS Type D5005 diffractometer at the Cu K_{α} wavelength.

4.2 Results

In situ neutron diffraction measurements were carried out on uncatalyzed and TiCl_3 -catalyzed NaAlH_4 , and the diffraction patterns were obtained during hydrogen cycling. The evolution of different phases over time in the diffraction patterns is shown in the colored plots, i.e., Figure 4.1 and Figure 4.2, for the respective samples, after subtraction of the fitted incoherent background due to protons.

4.2.1 Uncatalyzed NaAlH_4

In the reference uncatalyzed NaAlH_4 , four different phases, as expected, namely NaAlH_4 , Al, Na_3AlH_6 , and NaH, were observed during the desorption process. The evolution of the phase fractions of these four phases over time, as extracted from the Rietveld analysis, is presented in Figure 4.3. The neutron diffraction pattern on the ball milled uncatalyzed NaAlH_4 powder at room temperature showed a partial decomposition of NaAlH_4 , revealed by the presence of a small amount of both Al (approximately 8%) and Na_3AlH_6 (approximately 3%). Upon heating this sample, a small increase in the released hydrogen pressure to approximately 350 mbar was observed at 150 °C, indicating the onset of the first decomposition step. The phase fractions of Al and Na_3AlH_6 phases significantly increased upon further heating to 190 °C accompanied by the release of hydrogen gas. At 190 °C, all the Bragg peaks associated with the NaAlH_4 phase disappeared abruptly due to the melting of NaAlH_4 . However, the Bragg peaks related to the Na_3AlH_6 and Al phases were still present. Incoherent scattering of neutrons due to hydrogen (protons) contributes significantly to the background in the diffraction patterns. The observed decrease in the background levels during hydrogen desorption, therefore, provided a further measure for the release of hydrogen. The second

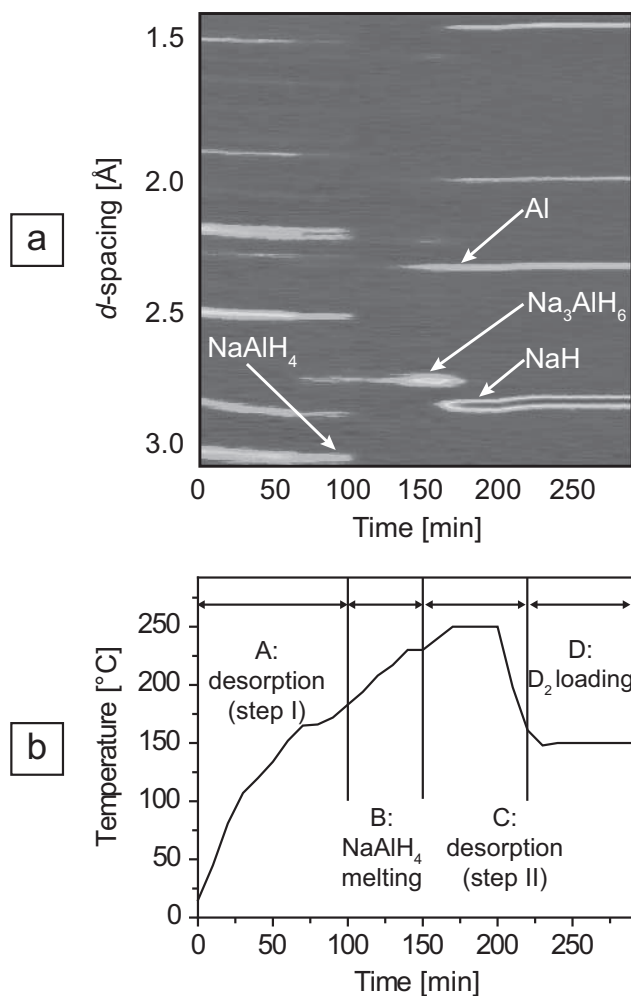


FIGURE 4.1 – (a) Neutron diffraction spectra during hydrogen desorption for uncatalyzed NaAlH₄. The incoherent background due to hydrogen was subtracted. The horizontal axis represents a small section of the d-spacing range measured. Bragg reflections of four different phases (NaAlH₄, Al, Na₃AlH₆, and NaH) were detected in uncatalyzed NaAlH₄; (b) corresponding change in temperature is plotted over time describing the hydrogen release and deuterium loading steps.

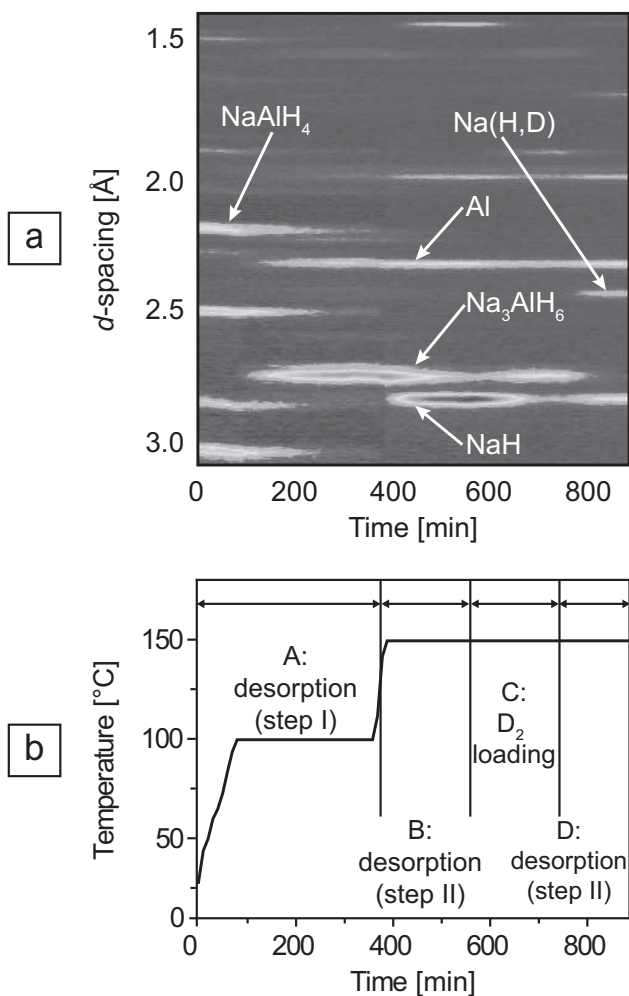


FIGURE 4.2 – (a) Neutron diffraction patterns plotted over time, showing the growth and decay of the different occurring phases, NaAlH_4 , Al , Na_3AlH_6 , NaCl , and Na(H,D) , during dehydrogenating and rehydrogenating of TiCl_3 -catalyzed NaAlH_4 . The incoherent background was subtracted. The horizontal axis represents a small section of the total d-spacing range measured; (b) corresponding change in temperature is plotted over time describing the hydrogen release and deuterium loading steps.

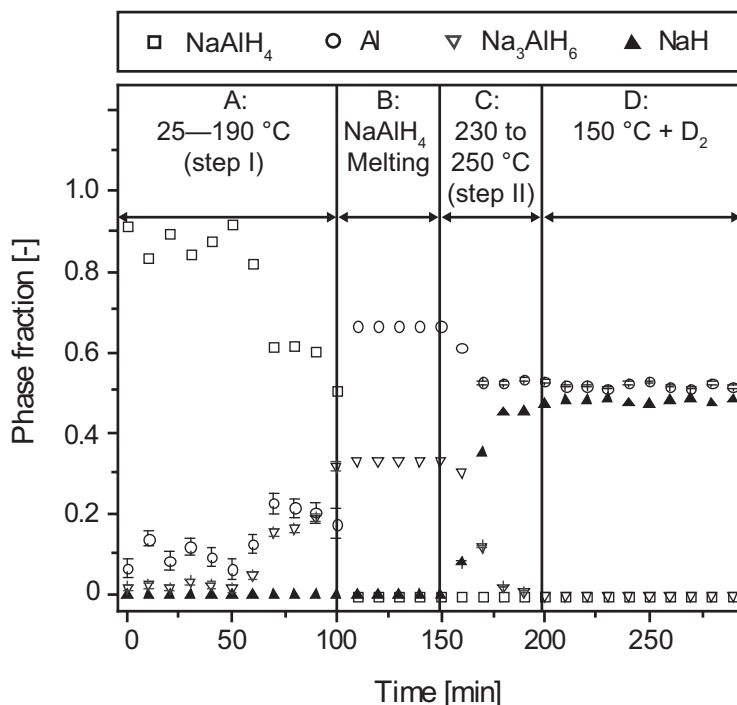


FIGURE 4.3 – Evolution of the phase fractions of NaAlH_4 , Na_3AlH_6 , NaH , and Al during hydrogen release in the uncatalyzed NaAlH_4 . The plot is divided into four intervals A–D; A: hydrogen desorption from room temperature to 190 °C; B: Melting of NaAlH_4 at 190 °C and the formation of Al and Na_3AlH_6 (with imposed fixed ratio of 2:1); C: second decomposition step in the temperature range of 230–250 °C; and D: trial of D_2 loading using a 10 bar pressure at 150 °C and subsequent desorption.

decomposition step, involving formation of NaH and Al phases at the expense of Na_3AlH_6 , commenced at 230 °C and completed at 250 °C. Following the completion of the second decomposition step, an attempt was made to reload the uncatalyzed NaAlH_4 with a 10 bar deuterium pressure at 150 °C, which was unsuccessful. No peaks related to $\text{Na}_3\text{Al}(\text{H},\text{D})_6$ formation could be discerned in the diffraction patterns, confirming the known irreversible behavior of the uncatalyzed NaAlH_4 .

4.2.2 Catalyzed NaAlH₄

Figure 4.4 shows the evolution of five different phases, extracted from the neutron diffraction spectra by Rietveld analysis, over time in the catalyzed NaAlH₄.¹ Further, a complete reversibility of the second step was observed in this case upon hydrogen cycling at 150 °C. No peaks related to Ti, its hydride or alloys such as Ti_xAl_{1-x}, TiAl₃ or TiCl₃ were observed. The first decomposition step started at 100 °C, and the flow of the released hydrogen was maintained to 1–2 bar pressure. The TiCl₃-catalyzed NaAlH₄ transformed completely into Na₃AlH₆ and Al in 270 min, with no signs of NaCl formation yet. The decomposition of Na₃AlH₆ into NaH and Al started at 150 °C, and completed in 150 min with the further release of hydrogen. Bragg peaks of NaCl were observed at this step. The decomposition products NaH and Al completely transformed back into Na₃Al(H,D)₆ upon application of 10 bar of deuterium pressure at 150 °C. Subsequent desorption of Na₃Al(H,D)₆ resulted in the formation of Na(H,D) and additional Al.

Clearly, the uncatalyzed and TiCl₃ catalyzed NaAlH₄ behave differently with respect to their reversibility. Reversibility involves mass transport of metal ions and hydrogen. Small crystallites, therefore, will clearly facilitate the mass transfer. Considering this fact, the evolution of grain sizes was monitored and compared for both kinds of sample. The grain sizes were calculated from the peak broadening using detailed Rietveld refinement analysis. The dependence of the width of diffraction peaks on *d*-spacing is consistent with grain size-induced broadening and rules out significant strain broadening. After ball milling, the grain sizes obtained in this manner for catalyzed and uncatalyzed NaAlH₄ were approximately 110 nm. In uncatalyzed NaAlH₄, the NaH and Al peaks were not broadened, indicating the presence of large grains. The estimated grain size is $\geq 1 \mu\text{m}$, corresponding to the resolution limit of the backscattering bank of GEM for diffraction line broadening. For catalyzed NaAlH₄, on the contrary, the grain sizes of NaH and Al were only approximately 120 nm, i.e., small and remarkably similar, with modest changes in the size during the various reactions (see Figure 4.5).

¹See the fitted patterns in Appendix A.

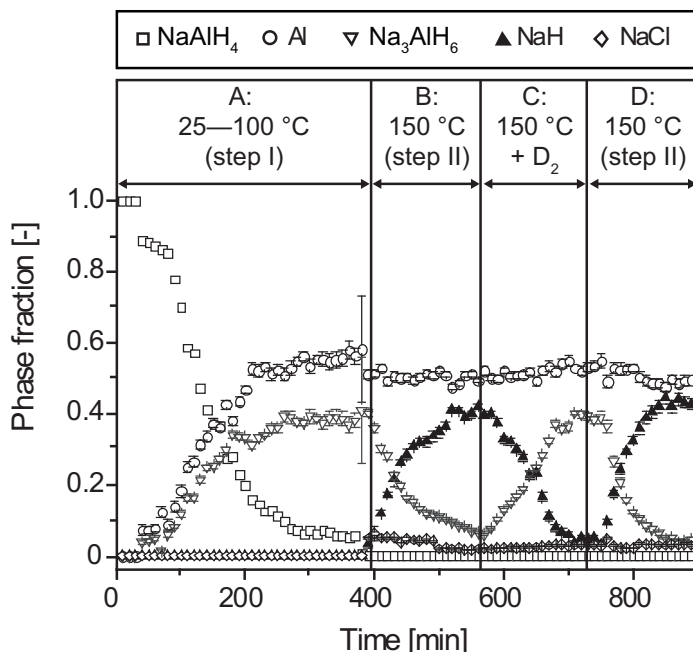


FIGURE 4.4 – Growth and decay of NaAlH_4 , Na_3AlH_6 , NaH , Al , and NaCl in terms of extracted phase fractions over time for the TiCl_3 -catalyzed NaAlH_4 during cycling. The four intervals, A–D, in the plot signify; A: First desorption step at $100\text{ }^\circ\text{C}$; B: Second decomposition step at $150\text{ }^\circ\text{C}$; C: 10 bar D_2 loading at $150\text{ }^\circ\text{C}$; D: Subsequent desorption after D_2 loading at $150\text{ }^\circ\text{C}$.

The grain sizes of NaCl and $\text{Na}_3\text{Al}(\text{H,D})_6$ were approximately 40 nm and 200 nm, respectively. Hydrogen vacancies facilitate the diffusion of hydrogen and metal species, making their presence an important parameter to study. Therefore, the hydrogen occupancy was monitored by detailed Rietveld analysis of the neutron diffraction patterns. The extracted hydrogen site occupancy effectively represents the coherent cross-section at the hydrogen site, and therefore, can vary either due to hydrogen vacancy formation or due to exchange of hydrogen with deuterium after D_2 exposure (see Figure 4.6), as the coherent neutron scattering lengths of hydrogen and deuterium are different and are of opposite sign

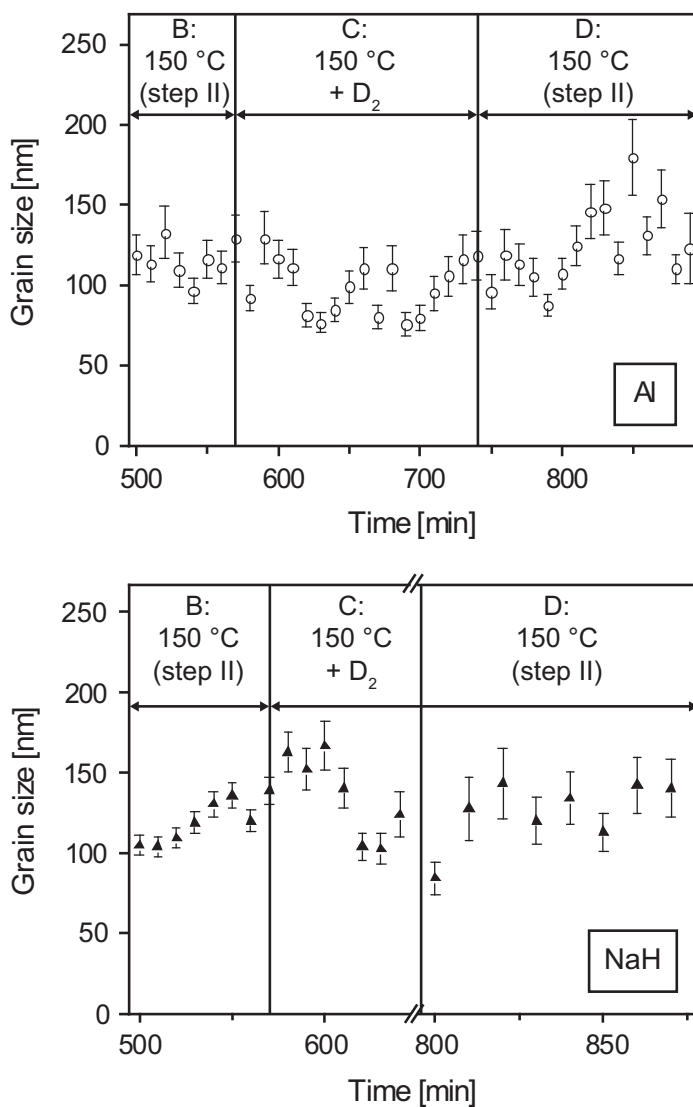


FIGURE 4.5 – Evolution of grain sizes of Al and NaH over time for the TiCl_3 -catalyzed NaAlH_4 , showing a striking similarity in the sizes and a slight variation in the average size of approximately 120 nm.

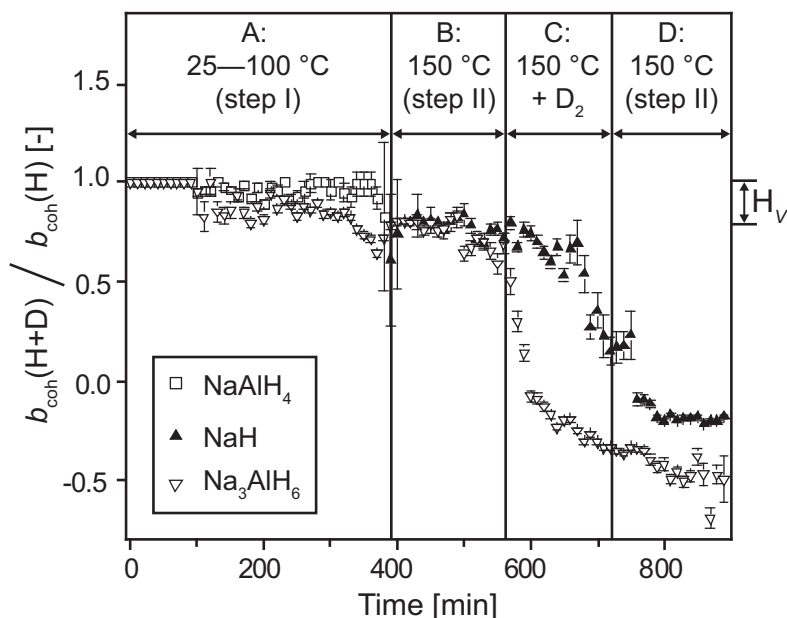


FIGURE 4.6 – Variation of the effective coherent scattering length b_{coh} at the hydrogen sites normalized to $b_{\text{coh}}(\text{H})$ for NaAlH_4 , Na_3AlH_6 , and NaH , respectively, over time for the TiCl_3 -catalyzed NaAlH_4 . In the interval of A and B, $b_{\text{coh}}(\text{H}+\text{D})/b_{\text{coh}}(\text{H})$ decreases due to hydrogen vacancy formation, while in the region C and D, the large reduction in the relative b_{coh} is due to a combined effect of hydrogen vacancy and hydrogen-deuterium exchange. The time intervals A—D represent; A: first desorption at 100 °C; B: second desorption at 150 °C; C: loading deuterium with 1 bar pressure at 150 °C; D: subsequent pumping out of deuterium at 150 °C.

($b_{\text{coh}}(\text{H}) = -3.74$ fm and $b_{\text{coh}}(\text{D}) = 6.67$ fm). The hydrogen sites remained fully occupied in uncatalyzed NaAlH_4 , maintaining the stoichiometry for NaAlH_4 , Na_3AlH_6 , and NaH over time. On the other hand, Na_3AlH_6 and NaH showed a considerable lowering in the hydrogen site occupancy in the catalyzed NaAlH_4 sample. Figure 4.6 represents the results in terms of the observed effective scattering length b_{coh} normalized to scattering length of hydrogen $b_{\text{coh}}(\text{H}) = -3.74$ fm for a fully occupied H site.

4.3 Discussion

4.3.1 Effect of grain sizes on reversibility

The neutron diffraction results clearly showed that the desorption and the rehydrogenation behavior of catalyzed and uncatalyzed NaAlH_4 is, as expected, remarkably different. The hydrogen was released smoothly in TiCl_3 -catalyzed NaAlH_4 for both reaction steps at a reaction time scale of the order of 150 min. On the other hand, the first reaction step in the uncatalyzed NaAlH_4 showed abrupt hydrogen release and involved melting of the NaAlH_4 phase before complete transformation was reached. Further, the second reaction step was completely reversible upon D_2 loading for catalyzed NaAlH_4 under 10 bar at 150 °C. On the contrary, the uncatalyzed NaAlH_4 could not be reloaded under the same temperature and pressure conditions.

While the above phenomena have been observed in earlier studies, a remarkable correlation between the grain sizes and the rehydrogenation reactions is observed here, which was not reported before in studies related to NaAlH_4 . The decomposition products of the uncatalyzed NaAlH_4 , such as Na_3AlH_6 , Al, and NaH, showed a clear growth in the grain sizes to values, $\geq 1 \mu\text{m}$, upon heating. In fact, the NaAlH_4 phase also showed a clear growth in the grain size from approximately 110 nm to 280 nm upon raising the temperature to 160 °C—annealing—before the onset of the first decomposition step.

On the other hand, the TiCl_3 -catalyzed NaAlH_4 showed maintained nano-size grains during the hydrogen cycling. The catalyzed NaAlH_4 showed a successful loading by D_2 in the second reaction step, and NaH and Al showed grain sizes of approximately 120 nm. This clearly indicates that the grain size is an important factor in the rehydrogenation step. This can be easily understood since reversible hydrogen charging in these materials requires the transport of H, Al, and Na ions, as well as mixing at the atomic level after phase separation has occurred. Clearly, a small size of crystallites reduces the diffusion distance, and so enhances the kinetics of reloading [84–86]. Noticeably, a partial reversibility of the hydrogen sorption was attained [87] for NaAlH_4 particles of only a

few nanometers on a surface-oxidized carbon nanofiber support. Here no transition metal catalyst was added, while the support is described as having no chemical reactions with the alanate during sorption or catalytic activity itself. When correct, this further indicates the large relevance of the diffusion distance. Apart from the diffusion distance aspect, small crystallites also appear to exhibit significant hydrogen vacancy concentrations, as described in the following section.

4.3.2 Hydrogen vacancy formation

The role of hydrogen vacancies for hydrogen migration has been widely studied in interstitial metal hydrides. The hydrogen sorption kinetics in crystalline solids is largely influenced by the presence of vacancies, and is further enhanced by the presence of grain boundaries. Nanoscopic metal hydride crystallites may contain large amount of vacancies [20], this may facilitate the hydrogen sorption kinetics. While recent theoretically studies on the role and presence of vacancies in NaAlH₄ and its decomposition products have focused on metal vacancies [88, 89], here the occurrence of a significant hydrogen vacancy formation is shown experimentally for TiCl₃-catalyzed NaAlH₄. Figure. 4.6 shows the development of the effective coherent scattering lengths $b_{\text{coh}}(H + D)/b_{\text{coh}}(H)$ for NaAlH₄, Na₃AlH₆, and NaH over time for the catalyzed NaAlH₄.

A hydrogen vacancy concentration of roughly 20% was observed for Na₃AlH₆ from the beginning to the end of time interval “A” and “B” in Figure 4.6, determined from the decrease in effective scattering length. This reduction is deduced from Rietveld refinement fitting, but is also directly observable from the relative change in the Bragg peak intensities for Na₃AlH_{6-x} compared to stoichiometric Na₃AlH₆ (see Figure 4.7). A decrease of 20% in the effective coherent scattering lengths $b_{\text{coh}}(H + D)/b_{\text{coh}}(H)$ was observed for NaH_{1-x}, which is due to a combination of the effects of hydrogen vacancies and the presence of deuterium in NaH. For NaH, the effect of deuterium on the effective scattering of NaH can not be excluded, as a 10 bar of deuterium pressure was applied after the completion of the first decomposition step. A calculation of this effect of deuterium on the effective scattering for NaH shows that a minimum of

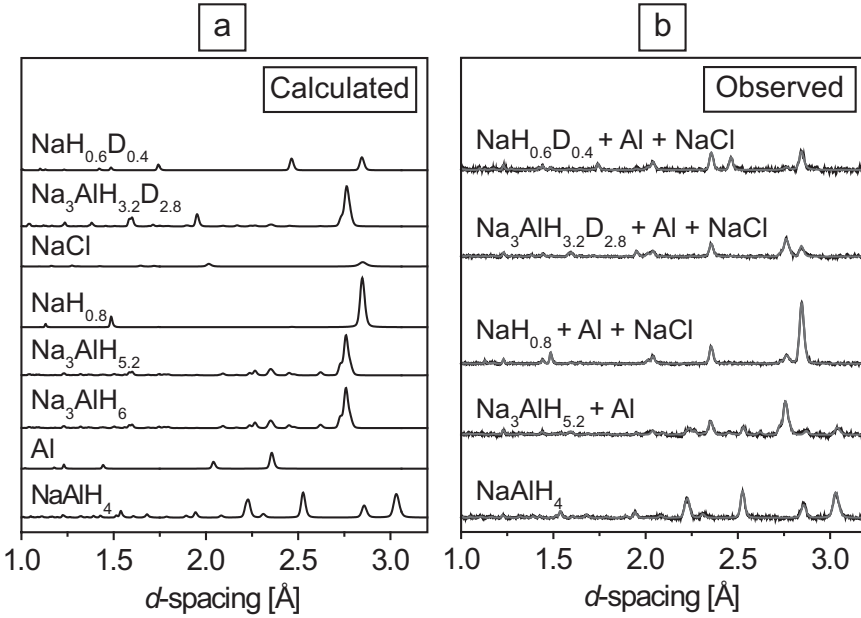


FIGURE 4.7 – (a) For clarity, simulated patterns extracted from Rietveld refinement are shown for all occurring phases separately (bottom to top: NaAlH_4 , Al , Na_3AlH_6 , $\text{Na}_3\text{AlH}_{5.2}$, $\text{NaH}_{0.8}$, NaCl , $\text{Na}_3\text{AlH}_{3.2}\text{D}_{2.8}$, $\text{NaH}_{0.6}\text{D}_{0.4}$) for catalyzed NaAlH_4 , illustrating the effects of hydrogen vacancy formation in $\text{Na}_3\text{AlH}_{6-x}$ and H-D exchange in NaH_{1-x} on the Bragg peak intensities. The simulated spectra for $\text{Na}_3\text{AlH}_{5.2}$ and $\text{Na}_3\text{AlH}_{3.2}\text{D}_{2.8}$ were normalized against the strongest peak of Na_3AlH_6 at a d-spacing of 2.755 Å; (b) The fitted observed neutron diffraction patterns for the respective phases are shown for reference. The spectra are plotted after subtraction of the incoherent background due to hydrogen.

3–5% concentration of hydrogen vacancies is still present in NaH . Here, the changes in the Bragg peak intensities were not easily deduced by the eye from the neutron diffraction patterns. The intensities of the even index NaH_{1-x} Bragg peaks rise according to

$$I \propto |F_{hkl}|^2 \propto (b_{\text{coh}}(\text{Na}) + (1-x)b_{\text{coh}}(\text{H}))^2 = (3.74x - 0.11)^2 \quad (4.2)$$

or $I \propto (x - 0.03)^2$ for hkl even with hydrogen vacancy fraction x . Nevertheless, a combination of Rietveld refinement and a clearly observed H-D

exchange at such a low temperature of 150 °C in NaH, provide a proof for the presence of large amount of hydrogen vacancy formation in NaH for catalyzed TiCl_3 - NaAlH_4 .

The observed abundant unoccupied hydrogen sites may well facilitate hydrogen diffusion through the sample, as was reported by Schimmel et al. in the case of nanostructured and catalyzed MgH_{2-x} [20]. The presence of vacancies facilitates the hydrogen diffusion by decreasing the migration energy for hydrogen. On the contrary, no change in the hydrogen site occupancies from the stoichiometric value, was observed for NaAlH_4 , Na_3AlH_6 , and NaH for uncatalyzed NaAlH_4 . Previous studies proposed that the prevention of phase separation and its related strains and interfacial energy in nanoscale crystals leads to vacancy formation in nano-crystalline (approximately 120 nm) MgH_{2-x} [20]. Similarly, strong structural changes were observed as a result of the prevention of intranocrystallite phase separation for small particle size in Li-insertion compounds with sizes in the range 7–120 nm [28]. Such phase separation related effects may also occur here for the nano-crystalline reaction products, Na_3AlH_6 and NaH, promoting hydrogen vacancy formation. The large amount of vacancy formation in Na_3AlH_6 may be due to a low formation energy for a vacancy, either related to size effects, or to the presence of Ti, as suggested in recent ab-initio studies on Na_3AlH_6 and NaAlH_4 [80] showing that low hydrogen vacancy formation energies indeed can be reached. Palumbo et al. [79] recently showed the presence of local relaxation dynamics in the decomposition of NaAlH_4 using anelastic spectroscopy, indicating hydrogen vacancy formation in Na_3AlH_6 . A mechanism for the vacancy formation was described based on the weakening of the local H–Al bonds, which was linked to the presence of Ti. A model to explain the increased hydrogen transport was also proposed [79].

The situation in NaAlH_4 for hydrogen sorption is more complicated than that for nano-crystalline MgH_{2-x} because of the involvement of a large number of phases. Nevertheless, it is proposed that the large vacancy densities in the catalyzed NaAlH_4 appear to be induced by the nanoscale of the Na_3AlH_6 crystallites, while the Ti-catalyst may play a

key role in the initial vacancy formation in Na_3AlH_6 , as suggested by ab initio calculations and by anelastic spectroscopy studies. Ti, however, is not expected to play such a role for the NaH crystallites, since earlier TEM studies [90] demonstrated that for the NaH–Al state the Ti is entirely located in the Ti_xAl crystallites. For NaH, a model to explain was evaluated the large amount of vacancies (see Chapter 5).

4.3.3 Grain refinement by the $\text{Ti}_x\text{Al}_{1-x}$ and NaCl particles

As already mentioned in the beginning of this chapter, crystallites of nano-size are important for reversibility and possibly also for hydrogen vacancy formation. Starting with nano-size crystals can be done easily such as by grinding the powder in a ball mill. However, maintaining the crystallite size small during the loading and unloading process is challenging and very important, as the crystallite otherwise generally grow in size during hydrogen cycling.

Studies on solidification of liquid aluminum [26,27] have shown that TiAl_3 acts as a grain refiner—prevention of agglomeration—for Al crystallites. Small TiAl_3 crystallites enhance the nucleation of solid aluminum. When a sufficient amount of nucleation centers (see Figure 4.8) is present in a well dispersed configuration, they do not allow the Al grains to grow beyond a certain size [26,27]. On the other hand, the absence of sufficient nucleation centers may lead to superheating [91] before a structural phase transition take place, yielding relatively large Al crystallites. The neutron experiment also showed that the uncatalyzed NaAlH_4 could be heated even above its standard melting temperature of 180 °C, before the major decomposition and melting occurs, resulting in large Al and Na_3AlH_6 crystallites.

Previous synchrotron X-ray diffraction and XAFS (X-ray absorption fine structure) studies on 6–10 mol% TiCl_3 catalyzed NaAlH_4 clearly showed the presence of $\text{Ti}_x\text{Al}_{1-x}$, Ti dissolved in Al, alloys after cycling [74,92,93]. A TEM study on NaAlH_4 catalyzed with 4 mol% TiCl_3 revealed TiAl_3 formation with hydrogen desorption [90]. Therefore, it is expected that $\text{Ti}_x\text{Al}_{1-x}$ formation also occurred in the present experiment. However, such $\text{Ti}_x\text{Al}_{1-x}$ phase was not detected in the diffraction

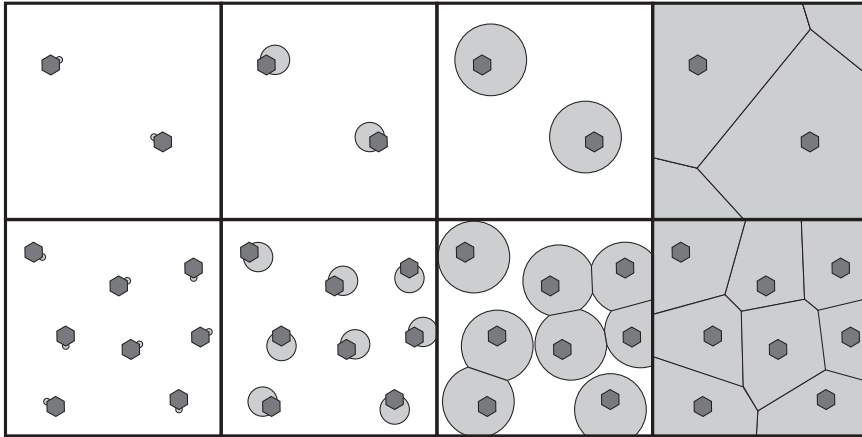


FIGURE 4.8 – A schematic picture showing that the high density of nucleation centers ($\text{NaCl} / \text{Ti}_x\text{Al}_{1-x}$) leads to finer grains.

patterns, possibly, because of the small amount of the catalyst and the overlap of the $\text{Ti}_x\text{Al}_{1-x}$ Bragg peaks with the Al metal Bragg peaks.

One of the important conditions for the grain refining action to happen is to have a good lattice matching between the substrate, nucleation center, and the adherent material. In view of the known grain refining action of TiAl_3 for Al, the presence of $\text{Ti}_x\text{Al}_{1-x}$, which has a distorted Al crystal structure, is responsible for arresting the crystallite sizes of Al to a certain size and preventing the agglomeration of Al crystallites. Interestingly, NaH and NaCl share the same rock salt crystal structure with a reasonably small lattice mismatch of close to 15%, see Table 4.1. Table 4.2 shows the structural parameters, extracted from the Rietveld refinement, for the other occurring phases during sorption reactions of TiCl_3 -catalyzed ball milled NaAlH_4

This may facilitate NaCl to act as a grain refiner for NaH and vice versa. NaCl grew simultaneously with NaH during the second decomposition step. After the complete formation of NaCl, approximately 40 nm in grain size, NaCl may act as grain refiner for Na(H,D) and stabilize the size of NaH crystallite in the last decomposition. Based on crystallite sizes and phase concentrations, approximately 1–2 NaCl crystallites per

TABLE 4.1 – Obtained structural parameters of the NaH and NaCl containing phases observed during sorption reactions of TiCl₃-catalyzed ball milled NaAlH₄.

NaH [<i>Fm</i> $\bar{3}$ <i>m</i>]	
Lattice parameter at 150 °C	$\mathbf{a}_1, \mathbf{a}_2, \mathbf{a}_3 = 4.91 \text{ \AA}$
Atom site in Wyckoff notation	Na: 4a (0, 0, 0) H: 4b (0.5, 0.5, 0.5)
Occupancy	Na: 1.000 H: 1.000 down to 0.72
NaCl [<i>Fm</i> $\bar{3}$ <i>m</i>]	
Lattice parameter at 150 °C	$\mathbf{a}_1, \mathbf{a}_2, \mathbf{a}_3 = 5.673 \text{ \AA}$
Atom site in Wyckoff notation	Na: 4a (0, 0, 0) Cl: 4b (0.5, 0.5, 0.5)
Occupancy	Na: 1.000 Cl: 1.000

NaH crystallite were estimated to form, which seems adequate for the activity as nucleation centers and to prevent NaH crystallite agglomeration beyond approximately 120 nm. Further, the observed sizes of the resulting Na₃AlH₆ crystallites—average approximately 200 nm, matches well with the combined volume of 3 NaH and 1 Al crystallite with a diameter of approximately 120 nm each.

4.3.4 Comparison with Ti-metal catalyzed NaAlH₄

Haiduc et. al showed that doping of NaAlH₄ with either TiCl₃ or Ti(OBu)₄ results in different Ti-compounds upon hydrogen desorption [94]. This was a motivation to study also the evolution of grain sizes of 2 mol% Ti-metal catalyzed NaAlH₄ by ex situ XRD after hydrogen desorption, enabling a comparison with TiCl₃-catalyzed NaAlH₄. The results show that the grain refining action may well depend on the amount, type, and

TABLE 4.2 – The structural parameters for NaAlH₄, Na₃AlH₆, and Al extracted from the Rietveld refinement during sorption reactions of TiCl₃-catalyzed ball milled NaAlH₄.

	NaAlH ₄ [<i>I41/a</i>]
Lattice parameter at 100 °C	$\mathbf{a}_1, \mathbf{a}_2 = 5.044 \text{ \AA}, \mathbf{a}_3 = 11.434 \text{ \AA}$
Atom site in Wyckoff notation	Na: 4a (0, 0.2500, 0.1250) Al: 4b (0, 0.2500, 0.6250) H: 16f (0.2340, 0.3860, 0.5500)
Occupancy	Na: 1.000 Al: 1.000 H: 1.000
	Na ₃ AlH ₆ [<i>P21/n</i>]
Lattice parameter at 100 °C	$\mathbf{a}_1 = 5.449 \text{ \AA}, \mathbf{a}_2 = 5.536 \text{ \AA}, \mathbf{a}_3 = 7.802 \text{ \AA}$
Atom site in Wyckoff notation	Na1: 2a (0, 0, 0.5) Na2: 2b (-0.006, 0.4601, 0.2518) Al: 4e (0, 0, 0) H1: 4e (0.091, 0.041, 0.215) H2: 4e (0.234, 0.328, 0.544) H3: 4e (0.165, 0.266, 0.944)
Occupancy	Na1: 1.000 Na2: 1.000 Al: 1.000 H1, H2, H3: 1.000 down to 0.82
	Al [<i>Fm$\bar{3}$m</i>]
Lattice parameter at 100 °C	$\mathbf{a}_1, \mathbf{a}_2, \mathbf{a}_3 = 4.064 \text{ \AA}$
Atom site in Wyckoff notation	Al: 4a (0, 0, 0)
Occupancy	Al: 1.000

TABLE 4.3 – Comparison of the grain sizes of the NaAlH₄, NaH, and Al phases during sorption reactions in TiCl₃-catalyzed and Ti-catalyzed NaAlH₄.

Sample	Sample treatment	Grain size [nm]		
		NaAlH ₄	NaH	Al
TiCl ₃ -catalyzed NaAlH ₄	Ball milled	110		
	150 °C		120	120
	150 °C + D ₂ , 150 ^a			
Ti-catalyzed NaAlH ₄	Ball milled	50		
	0.5 h at 150 °C		100	220
	2 h at 170 °C		120	220
	8 h at 180 °C		100	190

^aSee Figure 4.5

structure of the Ti alloys formed. In contrast to TiCl₃-catalyzed NaAlH₄, the Al and NaH crystallites for Ti-catalyzed NaAlH₄ showed a growth of a factor of 4 and 2, respectively, compared with the initial grain size of NaAlH₄ after the ball milling (Table 4.3).

The observed growth may be due to the dispersion of Ti in the Ti_xAl_{1-x} may be different relative to TiCl₃-catalyzed NaAlH₄, where the TiCl₃ catalyst may be dispersed more homogeneously, resulting in smaller Al crystallites. Further, growth in NaH crystallite size to a factor of 2 compared with the initial grain size of NaAlH₄ in the absence of NaCl confirms the grain refining action of NaCl. Interestingly, the NaH crystallites do not show any further growth at higher temperature over prolonged time (Table 4.3). This may indicate that the presence of nanoscale Al crystallites, stabilized by Ti_xAl_{1-x} alloys, imposes a morphology in which NaH crystallites cannot grow upon annealing.

4.3.5 Hydrogen-deuterium exchange in NaH

The evolution of the effective scattering lengths $b_{\text{coh}}(H + D)/b_{\text{coh}}(H)$ of the Na₃AlH₆ and NaH phases (Figure 4.6) show a further significant reduction during D₂ loading of NaH together with Al in the time interval “C”. Interestingly, this large reduction in $b_{\text{coh}}(H + D)/b_{\text{coh}}(H)$ is primarily related to hydrogen-deuterium (H-D) exchange [95] upon D₂ loading. This reduction is not due to an increase in amount of H vacancies in nano-NaH. The negative values of observed $b_{\text{coh}}(H + D)/b_{\text{coh}}(H)$ are caused by the opposite sign of scattering length of D₂ with respect to $b_{\text{coh}}(H)$. Additionally, the H-D exchange in NaH is clearly visible by the appearance of additional, even indexed, Bragg peaks in the neutron diffraction patterns of Na(H,D), as shown in Figure 4.7. The incorporated deuterium fraction x in NaH_{1-x}D_x can be sensitively monitored by the rise of the even-indexed peaks upon H-D exchange (see Equation (4.3)) in the neutron diffraction peaks

$$I \propto (b_{\text{coh}}(\text{Na}) + (1 - x)b_{\text{coh}}(\text{H}) + xb_{\text{coh}}(\text{D}))^2 = (10.41x - 0.11)^2 \quad (4.3)$$

or $I \propto (x - 0.01)^2$ for even hkl . The NaH diffraction exhibits only odd-indexed peaks. The presence of odd-indexed peaks only in NaH is caused by accidental extinction of the even-indexed peaks because the coherent neutron scattering lengths of Na (+3.62 fm) and H (-3.74 fm) are almost equal, but are opposite in sign. The formation of Na₃Al(H, D)₆ in the region “C” is expected; however, the exchange of deuterium with hydrogen in nano-NaH lattice is surprising. NaH is known to be a rather stable compound, with a very low hydrogen equilibrium pressure of about 0.01 mbar at 150 °C [96]. This infers that, despite the stability of NaH, H-D exchange happens fairly rapidly for such NaH nano-particle. Clearly, the presence of abundant H-vacancies in nano-NaH, as detected here, are essential for H-D exchange to happen on the observed timescale of approximately 100 min at a relatively low temperature. The presence of vacancies reduces the characteristic diffusion time by lowering the migration energy for hydrogen. Further, this might suggest that NaH crystallites play a role in dissociating hydrogen molecules at their surfaces [97].

In contrast, the uncatalyzed- NaAlH_4 did not show any exchange of hydrogen with deuterium in NaH. In view of the above discussion, a plausible reason for the absence of H-D exchange in the uncatalyzed NaAlH_4 sample is due to the absence of vacancies in the large NaH crystallites.

4.4 Conclusions

TiCl_3 catalyzed and nanostructured NaAlH_4 has superior reversible hydrogen sorption behavior as compared to uncatalyzed NaAlH_4 . This study showed clear differences in the crystallite sizes of the occurring phases in the catalyzed and uncatalyzed NaAlH_4 . Uncatalyzed NaAlH_4 showed large crystallites, with sizes $\geq 1 \mu\text{m}$, for all occurring phases during the desorption, making it irreversible for deuterium loading. On the other hand, the catalyzed NaAlH_4 showed the presence of nanocrystallites of NaH and Al with the size of approximately 120 nm, which were maintained during the unloading and loading cycling.

The grain refining action of the reaction products $\text{Ti}_x\text{Al}_{1-x}$ and NaCl for Al and NaH, respectively, is responsible for maintaining the grain sizes to nano-dimension. The nanostructured NaH and Na_3AlH_6 phases showed the presence of abundant hydrogen vacancies, which leads to H-D exchange in nano-NaH at a relatively low temperature of about 150 °C. Nano-size crystallite dimensions reduce the required transport distances of hydrogen and metal ions, while the presence of vacancies facilitates ion diffusion. Therefore, the maintenance of crystallite sizes at the nanoscale during hydrogen cycling and the tailoring of vacancy concentrations are key ingredients for the improvement of the kinetics and reversibility of hydrogenation reactions in light-metal hydrides.

5

Ab initio calculations on NaH

A good hydrogen storage system should have satisfactorily fast hydrogen release and uptake kinetics, while meeting the other stringent storage conditions such as high gravimetric and volumetric densities. Moreover, it should also show high reversibility. The presence of crystal defects is known to have a significant influence on the diffusion of atoms and ions [98–100]. They will, therefore, affect the mass transport in the materials in a direct manner, which is of large significance for the reversibility of the hydrogenation reactions. Therefore, it becomes important to study the presence and the formation of vacancies in the hydrogen storage materials.

A number of recent studies on hydrogen storage and (lithium) Li-ion materials, nano-MgH_{2-x} and nano-Li_xTiO₂, show that nano-sized crystallites may contain very high hydrogen vacancy concentrations and a largely increased lithium solubility [20, 28, 101]. For NaAlH₄, recent experimental and calculation studies shed light on the presence and their effect on the reaction kinetics and reversibility [79, 81]. The neutron diffraction studies [82] (see Chapter 4) showed pronounced hydrogen-vacancy formation in the resulting decomposition products Na₃AlH_{6-x} (approximately 20%) and NaH_{1-x} ($\geq 3\%$) in the TiCl₃-catalyzed and nanostructured NaAlH₄ (see Chapter 4). This study also suggested a further important role of TiCl₃ as a grain refiner, besides acting as a hydrogen split-

ter [23,68,102]. Further, in the nano- NaH_{1-x} phase, an unexpected, clear and relatively fast H-D exchange was also observed. In contrast, this exchange was absent in vacancy deprived large crystallites of undoped NaAlH_4 . It is believed that the transport kinetics and H-D exchange is directly related to the presence of abundant vacancy defects in the nano- NaH phase.

This chapter presents ab initio calculations of the vacancy mediated hydrogen migration energies in bulk NaH and at the NaH (001) surface. In particular, the relevant migration energies were studied in detail, as they control the diffusion and magnitude of the diffusion coefficient for atomic hydrogen in the presence of hydrogen vacancies (H_V) in the NaH lattice. Further, the formation energies for various hydrogen defects, vacancies H_V and interstitials H_I , in the NaH lattice were obtained in all possible charged states (+1, 0, -1) [80]. Various charge states of the defects need to be considered, as the defects introduce additional energy levels in the band structure of this ionic salt host material consisting of Na^+ and H^- ions. Finally, a model on the interface of NaH with NaCl , the latter acting as a nucleation center, was evaluated to explain the large amount of hydrogen vacancies in nano- NaH observed experimentally in the TiCl_3 -doped NaAlH_4 upon hydrogen cycling. The model shows that the formation of an in-between (face-centered cubic) fcc- Na layer is preferred, providing a source for the detected high vacancy concentrations. Notably, mechanisms explaining the relatively fast hydrogen transport in the NaH nano-particles involving Ti can be largely excluded, as it is known that Ti is not incorporated in the NaH nano-particles [103].

5.1 Computational procedure

Ab initio calculations, based on DFT [40,41], were carried out using the USPP and GGA [104,105]. The calculations were implemented in the VASP code [44]. Ultra-soft potentials with the valence states 3s for Na, 1s for H, 3s and 3p for Cl (Chlorine) were used. The geometry optimization calculations were performed with a 200 eV and 219.242 eV energy cut-off for NaH and NaCl , respectively, with the convergence criteria set at

2×10^{-5} eV atom⁻¹. The Brillouin zone was sampled using a Monkhorst-Pack sampling technique [106]. A $5 \times 5 \times 5$ grid was used for bulk NaH, Na, and NaCl using a 64 atom supercell, while $6 \times 6 \times 1$, and $9 \times 9 \times 1$ k -point grids were used for the NaH surface (001) (160 atoms) and NaCl–NaH (001) (320 atoms and 40 atoms) interface calculations, respectively. The equilibrium atomic positions after relaxation of the structure were calculated starting from bulk positions using the refined crystallographic data of Refs. [107, 108] (obtained from ICSD database), and the unit cell parameters were validated by optimizing the unit cell. The calculated unit cell parameters showed minor and expected deviations relative to the experimental values for bulk single crystals of 3% for NaH (experimentally 4.89 Å, calculated 4.73 Å), 4% for fcc-Na (expected 5.33 Å, calculated 5.10 Å), and 3% for NaCl (experimentally 5.63 Å, calculated 5.47 Å). The band gap, E_g , of 3.51 eV for bulk NaH deduced from these calculations is 3% smaller than obtained in a recent other DFT-based study [109], employing PAW potentials. This small difference may be the result of the larger lattice parameter of 4.82 Å, and the other potentials for the interaction between ions and electrons used in the latter study. A very similar overall electron energy density-of-states (DOS) was obtained.

After calculating the equilibrium structure and total energy of the perfect crystal, a hydrogen vacancy (H_V) was introduced into an otherwise perfect lattice. The formation energies for hydrogen-related defects in all charged states (+1, 0, -1) for bulk NaH were calculated. This energy was compared with the energy to create a vacancy at the NaH (001) surface to examine the influence of nanoscale dimensions on the formation energy for a vacancy. Further, migration energies were calculated to study the diffusion through bulk NaH and the near-surface layers of NaH. Additionally, the migration energy for an isolated hydrogen atom in fcc-Na was also studied. All bulk and interface calculations were performed with and without relaxation of selected Na atoms around the defect, while the surface calculations were done without relaxation of atoms. The energy costs to introduce a defect into a perfect lattice, i.e., the formation energy of the respective defect E^f , was calculated as follows [110, 111]:

$$E^f = E(\text{defect}^q) - E(\text{bulk}) \pm \mu_H + qE_F, \quad (5.1)$$

where the first and second term are the total energies of supercells with and without a defect, respectively. μ_{H} is the chemical potential of hydrogen at $T = 0$ K, which is fixed to half of the energy of an H_2 molecule, i.e., 2.21 eV. The sign of the μ_{H} term is positive if a hydrogen vacancy is created and negative in case a hydrogen interstitial is created. The last term in Equation (5.1) relates to charged defects, q is the charge of the defect and E_{F} is the energy of the reservoir with which these charges are exchanged, i.e., the Fermi energy level or the electron chemical potential. The equilibrium concentration χ of a defect at a given temperature T , with the Boltzmann constant k_{B} , can be calculated using

$$\chi = \exp\left(\frac{-E^{\text{f}}}{k_{\text{B}}T}\right). \quad (5.2)$$

Further, the energy and relaxed geometry for a set of different interfaces were calculated, including the Na–NaH (30 atoms), NaCl–Na (30 atoms) and NaCl–NaH (40 atoms) (001) interfaces, motivated by the growth of NaH on NaCl crystallites acting as nucleation centers, as described by Singh et al. [82]. The interface energy (E_{int}) is defined as the difference in the energy of an interface system relative to the energies of the involved bulk crystals, as given in Equation (5.3) below

$$E_{\text{int}} = E(\text{interface system}) - \sum E(\text{bulk crystals}). \quad (5.3)$$

5.2 Results and discussion

5.2.1 Migration energies and diffusion coefficients

The hydrogenation kinetics of a hydrogen storage material is often rate-limited by a diffusion-controlled reaction and transport, determining the effective velocity at which the hydrogen atoms can diffuse through the solid matrix. A hopping model was used to imitate the vacancy-mediated hydrogen diffusion in fcc-NaH.

Based on the hopping diffusion model, a hydrogen atom (neighboring a vacancy) is thermally excited, and vibrates around its equilibrium

position. This vibrational motion has a frequency ν_0 , which is material dependent, and is typically of the order of 10^{12} s^{-1} to 10^{13} s^{-1} . For each of the vibrational cycles, a finite and small probability of hopping into the neighboring vacant lattice site exists, which depends on the relative magnitude of the energy barrier height E_m (the migration energy) and the thermal vibrational energy $k_B T$. The diffusing atom needs to cross this E_m in order to reach the vacancy by pushing the surrounding atoms apart and squeezing through. This process is facilitated, when more than one neighboring lattice sites are vacant. However, these calculations consider the tractable case of hopping into an isolated hydrogen vacancy, which is strictly valid in the limit of low vacancy concentrations.

Mathematically, the model is represented by the expressions given in Equation (5.4) below for the diffusion constant, where the factor $1/6$ takes care of the 3D bidirectional motion in the fcc-sublattice, and s is the distance, which a diffusing atom covers to reach the vacancy (see Figure 5.1 for the case of NaH). The concentration of vacancies χ is in thermal equilibrium given by the Equation (5.2). The diffusion constant defined in Equation (5.4) and Equation (5.5) can be used to calculate the characteristic diffusion time t , given in Equation (5.6), for hydrogen to move out of or into a grain of radius R

$$D = \frac{1}{6} s^2 \nu_0 \chi \exp\left(\frac{-E_m}{k_B T}\right), \quad (5.4)$$

$$D_0 = \frac{1}{6} s^2 \nu_0, \quad (5.5)$$

$$t = \frac{R^2}{6D}. \quad (5.6)$$

These equations are strictly valid for the diffusion of an isolated vacancy solely, since the related diffusion motion of the hydrogen atoms is correlated because the chance of hopping back into the original lattice position is larger than towards other positions. This can be accounted for by a correlation factor ζ which is of order ≤ 1 , which has been discarded here. For the comparison with experiments, the primary interest is in obtaining the correct order of magnitude of the diffusion time scale, rather than a model dependent exact value.

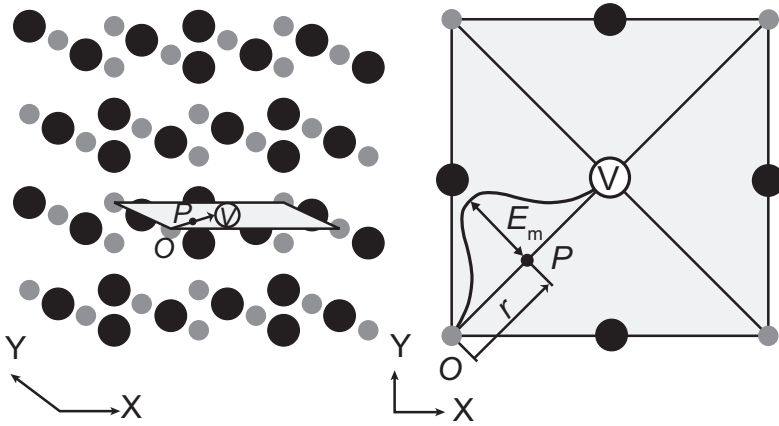


FIGURE 5.1 – A schematic diagram showing the hydrogen path to a neighboring hydrogen vacancy used in the calculations. The selected 10 Na atoms neighboring the vacancy were allowed to relax. Small gray circles represent hydrogen atoms and black large circles represent Na atoms. The big open circle containing “V” represents an isolated hydrogen vacancy.

For NaH, the migration energy for the hydrogen vacancy was calculated in all possible charged states with and without selective atomic relaxation. This was achieved by calculating the cohesive energy of the 63 atoms supercell for different positions of hydrogen on the path toward the hydrogen vacancy moving along the $\langle 110 \rangle$ NaH diagonal (see Figure 5.1). The neighboring 10 Na atoms around the vacancy were allowed to relax. The hydrogen migration energy E_m in the presence of a vacancy was deduced from the resulting curve as shown in Figure 5.2 for a neutral vacancy. E_m is the difference in energy at point O and at the saddle point P , and is 0.94 eV for the case of a neutral vacancy. This is significantly lower than for the case of a direct-exchange of hydrogen with one of its neighboring hydrogen atoms, i.e., in absence of a vacancy, with a calculated migration energy of 4.05 eV. Further, the attempt frequency from the same curve by a parabolic fit near the equilibrium position O was estimated, using Equation (5.7) with k the force constant of the locally harmonic hydrogen vibration

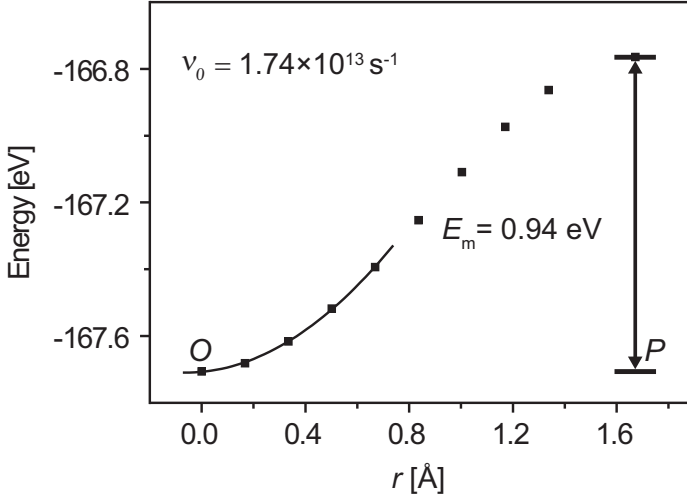


FIGURE 5.2 – Calculated total energy as a function of hydrogen position along the direct path of hydrogen toward the neighboring hydrogen vacancy in bulk NaH. The local minimum at point O was fitted by a parabola for the estimation of the local hydrogen vibration frequency.

$$E = \frac{1}{2}kr^2, \quad (5.7)$$

$$\nu_0 = \frac{1}{2\pi} \sqrt{\frac{k}{m}}. \quad (5.8)$$

The lattice point O corresponds to a local minimum, and point P is a saddle point, which was verified by calculating the total energy as a function of displacement of the hydrogen atom in directions perpendicular to the line connecting the lattice point O and saddle point P . Notably, the obtained frequencies of 17–18 THz (Table 5.1) are situated in the lower part of the high frequency interval of hydrogen dominated vibrations in the phonon DOS for bulk NaH calculated by Ke et al. [109].

The hopping model was used to assess the diffusion coefficients for the various types of vacancies. Subsequently, the characteristic diffusion time was deduced for hydrogen to cover a given distance, corresponding to an average NaH grain size of 60 nm in radius (see Table 5.1). For the neutral vacancy, the thus found time, which is needed for hy-

TABLE 5.1 – Migration energy for hydrogen in the presence of various charged vacancies (+1, 0, -1) in NaH including local structure relaxation, and characteristic diffusion time for hydrogen to cover a diffusion distance of 60 nm at a temperature of 150 °C.

Type of vacancy	$\nu_0 \times 10^{13}$ [s ⁻¹]	E_m [eV]	D [nm ² s ⁻¹]	t [s]
H _V ⁰	1.74	0.94	0.63	950
H _V ⁺	1.72	0.57	1.7×10^4	0.21
H _V ⁻	1.77	1.17	1.29×10^{-3}	4.5×10^5

drogen to cover this distance at 150 °C for the experimentally observed vacancy concentration of 3% (minimum) is 950 s. This is in agreement, to at least within the correct order of magnitude, with the time scale of H-D exchange observed in neutron diffraction measurements [82]. The migration energy of 4 eV, in absence of vacancies, clearly leads to negligible hydrogen diffusion at this temperature and time scales, showing that vacancies are crucial for H-D exchange in NaH at 150 °C.

As expected for isolated hydrogen atoms in fcc-Na, the hydrogen diffusion is here much faster with a diffusion time of the order of 6.7×10^{-4} s only, showing the high mobility of hydrogen in fcc-Na. These calculations further show that the positively charged vacancy H_V⁺ has the lowest migration energy among the three possible types of isolated vacancies in NaH. Therefore, once they are formed, H_V⁺ will induce the fastest hydrogen diffusion rate. In order to cover the distance of a grain radius at 150 °C, a H_V⁺ vacancy concentration of only 5.6×10^{-6} would be needed in order to attain a diffusion time of the order of 950 s. Based on the formation energy of 0.68 eV, as presented in more detail in the next section, an equilibrium concentration of 7.1×10^{-9} at 150 °C is derived, i.e., still lower by 2–3 orders of magnitude. Nevertheless, this shows that, once they are formed, these positively charged vacancies will be highly mobile, and can easily travel macroscopic distances at suitable hydrogen cycling temperatures resulting into a significant increase in the reaction

kinetics in light-metal hydrides. Notably, the diffusion time would be somewhat larger for the case of deuterium atoms, used for example in monitoring the H-D exchange processes, by of the order of $\sqrt{2}$ as of their higher mass.

Considering the effect of the local hydrogen migration energy, it is remarkable that these calculations on the unrelaxed NaH (001) surface indicate that hydrogen moves more easily inwards, deeper into the NaH subsurface region, than outwards to the top NaH layer. The obtained migration energy for a hydrogen atom to move from the second layer to the top NaH layer is, namely, 1.37 eV in the presence of a neutral vacancy, while E_m for the reverse motion from the top layer inwards to the below layer is only 1.22 eV, induced by the weaker binding of the hydrogen atom in the topmost layer.

5.2.2 Formation energies for a variety of defects

Clearly, the formation energy of hydrogen vacancies is an important factor in determining the vacancy concentrations present in the material. This formation energy, together with a vacancy specific hydrogen migration energy, will be the dominant factor in determining the activation energy for diffusion, and correspondingly, the hydrogen kinetics. Therefore, this section focuses on the formation energies of hydrogen vacancies and interstitials in the various charge states. Further, a model relevant for explaining large vacancy concentrations in metal hydride nanoparticles in general was evaluated. It was found that this mechanism can induce the high hydrogen vacancy concentrations in the specific case of NaH nano-particles resulting during the hydrogen desorption reactions of TiCl_3 -doped NaAlH_4 .

Table 5.2 presents the formation energies of neutral and charged vacancies in bulk NaH before and after structural relaxation. Interestingly, the vacancy formation energy for a positive vacancy H_V^+ is substantially lower than that of the negatively charged and neutral vacancies, and is most affected by a structural relaxation in which Na atoms, neighboring the positively charged vacancy, show a distinct outward relaxation. The formation energies of hydrogen vacancies and interstitials in their three

TABLE 5.2 – Formation energies of the H vacancy in the various charged states in bulk NaH and at the NaH (001) surface, calculated with the Fermi energy at 0 eV, i.e., equal to the top of the valence band.

Type of vacancy	Formation Energy [eV]		
	Bulk		Surface
	unrelaxed	relaxed	unrelaxed
H_V^0	2.66	2.61	2.47
H_V^+	1.18	0.68	3.21
H_V^-	4.98	4.93	3.59

charge states are plotted in Figure 5.3 as a function of Fermi level position in the NaH band gap. The zero of the Fermi level is set at the valence-band maximum. Figure 5.3 shows that the combination of a positively charged vacancy H_V^+ with a negatively charged hydrogen interstitial H_I^- , satisfying the charge neutrality condition, has the lowest formation energy, indicating that this combination is the most probable to occur. However, the formation energy of this vacancy-interstitial pair is 1.53 eV, which is still too high to explain the high vacancy concentrations and the fast H-D exchange time scales as observed in neutron diffraction experiments.

Further, the formation energy of an isolated hydrogen vacancy at the NaH (001) surface was calculated, since surfaces play an important role in nano-particles as of their largely increased surface-to-volume ratios. These calculations show that indeed the energy of creating a neutral vacancy at the NaH surface in its topmost layer is more favorable than in the bulk, with a vacancy formation energy of 0.2 eV lower than that of the bulk value. Nevertheless, this effect is too small to account for the observed high hydrogen vacancy concentrations.

The hydrogen vacancy formation at the unrelaxed NaCl–NaH interface at the intermediate Na lattice parameter of 5.10 Å was also considered. The formation energy for an isolated neutral hydrogen vacancy at

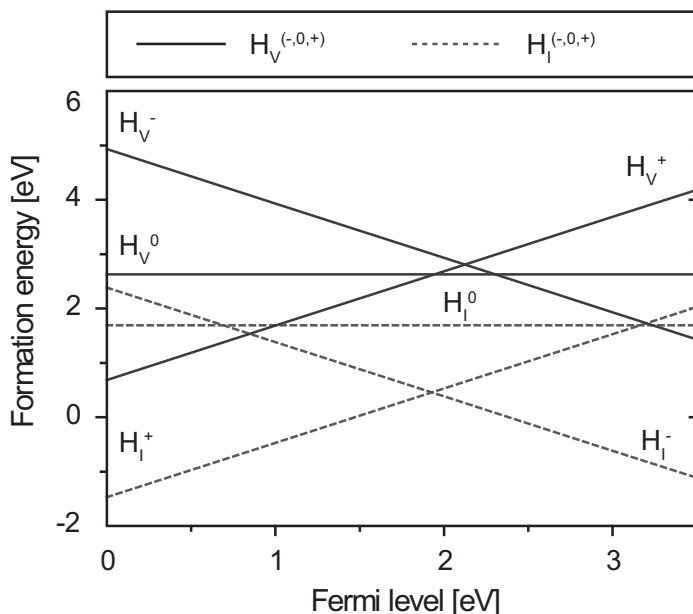


FIGURE 5.3 – Calculated formation energies of hydrogen vacancies and interstitials in NaH as a function of Fermi level position in the band gap. The top of the valence band is taken as the zero of Fermi level.

the interface of 2.53 eV is 5% less than in bulk NaH, and still about 2% larger than for a hydrogen vacancy at the surface.

5.2.3 Mechanism for abundant vacancies in nano-NaH

The calculated formation energies described in the previous section do not provide a satisfactory explanation for the large vacancy concentrations observed in neutron diffraction experiments and inferred from the hydrogen-deuterium exchange detected in nano-NaH. Therefore, a model, which provides a mechanism for the formation of abundant hydrogen vacancy concentrations in metal hydride nano-particle (composite) systems, was evaluated.

NaCl–Na–NaH growth model

In the TiCl_3 -doped NaAlH_4 system, NaCl is formed simultaneously with NaH in the second desorption step [82]. The small and abundant NaCl crystallites very likely act as nucleation centers for subsequent growth of NaH, since NaH and NaCl share the same rock-salt crystallographic structure and a similar ionic bonding at a fair lattice matching. These factors will promote an easy growth of NaH on NaCl nucleation centers. This was examined by calculating the interface energy for a cube-on-cube growth with NaH (100)–NaCl (100). The lattice mismatch for NaH–NaCl, fcc-Na–NaCl, fcc-Na–NaH as deduced from the calculations of the respective bulk equilibrium lattice parameters is 13.5%, 6.7%, and 7.3% for the (001)–(001) interfaces. While other orientations, such as NaH (111)–NaCl (200), may provide a better lattice matching, the occurrence of such an interface is not likely. This is because the atomic bonding is by far less favorable and the resulting interface involves the creation of the energetically unfavorable polar NaH (111) termination. For example, a MgO (100) termination is often observed with the nucleation and growth of embedded nanovoids [112] and nano-particles [113,114] following ion implantation and thermal annealing, showing its large stability. On the other hand, the unfavorable MgO (111) termination is not detected in the electron microscopy studies.

Still, the relatively largest mismatch (13.5%) for the likely case of cube-on-cube growth of NaH on a NaCl (001) surface indicates that possibly an energetically favorable growth may occur with the formation of a narrow interlayer of fcc-Na [115], with a thickness of a few nanometers at most, in-between the NaH and NaCl domains, providing a better matching for the subsequent NaCl–Na and Na–NaH interfaces and a lowering of the local strain in the more gradual growth. Fcc-Na is expected to stabilize in favor of the bcc structure of bulk Na, because of its good lattice matching, while the difference in cohesive energies is very small. Evaluation of the existence of such a driving force to form a narrow interlayer of fcc-Na was done by calculating the interface energies for the NaCl–NaH, NaCl–Na, and Na–NaH interfaces. The interface energies were calculated in such a way that the induced strain energy due to the lattice mismatch is

minimized by a relaxation of the lattice in the direction perpendicular to the interface plane [116], for a set of different fixed lattice parameters in the interface plane. The interface energy is defined as the difference with respect to the energy of the relaxed equilibrium tetragonal bulk systems at a particular fixed lattice parameter in the interface plane [116].

In this way, the interface energy for the NaCl (001)–NaH (001) interface of 0.038 J m^{-2} was obtained. Similarly, the interface energies for the NaCl–Na and Na–NaH interfaces are found to be 0.24 J m^{-2} and 0.28 J m^{-2} , respectively. All these interface energies are quite low, in particular considering the given lattice mismatches, since typical interface energies for cube-on-cube systems with a small lattice mismatch are typically in the range of $1\text{--}2 \text{ J m}^{-2}$. For example, the interface energy for a Au (001)–MgO (001) interface, with a small lattice mismatch of 3.2% only, is in the range between 1.5 and 2 J m^{-2} , see Ref. [117]. The interface energies obtained in these calculations give information primarily about the energy needed to form the different chemical bondings of atoms at the interface. These calculations show that this chemical interface energy is minimum for the NaH–NaCl interface. However, there it is accompanied by a large tetragonal distortion of the NaH lattice to adjust to the NaCl in-plane lattice parameter of 5.47 \AA , with a deformation energy of roughly 0.16 eV per NaH pair relative to equilibrium fcc-NaH. On the other hand, while the formation of the NaCl–Na and Na–NaH interfaces requires relatively more energy to create the chemical bonding as compared to the NaH–NaCl interface, the energy of deformation for Na is very small ($0.008\text{--}0.010 \text{ eV}$ per Na atom). Na indeed is easily deformable, as it has by far the lowest bulk modulus. The value of the bulk modulus is obtained from the equation of state (EOS), which expresses the energy E as a function of the lattice parameter a or volume per Na atom $v = \frac{1}{4}a^3$ for an fcc crystal. The bulk modulus κ is defined by equation (5.9) (Ref. [118]) evaluated at the calculated fcc equilibrium lattice parameter

$$\kappa = v \frac{\partial^2 E}{\partial v^2} = \frac{4}{9a} \frac{\partial^2 E}{\partial a^2}. \quad (5.9)$$

The values for the bulk moduli of NaH, NaCl, and fcc-Na calculated in

this way are 26.5 GPa, 32.2 GPa, and 9.8 GPa, respectively. These values are in close agreement with theoretical and experimental bulk moduli for NaH [119], NaCl [120], and Na [121], reported in the literature. The large difference in the bulk modulus of Na relative to NaH and NaCl confirms that the formation of an intermediate Na layer will aid significantly to minimize the elastic part of the interface energy, as Na is easily deformable. These calculations indicate, therefore, that fcc-Na is likely to form in-between NaCl and NaH upon growth of Na(H) on top of the NaCl small crystallites, as this will lower the overall interface energy needed. Moreover, this also allows for the growth of a more gradual interface region reducing the local strain arising from the larger lattice mismatch between NaCl and NaH.

This proposes that, initially during the second desorption step, fcc-Na indeed grows on the NaCl crystallites while maintaining the fcc (rock salt) crystal structure [115], and subsequently NaH is formed on top. The thin fcc-Na interlayer effectively contains abundant hydrogen vacancies. The high mobility of hydrogen in the fcc-Na lattice will provide a pathway for fast hydrogen or deuterium transport toward or from the NaH_{1-x} nano-particles during H-D exchange or hydrogen sorption processes. The NaCl–Na–NaH growth model, therefore, provides a plausible mechanism explaining the high concentration of hydrogen vacancies¹ and H-D exchange in NaH observed experimentally. A direct consequence is that this will only occur effectively for sub-micrometer sized NaH grains and in the presence of NaCl, consistent with currently available experimental data. Notably, based on this model, the H-D exchange will mainly be through the fcc-Na thin layer between NaH and NaCl crystallites, because it is the major source of the hydrogen vacancies. In [82] the diffraction shows clearly separate NaCl and NaH phases, i.e., the lattices have different dimensions. A fcc-Na interlayer with cell dimensions stretching from NaH to NaCl will be taken as contributing to the NaH (and NaCl) diffraction pattern(s) for those Na fractions that have positional parame-

¹Assuming a thickness of approximately 1 nm for the fcc-Na interlayer and a contact area of roughly 10% of the surface of a NaH crystallite ($R \approx 60$ nm) with the neighboring NaCl ($R \approx 20$ nm), nucleation centers, leads to an estimated hydrogen vacancy fraction χ of approximately 0.5%.

ters that are within the range of the thermal displacement factors (temperature factors). Based on the actual temperature factors for Na in NaH, it is estimated that about 1/4 of the Na interlayer contributes to the NaH diffraction pattern, 1/4 to NaCl and $\sim 1/2$ to a (invisible) background.

5.3 Conclusions

These calculations clearly show that the presence of hydrogen vacancies significantly affects the hydrogen migration energy in NaH, resulting in faster diffusion, and enabling H-D exchange in nano-NaH as observed upon decomposition of ball-milled TiCl₃-doped NaAlH₄. The estimated rate of the vacancy-mediated hydrogen transport based on diffusion theory is consistent with observed H-D exchange reaction rates. The formation energies for intrinsic hydrogen vacancy-interstitial pairs are too high to explain the observed high hydrogen vacancy concentrations inside the NaH phase.

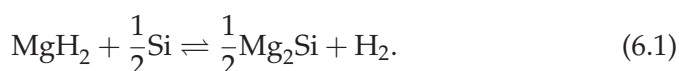
A model to provide an insight into the mechanisms leading to the presence of abundant hydrogen vacancies was evaluated. The calculated low fcc-Na–NaCl and NaH–fcc-Na (001) interface energies show that a rational mechanism to induce abundant hydrogen vacancies by promoting the growth of an fcc-Na interlayer between NaH crystallites and the NaCl nucleation centers is rational. The calculated low interface energies support the view that NaH grows easily on NaCl nucleation centers, and assist the idea of the role of NaCl as grain refiner for NaH.

6

Si destabilized MgH₂

Light-metal hydrides are attractive materials for hydrogen storage because of their relatively large storage capacity [14, 122–124]. However, most of the high capacity hydrides are very stable, and release hydrogen at relatively high temperatures, i.e., above 250 °C. One of the approaches to address this thermodynamic constraint is to combine the existing hydrides with suitable element, a binary compound or with complex hydrides and form new compounds or alloys upon dehydrogenation [24] for specific combination. This approach is expected to increase equilibrium hydrogen pressures by lowering of the overall enthalpy for the modified dehydrogenation reaction, and it effectively destabilizes the composite hydrides.

A well known and promising metal hydride, i.e., MgH₂, suffers from high operation temperatures. It has an equilibrium pressure of 1 bar at 280 °C. An approach to destabilize MgH₂ in the presence of Si led to an increase in the equilibrium hydrogen pressure from 1.8 bar to more than 7.5 bar at 300 °C [24]. This occurs at the expense of an expected decrease in the hydrogen capacity to 5.0 wt.% due to Si addition. Upon heating a MgH₂-Si mixture, the hydrogen can be released in a single dissociation step with the formation of Mg₂Si instead of Mg [24, 102, 125, 126]



However, a major challenge remains to make the reaction reversible, i.e., forming MgH_2 from Mg_2Si upon hydrogenation. So far only one study reported the successful loading near room temperature of Mg_2Si during ball milling while applying in situ hydrogen pressures up to 20 bar [126]. This study therefore indicates that the irreversibility of reaction (6.1) may be due to very slow kinetics for a significant hydrogenation to occur. Further, the maintenance of crystallite sizes to nano-dimensions, and possibly also the presence of vacancies by ball milling throughout the cycling facilitated the reaction kinetics and led to a successful loading of Mg_2Si .

In line with the previous studies reported in this thesis, the grain sizes need to remain small during the hydrogen cycling to facilitate reversibility. Therefore, suitable grain refining agents are needed, which may arrest the crystallites sizes at the nanoscale during the hydrogen cycling reaction [82]. This was a motivation to investigate the evolution of crystallite sizes and their effect during the hydrogenation of Mg_2Si using a grain refiner agent. Nb_2O_5 was an obvious choice, as it is known to show the superior catalytic activity for MgH_2 [20,25,101,127]. In particular, the reaction products Nb and/or MgO were anticipated to act as possible grain refiner for Mg_2Si . Figure 6.1 shows the fairly good lattice matching of the cubic Nb and MgO with Mg_2Si . In this study, two types of samples, powders as well as films, were investigated.

Nb_2O_5 -catalyzed MgH_2 -Si powder Powder samples were used to study the evolution of grain sizes of the occurring phases. The grain sizes were extracted from the broadening of the peaks using GSAS on the obtained ex situ XRD patterns before and after the milling of the powder mixture, after the dehydrogenation, and subsequent hydrogenation steps. The detailed study on the size evolution showed that very small grain sizes of MgH_2 of approximately 10 nm can be achieved by milling in the presence of Si for 30 min only. The Si also reaches small crystallite sizes of 100 nm. Nano- Mg_2Si (80 nm) was formed during desorption in the temperature range of 25–320 °C of the Nb_2O_5 -catalyzed MgH_2 -Si mixture. Despite of the nano-dimensions of the crystallites; however, the Mg_2Si could not be reloaded successfully with hydrogen.

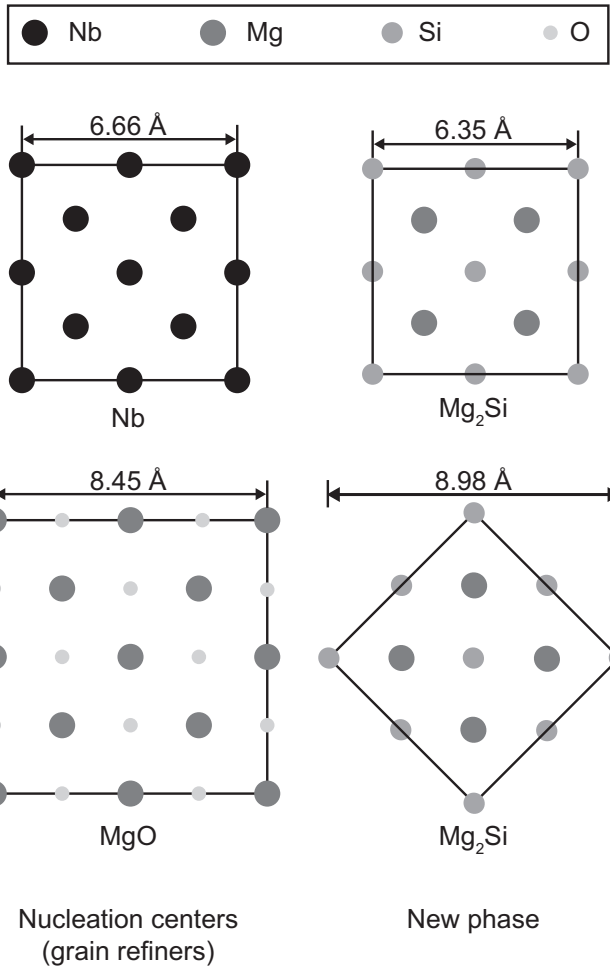


FIGURE 6.1 – A good lattice matching is a requirement for grain refinement to occur. Fcc-Nb (100) and rock salt-MgO (100) show a fairly good lattice matching with the fluorite-Mg₂Si at the given relative orientations of the cubic structures.

Pd-catalyzed Mg-Si thin film To further understand the behavior of the irreversibility of the Mg₂Si upon hydrogenation, Mg-Si bilayer thin films capped with Pd were studied. For the thin films, Pd was chosen to be a

catalyst for a number of reasons. Pd has shown good catalytic activity as a H_2 splitter [102], and it is easy to deposit a Pd-cap layer on top of a Mg-Si bilayer, which further avoids oxidation of the Mg layer. A number of techniques such as positron depth profiling, TEM, SAD, and XRD were used to clarify the (lack of) reactivity of Mg_2Si with hydrogen. These techniques were employed to gain insight into the structural transformations associated with the solid state reactions. Similarly deposited films were heated up to 207 °C under either 10 bar of H_2 or He atmospheres for 24 h to study the reaction path for Mg_2Si formation in the presence or the absence of hydrogen.

6.1 Experimental description

Powder samples were synthesized using the ball milling technique, while the thin film samples were prepared using the PSD technique.

Powder samples The powder samples were synthesized by grinding the powders MgH_2 , Si, and 2 mol% Nb_2O_5 with a MgH_2 : Si weight ratio of (2:1) in a Fritsch Pulversette 6 planetary monomill with a ball to powder ratio of close to 96:1 (128 g of balls:1.328 g of the mixture) for periods of 15 up to 120 min with a rotational speed of 400 rpm. A stainless steel bowl (80 ml) and 32 balls with a diameter of 10 mm were used. The MgH_2 powder of purity 98% was bought from ABCR GmbH & Co., while Si and Nb_2O_5 , each with the purity of 99.99%, were bought from Sigma Aldrich.

For desorption a sample which had been ball milled for 2 h was heated in the temperature range from -173 °C to 320 °C at a rate of 0.3 °C min^{-1} for 15 h. For subsequent rehydrogenation, the sample was placed under 10 bar of H_2 pressure at a number of selected temperatures in the range of 25 to 320 °C for 5–15 h to investigate its reloading behavior. The amount of absorbed H_2 was investigated by performing subsequent desorption measurements using the HYDRA setup.

The ex situ X-ray diffraction was performed on individual as-received MgH_2 , Si, and Nb_2O_5 powders, the milled mixture, the desorbed sample, and the reloaded sample. Cu K_α radiation was used on a Bruker-AXS

Type D5005. All diffraction patterns were fitted by Rietveld refinement using GSAS, and the grain sizes of the various occurring phases were calculated after each treatment from the broadening of the peaks using the Scherrer formula (see Section 2.3).

Thin film samples Mg-Si bilayer films capped with Pd were deposited on glass substrates by the PSD technique (see Section 2.2.1) using an Ar plasma in the pressure ranging from $(1-3) \times 10^{-6}$ bar. Mg (purity 99.9%) and Si wafer (purity 99.99%) targets were used; subsequently, a Pd-cap layer was deposited. Similarly prepared films were heated up to 207 °C under 10 bar of H₂ or He pressure for 24 h using the HYDRA setup (see Section 2.5).

The positron Doppler broadening of annihilation radiation (511 keV) was measured on the as prepared, He treated, and H₂ treated films using positrons with a kinetic energy in the range of 0–25 keV. The technique will show the changes (if there is any) in the electronic structure and phase probed by the positron, and possibly vacancy formation, upon hydrogenation. The *S* parameter depth profiles were analyzed using the VEPFIT software package (see Section 2.8).

The films were characterized by XRD using a Bruker-AXS Type D5005 diffractometer at the Cu K_α wavelength. Further, TEM and SAD studies were carried out on both selected powder and thin film samples using a Philips CM30T microscope at 300 kV.

6.2 Powder samples

Microstructural studies

The XRD pattern obtained for the ball milled (2 h) sample shows the presence of the MgH₂, Si, and Mg_{0.33}Nb_{1.67}O₃ phases (see Figure 6.2). A detailed study of the size evolution of the phases with milling time showed that the crystallite sizes for MgH₂ were reduced from 160 nm to roughly 10 nm in only 30 min of milling time in the presence of Si and the catalyst Nb₂O₅. The Si reduces from 285 nm to 100 nm in the same time

interval. After 60 min of ball milling, the size of MgH_2 further reduces to 5 nm, while the size of Si decreases to 50 nm. Upon ball milling for 120 min, both MgH_2 and Si did not show any further reduction in the crystallite size.

The sample was subsequently dehydrogenated in the temperature range of 25–320 °C for 10 h. Note that a presence of 10 bar hydrogen pressure is expected to be above the equilibrium pressure at a temperature of 25 °C for reaction (6.1). The subsequent XRD on the sample shows the presence of Mg_2Si , MgO , $\text{Mg}_{0.33}\text{Nb}_{1.67}\text{O}_3$, and some residual Si. The initial size of the formed Mg_2Si crystallites was 80 nm. Subsequent thermal desorption up to roughly 280 °C after an attempt of hydrogenation at 25 °C for 15 h showed no change in the pressure as well as quadrupole signal. This shows that hydrogen loading was not achieved under the above mentioned conditions. Under 10 bar of hydrogen pressure for 5 h for a rather small increase in the size of Mg_2Si to 100 nm was observed temperatures up to 320 °C (see Table 6.1).

The XRD study shows that the Mg_2Si phase appears only after the dehydrogenation. No formation of Mg_2Si was observed after 2 h of ball milling (see Figure 6.2). Mg_2Si could not be loaded successfully.

The crystallite size of Mg_2Si does remain at a nanoscale dimension even after application of relatively higher temperatures close to 320 °C, indicating that the grain refining action, probably of MgO , is quite effective. However, it seems that the maintenance of a small grain size of roughly 100 nm is not enough to make the reaction (6.1) reversible, since no trace of formation of MgH_2 from Mg_2Si upon hydrogenation was observed.

Further, TEM micro-graphs on the powder mixture before milling clearly show that Si and MgH_2 particles are well separated with no grain boundaries and with no signs of the presence of any type of oxides e.g. SiO_2 , MgO , and/or $\text{Mg}_{0.33}\text{Nb}_{1.67}\text{O}_3$. After the milling, there were no signs of Mg_2Si phase observed by TEM either. In addition to MgH_2 and Si, oxides, such as SiO_2 and MgO , and pure Nb were now observed. Further, the TEM shows pure Nb particles attached to MgH_2 particles; however, it is not clear if any chemical bonding across the interface between the Nb

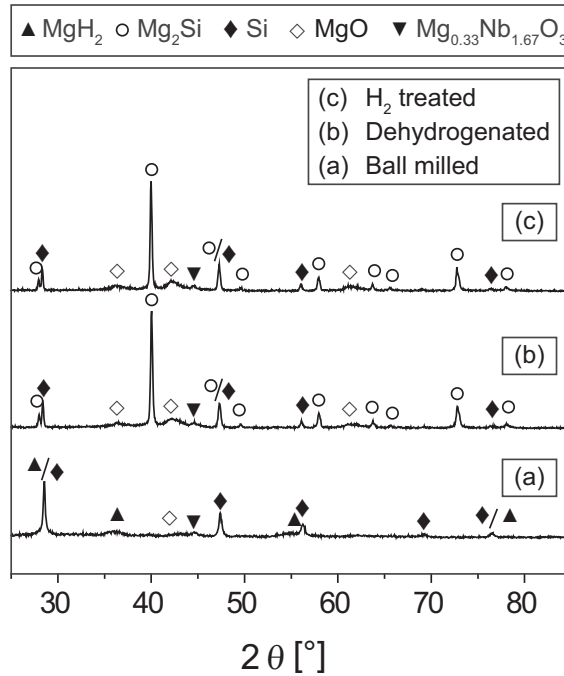


FIGURE 6.2 – XRD showing the occurring phases after 2 h ball milling, dehydrogenated for 15 h up to 320 °C, and under 10 bar of hydrogen pressure for 5 h up to 320 °C.

and MgH_2 exists. Moreover, TEM images show that Mg_2Si was formed only after the dehydrogenation step, and no formation of a MgH_2 phase was observed after the hydrogen loading step, consistent with the XRD results.

In brevity, both XRD and TEM studies show that the grain refinement activity of either Nb or MgO is effective, but hydrogen loading at various temperatures is unsuccessful. In order to gain a further insight into the apparent irreversibility of Mg_2Si , the local transformations associated with the solid-state reactions were studied. Mg-Si bilayers capped with Pd were studied using a number techniques including positron depth profiling, TEM, and XRD (see Section 6.3).

TABLE 6.1 – Evolution of grain sizes of the different occurring phases in a powder mixture of Nb_2O_5 -catalyzed MgH_2 and Si before and after milling and after dehydrogenation and hydrogenation.

Sample treatment	Grain sizes [nm]			
	MgH_2	Si	Nb_2O_5	Mg_2Si
As received	160	285	60	
2 h milling	5	50		
Dehydrogenated (15 h 25–320 °C)		125		80
H_2 treated (5 h 320 °C 10 bar)		150		100

6.3 Thin film samples

6.3.1 Mg_2Si formation in H_2 and He atmospheres

In order to better understand the interaction between Mg and Si above room temperature, the evolution of samples consisting of a Mg-Si double layer capped with a Pd top layer deposited on a glass substrate were investigated upon heating with and without the presence of hydrogen.

Figures 6.3(a) and 6.3 (b) show representative positron depth profiles of the Doppler S parameter for He heated and hydrogenated Mg-Si thin films, respectively. The three regions correspond to a roughly 5 nm thin Pd cap layer, a Mg metal layer with a thickness of nearly 400 nm, an approximately 250 nm thick Si layer, and the glass substrate. The solid lines in Figure 6.3 represent the fit using VEPFIT analysis [57] of the Doppler depth profiles. The drop in the value of the S -parameter around 5 keV, i.e., close to the Mg and Si interface, corresponds to the formation of Mg_2Si .

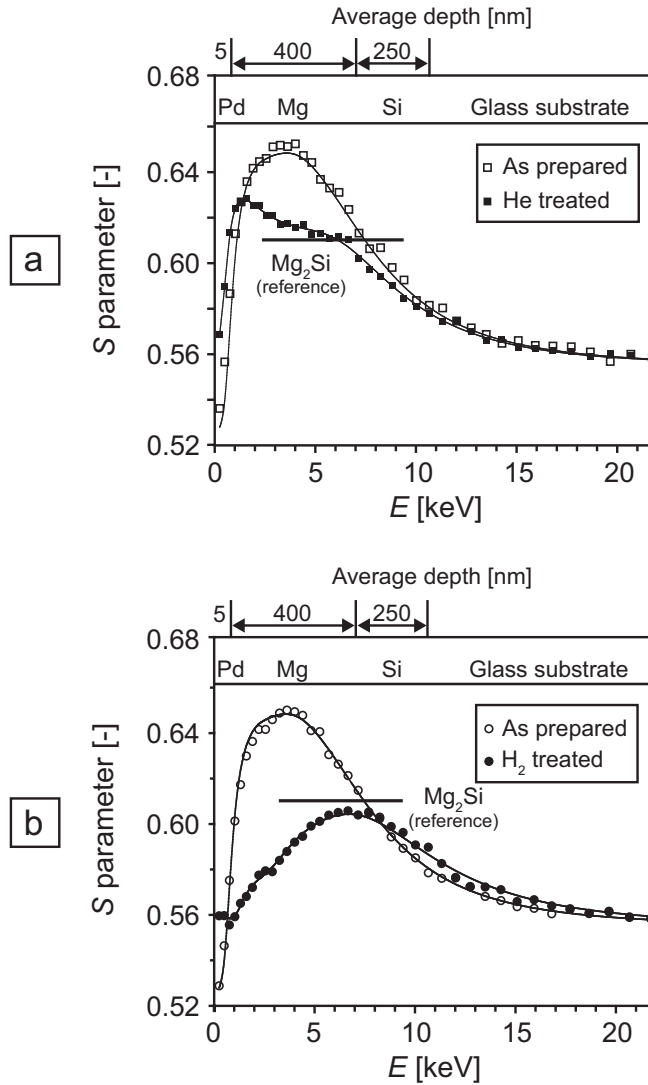


FIGURE 6.3 – (a) Doppler S parameter depth profiles for as-deposited Pd-capped Mg-Si bilayer thin film (hollow squares), and after heating to 207 °C under 10 bar of He atmosphere (filled squares); (b) Doppler S parameter depth profiles for Pd-capped Mg-Si bilayer thin film (hollow circles), and after the heat treatment at 207 °C under 10 bar of H₂ pressure (filled circles).

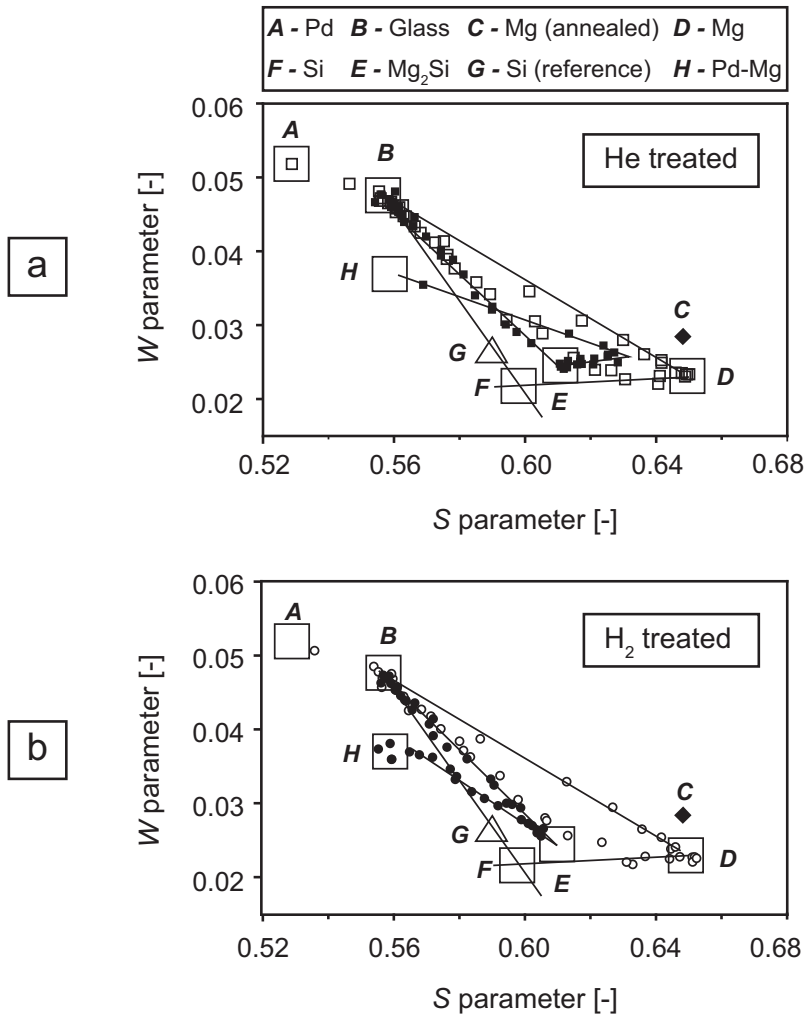


FIGURE 6.4 – (a) $S - W$ diagram corresponding to He treated sample; and (b) A graph between S and W parameters corresponding to hydrogen heated film.

Further, the $S - W$ graphs show a new cluster point, corresponding to Mg₂Si phase ($S = 0.61, W = 0.025$) after the heat treatment in both cases (see Figure 6.4(a) and 6.4(b)).

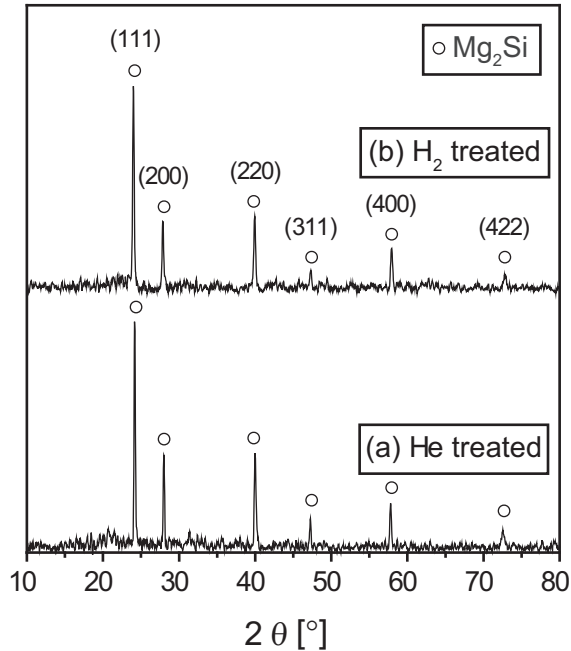


FIGURE 6.5 – XRD showing that irrespective of the gas atmosphere (He or H_2), heating of Mg-Si bilayer system results into Mg_2Si formation.

Subsequent XRD studies on both types of sample after heating with and without a hydrogen atmosphere showed the Mg_2Si formation. This indicates that heating up to 207 °C only is enough to form the Mg_2Si phase. No other crystalline phases besides Mg_2Si were detected in the XRD patterns (see Figure 6.5).

6.3.2 Different pathways for Mg_2Si formation

Notably, for a positron implantation energy of <5 keV, the positron depth profile shows (see Figures 6.3(a) and 6.3(b)) a different evolution of the layers at the Pd-Mg interface for the samples treated with and without the application of hydrogen. This difference is further clearly visible in the Figures 6.4(a) and 6.4(b). The S-W point for the sample treated under He atmosphere (see Figure 6.4(a)) first moves from the Pd-Mg top layer

in the direction of the Mg *S-W* cluster point, suggesting the presence of a rather thin (amorphous) Mg-rich layer near the Mg-Pd interface. Beyond this implantation energy, positrons progressively see mainly the formed Mg_2Si as seen from corresponding *S-W* cluster point. On the other hand, the hydrogen loaded bilayer sample shows a change from the *S-W* point of the Pd-Mg cap layer directly toward that of Mg_2Si (see Figure 6.4(b)).

This difference in the evolution of the layers close to the Pd-Mg interface can be attributed to the initial formation of MgH_2 at the top part of the Mg layer expected on the basis of earlier successful loading of Mg films deposited on Si wafers (see Chapter 3). At this stage, Mg_2Si formation at the Mg-Si interface will occur simultaneously. This latter reaction will even be accelerated relative to the sample treated under a He atmosphere by the significant heat release and local temperature rise caused by the hydrogenation of the pre-layer to MgH_2 having a high enthalpy of formation. As soon as the Mg_2Si zone is in contact with the MgH_2 layer, destabilization will be effective, and the applied hydrogen pressure of 10 bar will no longer be sufficient at the high temperature of the experiment to hinder complete hydrogen desorption of the MgH_2 pre-layer, and a full transformation to Mg_2Si will be reached. This proposed model of evolution of the layers and the finally reached Mg_2Si formation in the hydrogen heated Mg-Si bilayer system is depicted in the Figure 6.6 and further supported by the TEM micrographs on He and H_2 heated samples (see Figure 6.7).

Further, besides showing a columnar growth of Mg_2Si phase similar to deposited Mg films [102], the TEM image shows the presence of an unreacted thin and homogeneous Si layer. The latter remains unreacted because of the non-stoichiometric ratio $\text{Mg}:\text{Si} < 2:1$ for the Mg and Si layer thicknesses used in this study. Additionally, for the He heat treated samples, TEM images reveal the presence of an amorphous layer on top of the Mg_2Si layer. In the H_2 treated sample, on the other hand, this amorphous layer is absent, showing the consistency with the positron depth profiles at shallow depths close to the Mg-Pd interface. Most probably, this amorphous layer consists of a partially unreacted amorphous Mg or Mg-rich compound as can be clearly seen in the Figure 6.3(a). However,

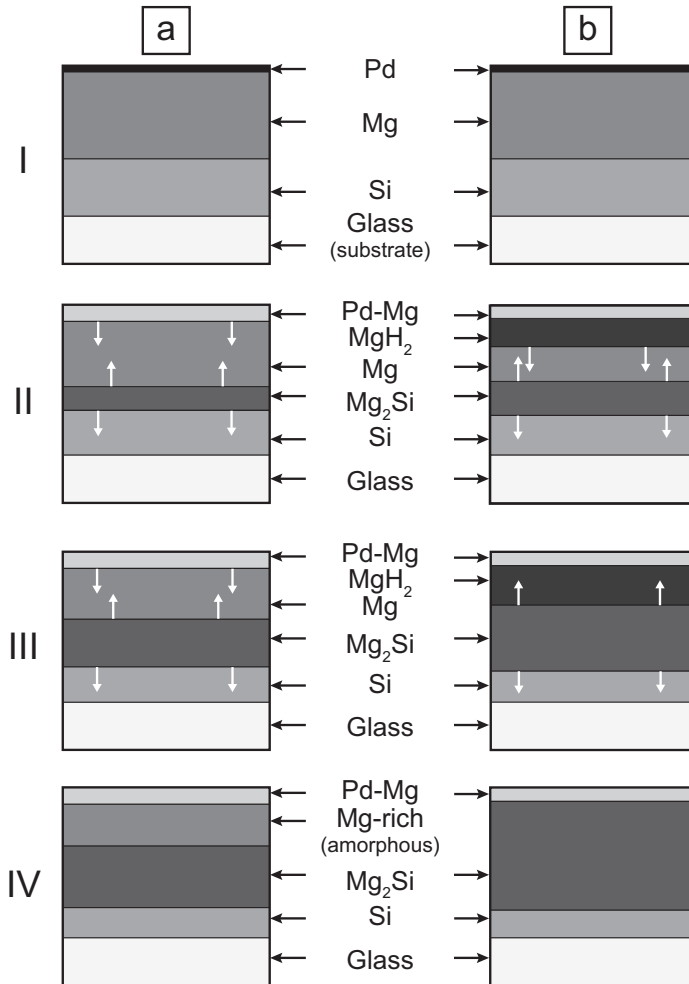


FIGURE 6.6 – Schematic drawing of the proposed evolution of Pd-capped Mg-Si bilayers on a glass substrate upon prolonged (a) heating at 207 °C at a pressure of 10 bar in an inert He gas environment; (b) in a hydrogen gas environment. The hydrogen loading leads to a higher local temperature and faster transformation to Mg₂Si, and inhibits the formation of an amorphous Mg-Pd or Mg-Si pre-layer. The initially formed MgH₂ releases all hydrogen upon reaching in contact with Mg₂Si.

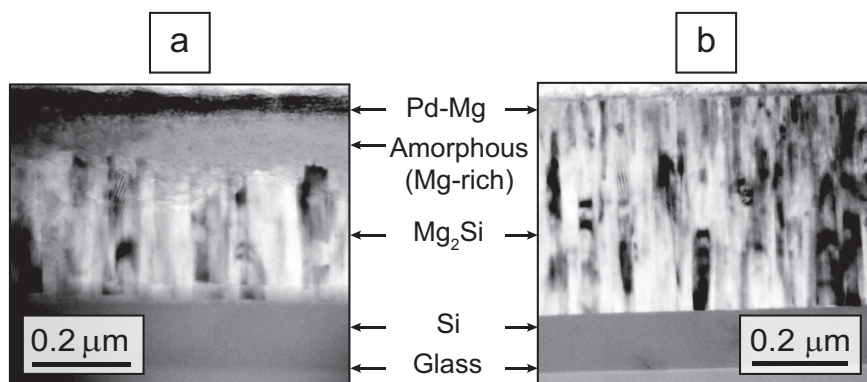


FIGURE 6.7 – Cross-sectional TEM images of Pd-capped Mg-Si bilayer films heating at $207 \text{ }^\circ\text{C}$ for 24 h with 10 bar of pressure (a) He (b) H_2 atmosphere. Both samples show the Mg_2Si formation on top of a thin residual Si layer. Further, the sample heated under a He atmosphere shows the presence of an amorphous layer, presumably Mg-rich in composition.

no such phase was observed in the XRD, which is related to the amorphous nature of the phase. Both Mg-rich Mg-Pd alloys and Si-rich and Mg-rich Mg-Si alloys may form amorphous layers in sputtered deposited films [128,129].

6.3.3 Possible mechanism for the irreversibility of Mg_2Si

The origin of the irreversibility of the formed Mg_2Si with subsequent hydrogenation most likely is related to the difficulty of removal of Mg from the Mg_2Si from its local tetrahedral binding geometry surrounded by four neighboring Si atoms. While thermodynamically the rehydrogenation step is favored at sufficiently high hydrogen pressures above the equilibrium pressure, the presence of a reaction barrier related to removal of Mg from Mg_2Si may obstruct the formation of local MgH_2 nuclei. This could also provide an explanation to the observed (partial) reversibility under in situ ball milling conditions using a 20 bar H_2 pressure, since ball milling of metal hydrides often leads to stabilization of non-equilibrium phases,

and may further aid to overcome reaction barriers. One of the other mentioned bottlenecks proposed in the literature, namely slow hydrogen dissociation at Mg_2Si surfaces, can be disregarded since hydrogen is readily present in its atomic form in the thin film studies [130]. Clemens et al. recently showed, in fact, that atomic hydrogen can easily permeate Pd-capped Mg_2Si layers to fully hydrogenate Mg films underneath. Recent ab initio calculations [131], moreover, show that hydrogen may dissociate easily at particular, oxygen-free, surfaces such as the Mg_2Si ($\bar{1}10$) surface.

6.4 Conclusions

XRD and TEM studies on powder samples show grain refinement is effective, but that using particle sizes around 100 nm is not sufficient to achieve the reversibility of Mg_2Si . The solid state reactions of Mg-Si bi-layers upon hydrogen loading and heat treatment in an inert gas environment were monitored. Both treatments lead to relatively fast Mg_2Si formation. Positron depth profiling revealed the appearance of an amorphous Mg-rich pre-layer for heating in inert gas environment solely, consistent with the electron microscopy study. Re-hydrogenation of Mg_2Si is difficult, most likely related to the presence of a barrier against removal of Mg from the Mg_2Si layer, inhibiting the formation of MgH_2 . This suggests that reversibility could possibly only be achieved using an appropriate additive, which can lower the reaction barrier related to the removal of Mg from Mg_2Si matrix during hydrogenation step, and which also facilitates the nucleation of MgH_2 crystallites in combination with smaller nano-crystallites.

7

TiF₃ catalyzed MgH₂

The addition of suitable catalysts and small crystallite (particle) sizes are known to improve the sorption kinetics in hydrogen storage materials. Starting with an initially small crystallite size is possible by grinding the powder in a ball milling; however, these crystallites are known to grow by spontaneous annealing during the hydrogen cycling [20]. Therefore, maintaining the crystallite sizes to nano-dimensions throughout the sorption reactions is a challenging task in hydrogen storage research. A recent study has shown an approach to restrict the growth of the crystallites size during a sorption reaction by revealing an additional role of the TiCl₃ catalyst as a grain refiner for the occurring phases, besides acting as a H₂ molecule splitter in the study on TiCl₃-catalyzed NaAlH₄ [82]. This study is a motivation to look for appropriate catalysts which can act as grain refiners for the other potential hydrogen storage candidates, especially for a well known hydrogen storage material, i.e., MgH₂. In MgH₂, catalysts like Nb, V, Nb₂O₅ were also shown to have an effect on crystallite size [20,25]. Nb₂O₅ is known to show superior catalytic activity for MgH₂ [20,25,101,127]; however, no optimization with respect to grain refining activity has been attempted yet.

A number of studies indicate the catalytic activity of TiF₃ (titanium fluoride) in MgH₂ and the formation of MgF₂ [132–135]. These studies

further show that H_2 can be loaded in Mg at room temperature, while the loading at room temperature for Nb_2O_5 -catalyzed MgH_2 has not been reported so far. However, these studies lack a clear explanation about the mechanism by which TiF_3 helps to facilitate this low temperature loading and the relatively faster kinetics. The studies described in the previous chapters suggest that MgF_2 acts as a grain refiner for MgH_2 because MgF_2 shares the same crystallographic structure as MgH_2 [136,137].

Therefore, to investigate the role of MgF_2 as a grain refiner, in situ neutron diffraction measurements were performed on TiF_3 -catalyzed MgH_2 . TiF_3 was taken as a catalyst, as it is known to lead to MgF_2 upon first desorption. Further, the evolution of deuterium vacancies in MgD_2 was also studied during deuterium cycling, for a comparison to vacancy formation in Nb and V-catalyzed MgH_2 [20]. This chapter reports that MgF_2 indeed arrests the crystallite sizes of MgD_2 at a nano-dimension (average crystallite size roughly 30 nm) during the deuterium loading and unloading. Further, these nano-crystallites show approximately 30% of deuterium vacancies in the beginning of the loading, while almost reaching full occupation upon full loading. Upon subsequent desorption at higher temperature the deuterium vacancy concentration rises again to 15%. In addition the material can rapidly absorb H_2 at temperature close to room temperature (RT).

7.1 Experimental procedure

The powders MgH_2 and 5 mol% TiF_3 were milled in a Fritsch Pulversette 6 planetary monomill with a ball to powder ratio of close to 50:1 ((32×4) g balls: 2.67 g of initial weight of total powder) for a period of 60 min with a rotational speed of 400 rpm. A pause of 15 min time was taken after every 15 min rotation interval. The MgH_2 powder, with a purity of 98%, was obtained from ABCR GmbH & Co. KG, and TiF_3 (100%) was obtained from Alfa Aesar.

The size of as-received MgH_2 and ball milled MgH_2 was found to be 150 nm and 30 nm, respectively. The sizes were extracted from the Rietveld fitting on XRD patterns, which were obtained using Cu K_α radi-

ation on a Bruker-AXS Type D5005 or on a PANalytical Type X'Pert Pro diffractometer, respectively.

The handling of all powders was done in the glove box containing argon as a working gas with an O₂ and H₂O content of ≤ 0.1 ppm. All powders (except for the hydrides) and equipment such as balls, bowl, and spatula, etc., were baked out in a vacuum oven at around 80 °C for a few hours before bringing them into the glove box.

After the milling, the sample was desorbed in the glove box using temperatures ranging from 25 to 280 °C. The desorption of the hydrogen gas was measured gravimetrically, i.e., by weighing the sample before and after heating. The sample was heated up to 280 °C, until no more change in the mass of the sample was observed at 280 °C, and the mass loss was 160 mg equivalent to 1.792 liter H₂ gas, corresponding to 6.5 wt.% of hydrogen released from the sample. Subsequently, the sample was characterized using XRD in order to observe Mg crystallite size, catalyst, and residual MgH₂.

In situ neutron diffraction measurements were performed during the D₂ cycling of TiF₃-catalyzed Mg using GEM (see Section 2.6.3) at ISIS. The first loading sequence on the desorbed sample (2.287 g) was performed at 150 °C in the pressure range from 5–10 bar of D₂ pressure. The use of deuterium allows to reduce the incoherent background significantly as compared to hydrogen. This loading sequence consisted of 11 loading steps at 150 °C with an ultimate pressure up to 10 bar and was performed until the Mg was completely transformed to rutile-MgD₂ (see Figure 7.2(a)).

After the full loading, the D₂ from the sample tubing was pumped away rapidly down to a pressure of 300 mbar. At this pressure D₂ slowly removed from the MgD₂. The sample was heated gradually up to 320 °C in order to remove D₂ from the MgD₂ completely. After full desorption, the sample was cooled to 50 °C, and a subsequent D₂ loading was attempted at this low temperature successfully. At this temperature, 9 steps of D₂ loading in the pressure range up to 10 bar were performed. Some extra shots of 10 bar of D₂ pressure were applied at 100 and 150 °C in order to achieve a complete transformation of Mg into MgD₂.

A neutron diffraction pattern was acquired for every 7.5 min during the D_2 loading and unloading as described above. However, the first pattern was taken for 16 min for a reference at a higher statistics. All diffraction patterns were fitted using Rietveld refinement using the software package GSAS (see Section 2.6.4). The detector banks 4, 5, and 6 of GEM (ISIS, UK) were fitted simultaneously,¹ while the phase fractions, the lattice parameters, and the line shapes were allowed to vary. The fits of the phase fractions were constraint among the three detector banks to retain mutual consistent values. The crystallite sizes of the occurring phases were extracted from the broadening of the peaks using the Scherrer's formula.

7.2 Results

The XRD on the ball milling sample showed the presence of $\beta\text{-MgH}_2$, $\gamma\text{-MgH}_2$, TiF_3 , and traces of MgO . A significant amount of 35% (in weight) of the total desorbed hydrogen was released already at 200 °C in 20 min upon subsequent desorption in the glove box. Upon further heating, more hydrogen gas was released. At 280 °C, no further change in the mass of the sample was observed. A subsequent XRD on the sample showed the presence of Mg , MgF_2 , traces of TiH_x , and a small amount of MgO . Notably, no TiH_2 peaks were observed directly after the milling, strongly indicating that the formation of TiH_x occurs upon heating [133]. The proposed reaction path way of the formation of TiH_x is described below in the Section 7.2.1.

7.2.1 In situ neutron diffraction on TiF_3 catalyzed Mg

The colored 3D diffraction plot (see Figure 7.1) shows the development of phases (Mg , MgF_2 , MgO , and MgD_2) upon D_2 cycling on TiF_3 -catalyzed Mg . Figure 7.2(a) shows the temperature conditions during the D_2 loading and unloading cycle over time at different temperatures.

¹A few selected fitted patterns are shown in Appendix B.

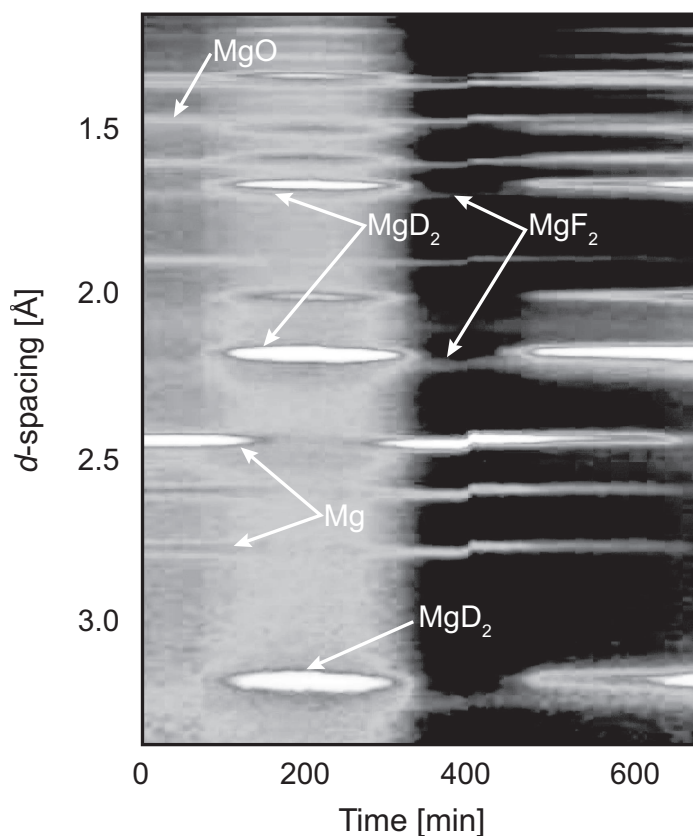


FIGURE 7.1 – Neutron diffraction patterns showing the evolution of occurring phases such as Mg, MgF₂, MgO, and MgD₂ over a section of *d*-spacings during D₂ cycling of TiF₃-catalyzed MgD₂.

The fate of the TiF₃ catalyst

There was no residual MgH₂ visible in the XRD, nor in the neutron diffraction for the initial sample after first desorption. However, in the 2D graph of the diffraction (see Figure 7.1), it is clearly visible that an incoherent background is present at the start of the experiments. This background disappears only after full loading with D₂ is completed and upon subsequent unloading at $T > 300$ °C (for $t > 300$ min, see graphs

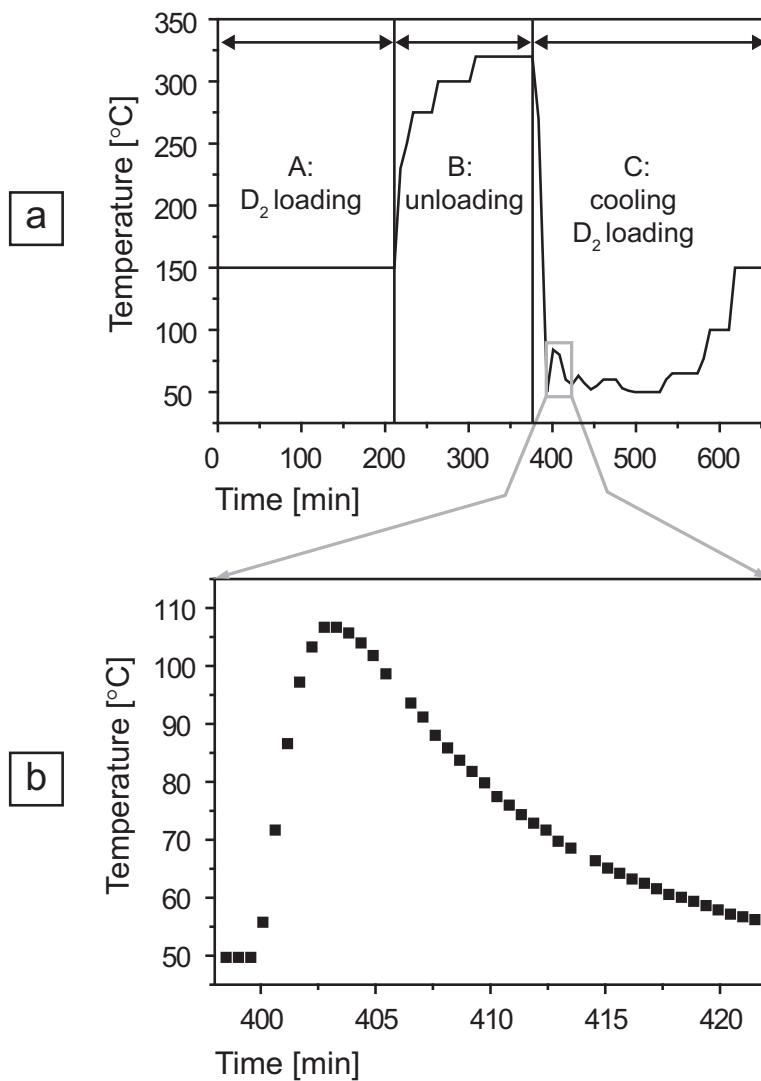
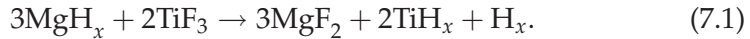


FIGURE 7.2 – (a) Change in temperature is plotted over time describing loading and unloading steps of TiF_3 -catalyzed MgD_2 ; (b) A sudden increase in the temperature up to 107 $^{\circ}\text{C}$ was observed upon 50 $^{\circ}\text{C}$ loading, which is encircled in (a).

Figure 7.1 and 7.2(a)) is performed. The presence of the incoherent background directly points to the presence of residual hydrogen (protons) in the desorbed sample containing Mg-metal. The presence of crystalline MgH_2 nevertheless can be ruled out based on XRD and neutron diffraction.

The fluorine from TiF_3 appears to have reacted with the MgH_2 to form MgF_2 ; and in the process both H_2 and Ti are liberated [133], the latter binding a fraction of the hydrogen



TiH_x is formed since its equilibrium pressure is much lower than MgH_2 at the same temperature (for all temperatures between room temperature to 320 °C). The hydrogen desorption during preparation of the initial desorbed sample can easily result in fully desorbed Mg, while still Ti is hydrided. $\text{TiH}_{1.5 < x < 2}$ has an equilibrium pressure of 10^{-2} mbar at 300 °C [138], while 280 °C was used for the initial desorption.

Loading at 150 °C

At the first step of first loading, approximately 140 ml of deuterium gas was absorbed within 3 min at 150 °C. After 200 min and several D_2 loadings, almost all Mg was transformed to MgD_2 with only 2% of residual Mg remaining. The evolution of the occurring phases in relative phase fractions, extracted from the Rietveld analysis, over time is shown in the Figure 7.3. The figure shows that roughly 10% MgF_2 was present from the beginning of the first loading and the amount of MgF_2 remains constant throughout the cycling process. A small fraction of MgO (5—7%) was present throughout the cycling process.

D_2 desorption

Desorption started at 150 °C, but the desorption was slow, i.e. roughly 1 ml min^{-1} . The pressure in the sample tube was roughly 320 mbar. Subsequently, the temperature was increased gradually up to 320 °C (see Figure 7.2(a)), and then the rate of deuterium release was increased to

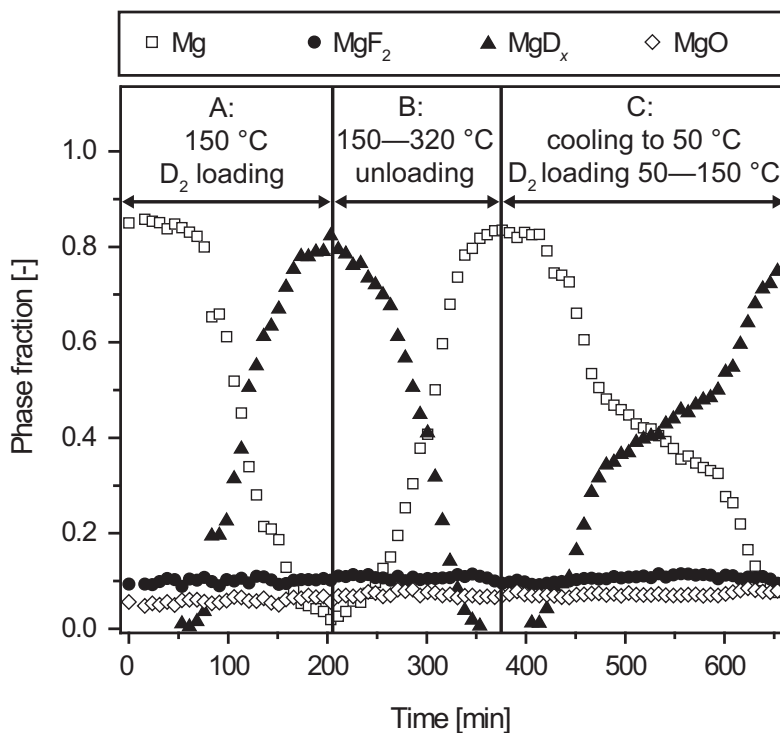


FIGURE 7.3 – Fraction of different phases were plotted over the measurement time. The plot is divided into 3 intervals. A: D_2 loading at 150 °C; B: D_2 desorption from the temperature ranging from 150 °C to 320 °C; C: cooling the system down to 50 °C and subsequent D_2 loading in the range of 50–150 °C. The applied D_2 ranged from 5–10 bar.

approximately 5 ml min^{-1} . A valve was used to control the D_2 flow, while maintaining some pressure in the sample tube. The deuterium was completely desorbed after 145 min (see Figure 7.3).

Loading at 50 °C

After the complete transformation of MgD_2 into Mg with the release of D_2 at 320 °C, the sample was cooled down to 50 °C. Subsequent loading at 50 °C led to the reappearance of the MgD_2 phase, which can be di-

rectly observed in the colored plot (see Figure 7.1). Roughly 284 ml of deuterium was absorbed in 3–4 min at 50 °C. Simultaneously, a drastic increase in the temperature up to 105 °C from 50 °C was observed, showing the exothermic behavior of the reaction (see Figure 7.2(b)). The sample was allowed to cool down to 55 °C, and subsequent gentle stepwise loading was done at 50 °C for 185 min. The deuterium loading was only completed to ~60% at 50 °C, so a few steps up to 10 bar of deuterium pressure at 100 and 150 °C were applied, which appeared sufficient to complete the deuterium loading.

Evolution of grain sizes

A careful Rietveld analysis of the data shows that the crystallites size of MgD_x remain surprisingly small, roughly 30 nm, throughout the deuterium cycling. The average crystallite size of MgF_2 is approximately 12 nm. The crystallite size of Mg also remain relatively small (ranging from 100–150 nm). In Nb or V catalyzed MgH_2 crystallite sizes for Mg and MgH_2 were observed of ~150 nm [20]. The small increase in Mg grain size observed here is due to the increase in temperature and the associated annealing of Mg.

H-D exchange in TiH_x

The TiF_3 catalyst in MgH_2 results in the formation of MgF_2 and TiH_x with $x \approx 2$ at RT. Many studies have been performed on the mobility of hydrogen in TiH_x , and it was shown by neutron and NMR experiments that large hydrogen and deuterium diffusion coefficients are observed [139,140]. Although the mobility of H and D in titanium hydride is high, the hydrogen and deuterium can normally not easily leave the Ti(H,D)_x since the hydrogen and deuterium equilibrium pressures are low.

As soon as the loading of deuterium has started on the desorbed Mg- TiF_3 sample, the hydrogen from TiH_x can escape from TiH_x , when it is exchanged with deuterium. Because of the rapid diffusion, this will already occur within less than seconds [139,140]. Such fast diffusion has been observed in other type of materials, e.g. Li-ion battery materi-

als [141]. The result is that a homogeneous hydrogen-deuterium mixture will be established rapidly within the sample for each loading of deuterium. The ~ 5 mol% of TiH_2 will thus provide a constant amount of H in the hydrogen-deuterium mixture that reduces to $\sim 5\%$ of the added deuterium upon loading. The unloading of deuterium after full loading will result in a 95% reduction of the hydrogen content in Ti(H,D)_x via the MgD_x compound, consequently the incoherent background in Figure 7.1 disappears. With the assumption of a homogenous hydrogen-deuterium mixture the effective neutron cross section can be calculated for each deuterium loading step. This leads to the correction of the measured occupancy numbers, which is presented in Figure 7.4.

Evolution of deuterium occupancy in MgD_x

This exchange expectedly has a correlation with deuterium vacancy formation, namely, a striking observation in Figure 7.4 is that during the D_2 desorption between time between 220 and 300 min, there are large amounts of vacancies present in the MgD_x phase. In [20], such vacancies were also observed, however, in a much more limited period during absorption: close to the beginning of absorption. Further, in the present case, vacancies are also formed close to the end of the desorption process. This is an indication that for these 5 times smaller crystallites of MgD_2 , the creation of vacancies is much more prominent.

The evolution of the D site occupancy in MgD_x was extracted as an important parameter using Rietveld analysis of the neutron diffraction patterns. Figure 7.4 shows that (after correction) approximately 32% of deuterium sites are vacant at the beginning of the loading. These vacancies are filled with deuterium during the subsequent loading. During the desorption, a decrease in the deuterium occupancy site from 0.97 down to 0.86 was observed. A 10% of deuterium vacancies in MgD_x was observed in the low temperature loading at 50 °C which were filled up at higher loading pressures.

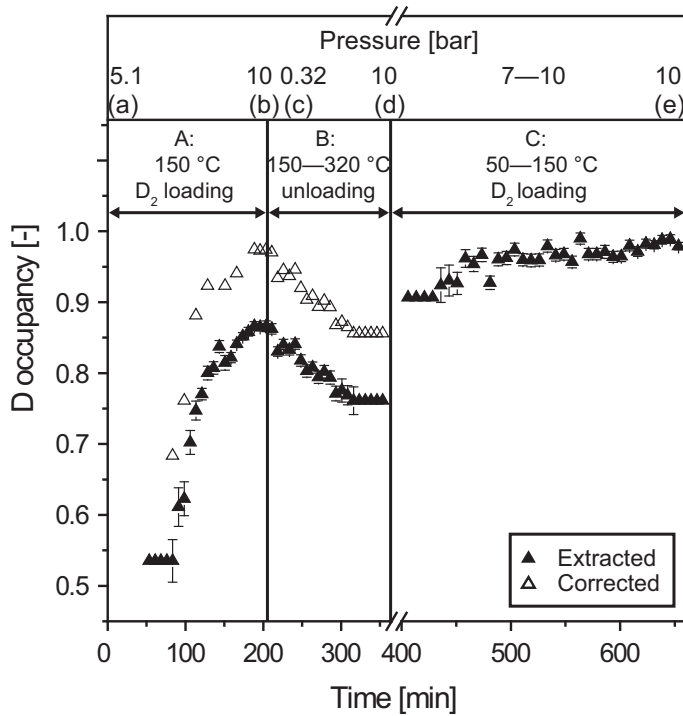


FIGURE 7.4 – The plot shows the change in D_2 occupancy over measuring time. A correction of the occupancy numbers initially extracted from the data was calculated with the assumption of the presence of a homogeneous H-D mixture (5%/95%) coming from the presence of TiH_x in the initial sample. The filled triangles are the corrected occupancy values, while empty triangles represent the measured occupancy number. (a) – the applied pressure at the first step of first loading at $150\text{ }^\circ\text{C}$ was 5.1 bar; (b) – a pressure of 10 bar was applied in order to ensure the complete loading; (c) – during desorption, the pressure in the sample tube was 0.32 bar; (d) – the low temperature loading was started with the application of 10 bar deuterium pressure, followed by a number of steps in pressure ranging from 7–10 bar (region (d) to (e)); (e) – finally ended with the application of 10 bar at $150\text{ }^\circ\text{C}$. Note that at (b) and (c) the same experimental conditions ($150\text{ }^\circ\text{C}$ and 10 bar) result in the same occupancies, showing that consistency is reached after correcting for the initial presence of H_2 . See Figure 7.2(a) for the corresponding temperature changes over time.

7.3 Discussion

7.3.1 Role of MgF_2 as a grain refiner

The neutron diffraction results clearly show that the MgD_2 crystallites remain to have nano-dimensions throughout the D_2 loading and unloading. Previous studies on NaAlH_4 show that the reaction products NaCl and TiAl_x act as grain refiner for NaH and Al , respectively, where NaCl and NaH ; Al and TiAl_x share the same crystallographic structure. One of the requirements for the grain refining action to happen is that the nucleation phase shares the same crystallographic structure as the adherent phase with may be a small lattice mismatch [82]. MgF_2 is known to have the same crystal structure (rutile) as Mg(H/D)_2 with a very small lattice mismatch of approximately 2% [136,137]. These observations clearly show that MgF_2 can act as nucleation centers for MgD_2 , and acts as a very effective grain refiner for MgD_2 crystallites by arresting the growth of the grains size to nano-dimensions. Notably, the MgD_2 crystalline sizes remain much smaller than for example in Nb-catalyzed MgD_2 .

Small grain sizes are further very important in influencing the reaction kinetics by decreasing the diffusion distances [20, 84, 85, 87], and might also be responsible for the vacancy formation [20], which also significantly helps to increase the hydrogen transport kinetics.

7.3.2 Deuterium vacancies during desorption in MgD_x

Strikingly, a strong decrease in the deuterium site occupancy from 0.97 down to 0.86 in the MgD_2 was observed upon heating up to 300 °C during desorption (see Figure 7.4). Notably, such a behavior is not shown by bulk- MgD_2 at the 300 °C so far, indicating that the thermodynamics is affected for nano-crystallites (30 nm in this case). For Nb_2O_5 -catalyzed Mg(H/D)_2 , abundant vacancies have been observed only at the very beginning of hydrogenation [20,101] and the very end of dehydrogenation. However for TiF_3 -catalyzed nano- MgD_2 , these abundant vacancies appear for larger time during the D_2 desorption and absorption.

7.4 Conclusions

The presence of the TiF_3 catalyst added to MgH_2 resulted into the formation of MgF_2 and TiH_x phases during the first hydrogen release. The formed MgF_2 crystallites act as nucleation centers for MgD_2 , and arrest the size of MgD_2 crystallites to 30 nm throughout the deuterium loading and unloading cycle. The MgF_2 containing Mg was successfully loaded at 50 °C. The exothermic behavior of the reaction of Mg with D_2 was clearly observed at 50 °C loading, where a drastic increase in the temperature up to 105 °C was measured. Approximately 60% of deuterium could be loaded at 50 °C. An H-D exchange was observed in the TiH_x phase.

Further, nano-crystallites of MgD_2 showed approximately 30% of deuterium vacancies in the beginning of the loading. These vacancies were fully filled in the subsequent steps of loading. A decrease in deuterium site occupancy from 0.97 down to 0.86 was observed again as a result of deuterium desorption at temperatures around 300 °C during desorption.

A

Fitted patterns on catalyzed NaAlH_4

The background of protonated samples in neutron diffraction is largely due to incoherent scattering on the protons. However, with the high count rate of the GEM diffractometer at ISIS and its advantageous scattering geometry, well resolved diffraction peaks can be obtained on top of the background after relatively short measurement times. The supplementary figures (see Figure A.1 and Figure A.2) presented in this appendix show two representative diffraction patterns together with the Rietveld refinement patterns. The patterns are, before and after subtracting the background, for the TiCl_3 -catalyzed sample collected in time interval “B”, where the Na_3AlH_6 compound is gradually transformed into the NaH and Al reaction products (see Chapter 4).

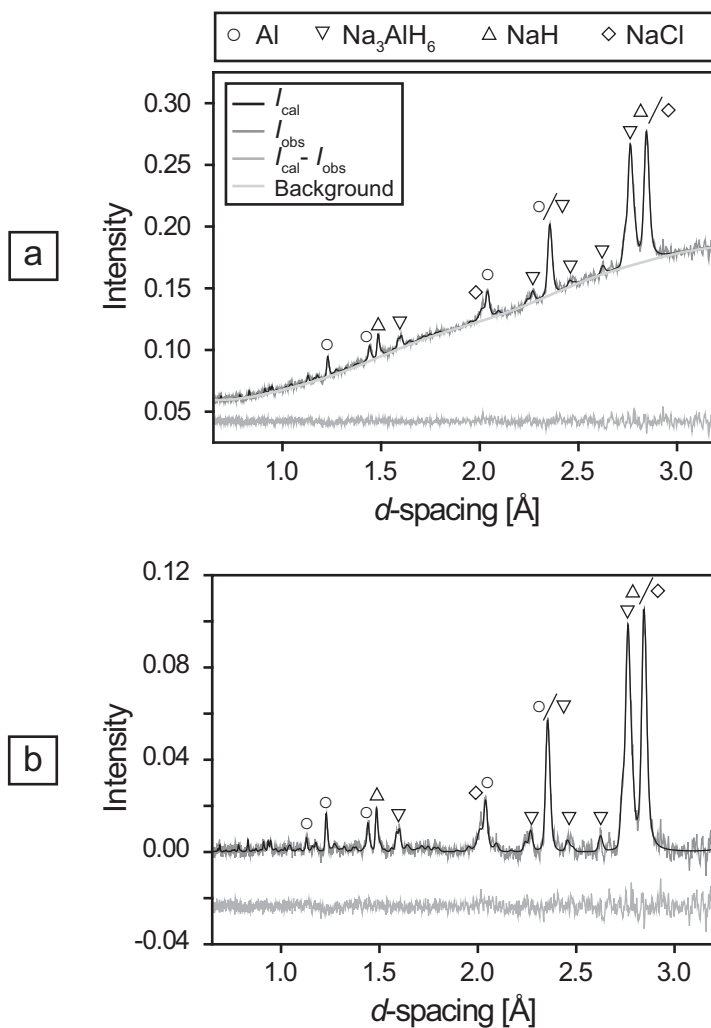


FIGURE A.1 – (a) A fitted diffraction pattern with background showing the onset of NaH formation together with NaCl upon heating the Na₃AlH₆ to 150 °C; (b) The pattern after subtraction of the background.

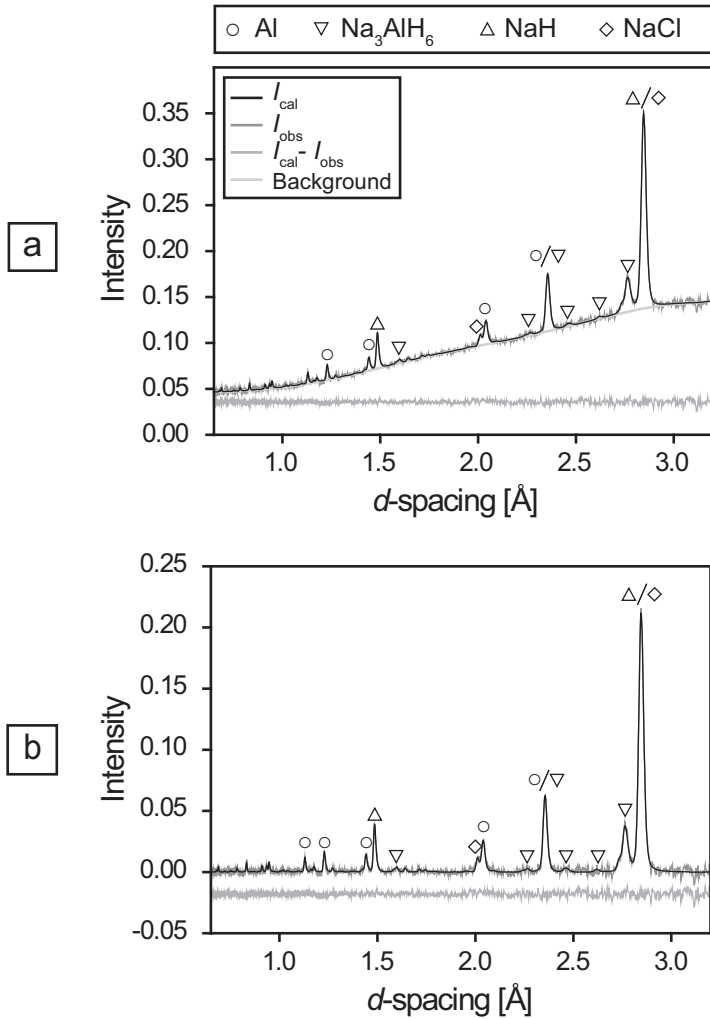


FIGURE A.2 – (a) A fitted diffraction pattern with background showing that Na₃AlH₆ completely transforms into NaH and Al at 150 °C; (b) The pattern after subtraction of the background.

B

TiF₃ catalyzed MgD₂: Fitted patterns

A few selected fitted neutron diffraction patterns from the TiF₃-catalyzed MgD₂ are presented in Figures B.1 and B.2. Figure B.1(a) is taken from interval A, just before the beginning of D₂ first step of the first loading sequence at 150 °C. After 200 min, Mg was transformed into MgD₂ while loading at 150 °C, leaving a very small amount of residual Mg (see Figure B.1(b)). A small background due to hydrogen present in the form TiH_x can be seen in the Figure B.1. Heating up to 320 °C resulted into the removal of this hydrogen and the absorbed deuterium (see Figure B.2(a)). Subsequently, a number of D₂ loading steps in the temperature range of 50 °C—150 °C resulted into the formation of MgD₂, with some residual of Mg (see Figure B.2(b)).

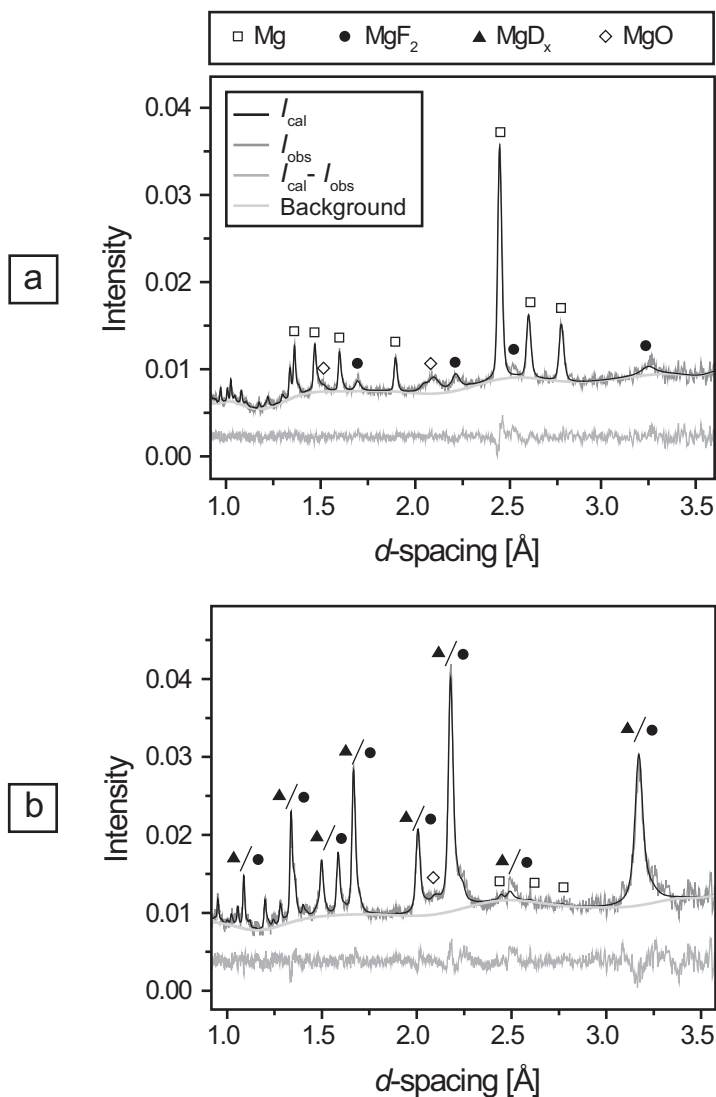


FIGURE B.1 – (a) A fitted diffraction pattern showing Mg, MgO, and MgF₂ at 150 °C before the first step of first load sequence; (b) After 200 min, several steps of D₂ loading resulted into the formation of MgD₂. Besides, MgD₂, MgO, MgF₂, and a small residual of Mg at 150 °C at the last step of first load sequence. A small background due to hydrogen can be seen, which is present in the form TiH_x.

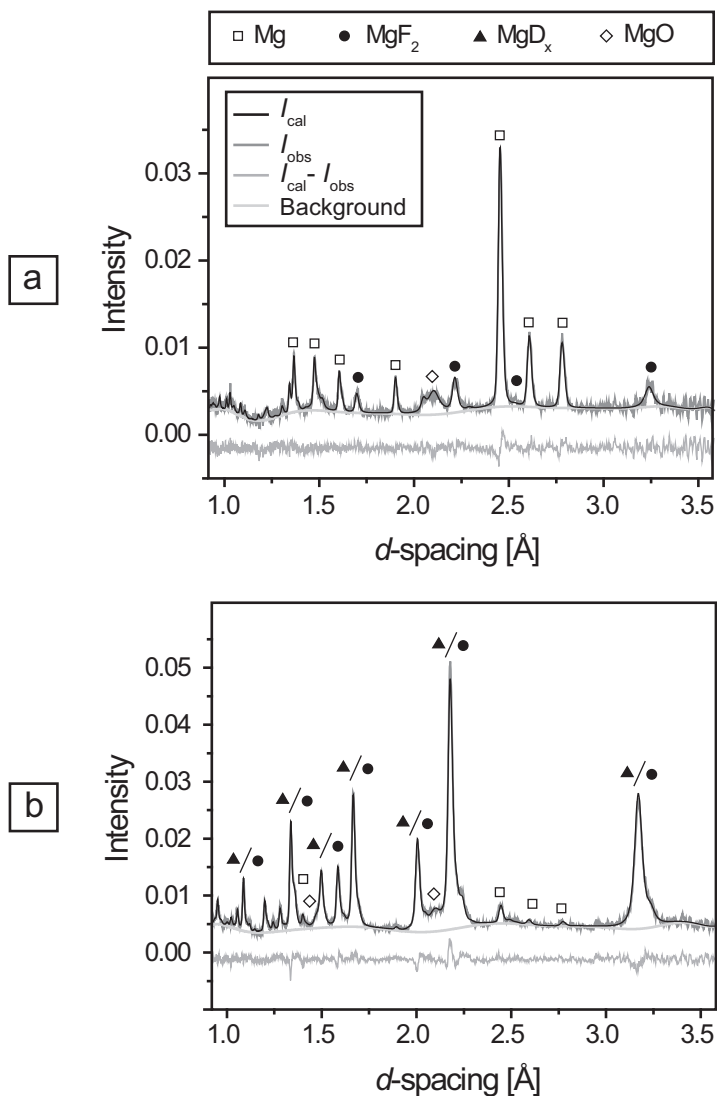


FIGURE B.2 – (a) After desorption at 320 °C, both hydrogen and deuterium were away from $\text{Mg}(\text{H},\text{D})_2$ or $\text{Ti}(\text{H},\text{D})_x$; (b) A diffraction pattern showing the complete transformation of Mg into MgD_2 at 150 °C after a number sequence of loading steps in the temperature range of 50—150 °C. Besides, MgD_2 , some residual Mg, MgO, and MgF_2 is present at the last step of second load sequence at 150 °C.

Summary

HYDROGEN STORAGE IN NANOSTRUCTURED LIGHT METAL HYDRIDES S. SINGH

his thesis presents studies on the role of catalysts as a grain refining agent, and as a hydrogen vacancy formation facilitator, besides its more commonly recognized activity as a hydrogen molecule splitter for hydrogen storage in metals. The grain refining agent, resulting from the catalyst (additive), keeps the crystallites to nanoscale (<150 nm), and reduces the diffusion distance in this way, which is needed for practical reversibility of hydrogenation reactions. It is shown that these nano-crystallites contain abundant hydrogen vacancies, which facilitate the hydrogen reaction kinetics by reducing the migration energy. Furthermore, solid state transformations in Si destabilized MgH_2 are presented. In particular, MgH_2 and NaAlH_4 were considered to be the model systems, as they are promising future hydrogen storage media. Therein, advanced analysis methods such as X-ray diffraction, neutron diffraction, electron microscopy, and positron depth profiling were applied. The latter may provide an insight into the electronic structure changes of metal hydride thin films used as hydrogen switchable mirrors and hydrogen sensors. Moreover, ab initio calculations based on DFT using VASP were also performed.

Pd-capped Mg films

Chapter 3 presents results on the structural transformation and the role of the Pd catalyst on the sorption temperatures and kinetics during hydrogen cycling in Pd-capped Mg thin films. The films grow in columns and clear interfaces with the substrate and Pd cap layer are present. Besides the expected phase transformation of hcp-Mg to rutile-MgH₂, Mg-Pd and Mg-Si alloying was observed at the Pd-Mg and Mg-Si interfaces. A martensitic like phase transformation from Mg to MgH₂ occurs with an orientation relationship of Mg (0002) || MgH₂ (110). The alloying occurs for temperatures above 200 °C, which may possibly affect the hydrogenation processes. The hydrogen sorption studies show that the Mg can be loaded up to 4 wt.% already at 200 °C for applied pressure of 2.5 bar for 2 h, and the full capacity of 7.6 wt.% can be reached with the application of 10 bar pressure for 24 h at this low temperature. Additionally, the delamination of the Pd cap layer at temperatures higher than 250 °C was observed, resulting into a significant decrease in the storage capacity. Positron depth profiling was used to reveal the delamination of ultrathin Pd-cap layers. The permeation studies showed that the hydrogen transport kinetics is rate limited by the hydrogen dissociation at the sample surface, indicating that the Pd catalyst acts as a H₂ splitter at the surface. The impact of the presence of a Pd cap-layer on the hydrogen sorption kinetics and temperatures of uptake and release is much higher than that of the nano-columnar grain structure.

TiCl₃ catalyzed NaAlH₄

Chapter 4 presents in situ neutron diffraction studies on protonated uncatalyzed and TiCl₃-catalyzed NaAlH₄. In particular, the evolution of grain sizes and the hydrogen occupancy throughout the phase transformations upon hydrogen release and deuterium reloading were studied. Clear differences in the crystallite sizes of the occurring phases, hydrogen occupancy, and reversibility behavior in the catalyzed and uncatalyzed NaAlH₄ were reported. After the ball milling, the crystallite sizes for catalyzed and uncatalyzed NaAlH₄ were the same, i.e., approximately

110 nm. However, uncatalyzed NaAlH_4 showed growth in the crystallites, to sizes $\geq 1 \mu\text{m}$, for all occurring phases during the desorption, making it irreversible for deuterium loading. On the other hand, the catalyzed NaAlH_4 showed the presence of nano-crystallites of NaH and Al with sizes of approximately 120 nm, which were maintained during the unloading and loading cycling. The maintenance of small crystallite sizes is caused by grain refinement, induced by the formed TiAl_x and NaCl compounds, acting as nucleation centers for Al and NaH, respectively. Moreover, the nanostructured NaH and Na_3AlH_6 phases showed the presence of abundant hydrogen vacancies, which leads to H-D exchange in nano-NaH at a relatively low temperature of about 150°C , while no vacancies were observed in such type of phases of uncatalyzed NaAlH_4 .

Ab initio calculations on NaH

The DFT based ab initio calculations clearly show that the presence of hydrogen vacancies significantly affects the hydrogen migration energy in NaH, resulting in faster diffusion, and enabling H-D exchange in nano-NaH as observed upon decomposition of ball-milled TiCl_3 -doped NaAlH_4 , as shown in Chapter 5. The estimated rate of the vacancy-mediated hydrogen transport based on diffusion theory is consistent with observed H-D exchange reaction rates. Further, the formation energies for various hydrogen defects, vacancies H_V and interstitials H_I , in the NaH lattice were obtained in all possible charged states (+1, 0, -1). The formation energies for intrinsic hydrogen vacancy-interstitial pairs are too high to explain the observed high hydrogen vacancy concentrations. In order to clarify the large amount of hydrogen vacancies in nano-NaH observed experimentally in the TiCl_3 -doped NaAlH_4 upon hydrogen cycling, a model on the interface of NaH with NaCl, the latter acting as a nucleation center, was evaluated. The calculated interface energies fcc-Na-NaCl and NaH-fcc-Na (001) are low, suggesting a mechanism to induce abundant hydrogen vacancies by promoting the growth of an fcc-Na interlayer between NaH crystallites and the NaCl nucleation centers. This model further assists the idea of the role of NaCl as grain refiner for NaH.

Si destabilized MgH₂

The Si destabilized MgH₂ system was chosen to further investigate the grain refining action by studying the evolution of crystallite sizes and their effect during the hydrogenation of Mg₂Si (see Chapter 6). Using Nb₂O₅ as an additive, the reaction products of Nb and/or MgO were anticipated to act as possible grain refiner for Mg₂Si. The detailed study on the size evolution showed that very small grain sizes of MgH₂ of approximately 10 nm can be achieved in only 30 min of milling in the presence of Si, which also consists of nano-dimension crystallites, i.e., 100 nm. Nano-Mg₂Si (80 nm) was obtained upon desorption in the temperature range of 25–300 °C of the Nb₂O₅-catalyzed MgH₂-Si mixture. Despite of the nano-dimensions of the crystallites, the Mg₂Si could not be loaded with hydrogen successfully.

Mg-Si bilayer thin films capped with Pd were studied as an aid to clarify the (lack of) reactivity and to gain an insight into the local transformations associated with the solid state reactions. A well-defined interface between different layers was present in such types of thin films with typical thicknesses of up to 1 μm. Similarly deposited films were heated up to 207 °C under 10 bar of helium and a hydrogen atmosphere for 24 h to study the reaction path for Mg₂Si formation. The study shows that the Mg₂Si formation is faster than that of MgH₂ formation. Re-hydrogenation of Mg₂Si is difficult, most likely related to the presence of a barrier against removal of Mg from the Mg₂Si layer, inhibiting the formation of MgH₂.

TiF₃-catalyzed MgH₂

In situ neutron diffraction studies on TiF₃-catalyzed MgH₂ are presented in the Chapter 7. The structural transformation together with the evolution of crystallite sizes and the deuterium occupancy in the MgD₂ upon deuterium loading and unloading were studied. The study shows that MgF₂ was formed during the first hydrogen release. The TiF₃-catalyzed MgD₂ was successfully loaded at a temperature as low as 50 °C; however, the hydrogen release was very slow at this temperature. The rate of deuterium release was increased by a factor of five at 320 °C. The crystallite

sizes of MgD_2 were found to be small (average crystallite size roughly 30 nm) during the deuterium loading and unloading. The restricted growth of MgD_2 throughout the deuterium cycle suggests that MgF_2 indeed acts as grain refiner for MgD_2 grains. Moreover, nano-crystallites of MgD_2 shows the presence of approximately 30% of deuterium vacancies in the beginning of the loading, which became almost fully occupied upon full loading. Subsequent, desorption at higher temperatures again leads to an increase in the deuterium vacancy concentration which rises to 15%.

In this thesis it is reported that catalysts can provide an additional role as a grain refiner besides playing an important role in the hydrogen release and uptake by splitting the hydrogen molecule bond. Grain refinement seems to work for several examples, while it does not solve the reversibility issue for Si-destabilized MgH_2 . It greatly improves reversibility at favorable hydrogen cycling conditions for the NaAlH_4 and MgH_2 systems. Furthermore, these nano-crystallites (<150 nm) show abundant hydrogen vacancy concentrations during hydrogen loading and unloading. These vacancies lead to an enhancement in the reaction kinetics during hydrogen cycling by reducing the migration energy.

Samenvatting

HYDROGEN STORAGE IN NANOSTRUCTURED LIGHT METAL HYDRIDES

S. SINGH

Dit proefschrift beschrijft een studie naar de rol van katalysatoren in de korrelverfijning en in de vorming van waterstofvacatures in opslagmaterialen voor waterstof gebaseerd op metaalhydriden. Deze rol blijkt op te treden naast de algemeen bekende rol van katalysatoren in het splitsen van de waterstofmoleculen. De door de toegevoegde katalysator veroorzaakte korrelverfijning zorgt ervoor dat de korrelgrootte van de kristallieten klein blijft (<150 nm), en vermindert zo de vereiste diffusielengte voor waterstof-en ionentransport, hetgeen nodig is voor de praktische omkeerbaarheid van de waterstofsorptiereacties. In dit proefschrift wordt aangetoond dat de nanokristallieten overvloedige hoeveelheden waterstofvacatures bevatten, die de kinetiek van de waterstofsorptiereacties bevorderen door de vermindering van de migratie energie. Bovendien wordt het verloop gepresenteerd van de vastestoftransformaties in MgH_2 dat door toevoeging van Si is gestabiliseerd. In het bijzonder worden hier MgH_2 en $NaAlH_4$ onderzocht als voorbeeldsystemen, temeer daar zij veelbelovende opslagmedia voor waterstof zijn. In deze studie zijn geavanceerde analysemethoden zoals Röntgendiffractie, neutronendiffractie, elektronenmicroscopie en positronen diepteprofilering toegepast. Deze laatste methode kan een inzicht geven in de veranderingen in de elektronische structuur van dunne lagen metaalhydriden, die een toepassing vinden in waterstof schakelbare

spiegels en waterstofsensoren. Daarnaast zijn ab initio berekeningen, gebaseerd op DFT, met behulp van de VASP code uitgevoerd.

Mg dunne lagen met een Pd katalysator toplaag

Hoofdstuk 3 behandelt onderzoek naar de structurele transformaties van Mg dunne lagen met een Pd toplaag en de invloed van Pd als katalysator op de temperaturen en kinetiek van het beladen met waterstof en het ontladen. De lagen groeien in de vorm van kolommen, en er is een scherp grensvlak met het substraat en de Pd toplaag aanwezig. Naast de bekende fase-transformatie van hcp-Mg naar rutiel-MgH₂ is de vorming van Mg-Pd en Mg-Si legeringen waargenomen bij de Pd-Mg en Mg-Si grensvlakken. Een martensitische fase-transformatie van Mg naar MgH₂ treedt op met de oriëntatierelatie Mg (0002) || MgH₂ (110). Voor temperaturen boven de 200 °C worden in de lagen legeringen gevormd, die mogelijk van invloed zijn op de waterstofbeladingsprocessen. De waterstofsorptiestudies tonen aan dat het Mg al bij 200 °C en een waterstofdruk van 2.5 bar gedurende 2 uur beladen kan worden tot 4 wt.%, en dat de volledige capaciteit van 7.6 wt.% bij deze lage temperatuur wordt bereikt bij gebruik van 10 bar waterstofdruk gedurende 24 uur. Daarnaast is delaminatie van de Pd toplaag waargenomen bij temperaturen hoger dan 250 °C, wat resulteert in een grote afname van de opslagcapaciteit. Positronen diepteprofilering is gebruikt om de delaminatie van ultradunne Pd toplagen aan te tonen. Uit de permeatiestudies is gebleken dat dissociatie van waterstofmoleculen aan het oppervlak van de dunnelaagmaterialen de snelheidsbepalende factor is in de waterstofkinetiek, wat aantoont dat de Pd katalysator fungeert als een splitter van H₂ moleculen aan het oppervlak. Het effect van de aanwezigheid van een Pd afdeklaag op de waterstofsorptiekinetiek en de temperaturen van opname en afgifte van waterstof is veel groter dan die van de kolomvormige korrelstructuur.

NaAlH₄ gekatalyseerd met TiCl₃

Hoofdstuk 4 beschrijft in-situ neutronen diffractiestudies aan geprotoneerd ongekatalyseerd en TiCl₃-gekatalyseerd NaAlH₄. In het bijzonder is de

ontwikkeling van de korrelgrootten en de waterstofbezetting tijdens de fasetransformaties behorend bij waterstofontlading en het opnieuw beladen met deuterium bestudeerd. Duidelijke verschillen zijn gevonden in de deeltjesgrootten van de optredende fasen, in de waterstofbezetting, en in de omkeerbaarheid van de reacties voor het gekatalyseerde en ongekatalyseerde NaAlH_4 . De deeltjesgrootten van de kristallieten zijn direct na de preparatie met behulp van kogelmalen hetzelfde voor gekatalyseerd en ongekatalyseerd NaAlH_4 , ongeveer 110 nm. Het ongekatalyseerde NaAlH_4 vertoonde echter een groei in de afmeting van de kristallieten tot voorbij 1 μm voor alle kristalfasen tijdens de desorptie, waardoor een herbelading met deuterium niet meer mogelijk bleek. Voor het gekatalyseerde NaAlH_4 bleek de desorptie echter te leiden tot het ontstaan van NaH en Al nanokristallieten met afmetingen van ongeveer 120 nm. Deze deeltjesgrootten bleven behouden tijdens de afgifte van waterstof en opname van deuterium. De behouden kleine deeltjesgrootten worden veroorzaakt door de korrelverfijning door de gevormde TiAl_x en NaCl verbindingen, die als nucleatiecentra voor respectievelijk het Al en het NaH optreden. Daarnaast zijn grote concentraties waterstofvacatures waargenomen in de gevormde nanogestructureerde NaH en Na_3AlH_6 fasen, wat leidt tot uitwisseling van waterstof en deuterium in de NaH nanokristallieten bij een relatief lage temperatuur van ongeveer 150 °C, terwijl er geen waterstofvacatures waargenomen zijn in deze fasen voor het ongekatalyseerde NaAlH_4 .

Ab initio berekeningen aan NaH

Uit de ab initio berekeningen gebaseerd op DFT, zoals weergegeven in hoofdstuk 5, blijkt duidelijk dat de aanwezigheid van waterstofvacatures de migratie energie van waterstof in NaH zeer sterk beïnvloedt, waardoor diffusie ontstaat en de uitwisseling van waterstof en deuterium voor het nano-NaH mogelijk wordt, zoals waargenomen tijdens de decompositie van het met kogelmalen geprepareerde NaAlH_4 gekatalyseerd met TiCl_3 . De op basis van diffusietheorie geschatte snelheid van het transport van waterstof via waterstofvacatures is in overeenstemming met de waargenomen snelheid van de uitwisseling van waterstof en deu-

terium. Verder is de vormingsenergie van diverse waterstofdefecten in het NaH kristalrooster, namelijk waterstofvacatures H_V en interstitiële waterstofatomen H_I , verkregen in alle mogelijke ladingstoestanden (dus $+1,0,-1$). De vormingsenergieën voor de intrinsieke waterstof vacature-interstitiële paren zijn te hoog om de waargenomen hoge concentraties waterstofvacatures te kunnen verklaren. Ten einde inzicht te krijgen in de grote hoeveelheid waterstofvacatures in nano-NaH, zoals experimenteel is waargenomen in het $TiCl_3$ -gedoopte $NaAlH_4$ tijdens waterstof ontladen en beladen, is een model geëvalueerd waarin het grensvlak van NaH met NaCl werd beschouwd. De NaCl kristallieten treden hierbij op als nucleatiecentra. De berekende grensvlakenergieën voor de fcc-Na || NaCl en NaH || fcc-Na (001) grensvlakken zijn laag. Een mogelijk mechanisme voor het opwekken van grote concentraties waterstofvacatures is hierdoor gevonden, waarin de groei van een kubisch vlakgecentreerde natrium (fcc-Na) tussenlaag tussen de NaCl nucleatiecentra en de NaH kristallieten centraal staat. Dit model onderbouwt tevens de voorgestelde rol van NaCl als korrelverfijner voor NaH.

MgH₂ gedestabiliseerd door Si

Het systeem MgH₂ gedestabiliseerd door Si is gekozen voor verder onderzoek naar de relatie tussen korrelverfijning en de ontwikkeling van deeltjesgrootten, en ten einde de gevolgen daarvan voor waterstofbelading van Mg₂Si te onderzoeken (zie hoofdstuk 6). Voor de katalysator Nb₂O₅ is de verwachting dat de reactieproducten Nb en/of MgO kunnen optreden als mogelijke korrelverfijners voor Mg₂Si. Uit de gedetailleerde studie naar de ontwikkeling van deeltjesgrootten is gebleken dat een zeer kleine korrelgrootte voor het MgH₂ van ongeveer 10 nm kan worden bereikt in slechts 30 min kogelmalen in aanwezigheid van Si poeder. De Si kristallieten bereiken ook kleine afmetingen, namelijk ongeveer 100 nm. Nano-Mg₂Si (80 nm) ontstaat tijdens waterstofdesorptie van het Nb₂O₅-gekatalyseerde MgH₂-Si systeem in het temperatuurgebied van 25—300 °C. Ondanks de nanoschaal afmetingen van de kristallieten bleek het Mg₂Si echter niet te kunnen worden herbeladen met waterstof. Mg-Si dubbellenen met een Pd toplaag zijn bestudeerd om verder inzicht te krij-

gen in de (afwezigheid van) reactiviteit en in de lokale transformaties ten gevolge van de vastestofreacties. Een goed gedefinieerd grensvlak tussen de verschillende lagen is aanwezig in dergelijke dunnelaagsystemen die typisch van de orde van $1\ \mu\text{m}$ dik zijn. De dunnelaagsystemen werden verhit tot $207\ \text{°C}$ gedurende 24 uur onder een 10 bar helium of waterstof atmosfeer ten einde het reactiepad voor de vorming van Mg_2Si te kunnen bestuderen. De studie toont aan dat de vorming van Mg_2Si sneller is dan de vorming van MgH_2 . Herbeladen van Mg_2Si is moeilijk, waarschijnlijk vanwege de aanwezigheid van een barrière tegen verwijdering van Mg uit de Mg_2Si laag, waardoor de vorming van MgH_2 wordt verhinderd.

MgH_2 gekatalyseerd met TiF_3

In-situ neutronen diffractiestudies aan MgH_2 gekatalyseerd met TiF_3 worden beschreven in hoofdstuk 7. De structurele transformaties samen met de ontwikkeling van de deeltjesgrootten en de deuteriumbezetting in het MgD_2 werden bestudeerd tijdens het ontladen en het beladen met deuterium. De studie toont aan dat MgF_2 werd gevormd tijdens de eerste waterstofontlading. Het met TiF_3 gekatalyseerde MgD_2 kon met succes worden herbeladen bij een nogal lage temperatuur van $50\ \text{°C}$, maar de desorptie van het deuterium is traag bij deze temperatuur. De snelheid van deuteriumontlading is vijf keer zo snel bij $320\ \text{°C}$. De deeltjesgrootten van het MgD_2 bleken klein te zijn (gemiddeld ongeveer $30\ \text{nm}$) en te blijven tijdens het ontladen en het herbeladen met deuterium. De beperkte groei van MgD_2 gedurende de gehele deuteriumbeladingscyclus suggereert dat MgF_2 inderdaad fungeert als korrelverfijner voor de MgD_2 deeltjes. Daarnaast is waargenomen dat de MgD_2 nanokristallieten ongeveer 30% deuteriumvacatures bevatten tijdens de beginfase van het beladen, waarna de deuteriumposities bijna volledig bezet werden nabij de volledig beladen toestand van het materiaal. De daaropvolgende ont-lading bij hogere temperaturen leidde tot een hernieuwde toename van de concentratie deuteriumvacatures tot 15%.

In dit proefschrift wordt beschreven dat katalysatoren een belangrijke aanvullende rol kunnen vervullen als korrelverfijner, naast de rol die zij spelen bij de opname en afgifte van waterstof door het splitsen van waterstofmoleculen. Het mechanisme van korrelverfijning lijkt te werken voor verscheidene voorbeelden, terwijl dit niet de oplossing blijkt te zijn om reversibiliteit te bereiken in het Si-gedestabiliseerde MgH_2 systeem. Het verbetert voor NaAlH_4 en MgH_2 gekatalyseerd met respectievelijk TiCl_3 en TiF_3 de omkeerbaarheid aanzienlijk en leidt tot gunstige omstandigheden van waterstofbelading en ontlading. Bovendien blijken de nanokristallieten (<150 nm) voor deze systemen grote concentraties waterstofvacatures te bevatten tijdens het beladen en ontladen. Deze vacatures leiden tot een verbetering in de kinetiek tijdens het cycleren met waterstof door de sterke vermindering van de migratie energie.

Bibliography

- [1] H. Cavendish. Experiments on factitious air. *Phil. Trans. R. Soc. Lon.*, 56, 1766. {2}
- [2] H. Hartley. Antoine Laurent Lavoisier. *Proc. Roy. Soc. London A*, 189(1019), 1947. {2}
- [3] P. Hoffmann. *Tomorrow's energy: Hydrogen, fuel cells, and prospects for a cleaner planet*. The MIT Press, Cambridge, Massachusetts, London, England, 2002. {2–5}
- [4] The National Hydrogen Association. <http://www.hydrogenassociation.org/general/factSheets.asp>, 2009. {2, 3, 5}
- [5] C. Russell. <http://www.rsc.org/chemistryworld/Issues/2003/August/electrolysis.asp>, August 2003. Royal Society of Chemistry. {2}
- [6] W.R. Grove. On the gas voltaic battery. Experiments made with a view of ascertaining the rationale of its action and its application to eudiometry. *Phil. Trans. R. Soc. Lon.*, 133, 1947. {2}
- [7] J.B.S. Haldane. *Daedalus or science and future; A paper read to the heretics*. Cambridge, 1923. {2}
- [8] A.J. Dessler. The Hindenburg hydrogen fire: Fatal flaws in the addison bain incendiary-paint theory. Technical report, Lunar and Planetary Laboratory, University of Arizona, 2004. {3}
- [9] A.J. Dessler, D.E. Overs, and W.H. Appleby. The Hindenburg fire: Hydrogen or incendiary paint? *Buoyant Flight*, 52, 2005. {3}
- [10] K.R. Williams. Francis Thomas Bacon. *Biogr. Mem. Fell. R. Soc.*, 39, 1994. {3}
- [11] Fuel Cell Test and Evaluation Center (FCTec). Fuel cell basics, 2001—2009. http://www.fctec.com/fctec_history.asp. {4}

- [12] R. Billings. <http://rogerbillings.info/index.html>, 2008. {4}
- [13] EIA/IEO. International energy outlook May 2007. Technical Report DOE/EIA-0484, EIA, 2007. {5, 6}
- [14] L. Schlapbach and A. Züttel. Hydrogen-storage materials for mobile applications. *Nature*, 414:353, 2001. {6, 73, 113}
- [15] A. Züttel. Materials for hydrogen storage. *Mater. Today*, 6:24, 2003. {7, 8}
- [16] G. Barkhordarian, T. Klassen, and R. Bormann. Fast hydrogen sorption kinetics of nanocrystalline Mg using Nb₂O₅ as catalyst. *Scripta Mater.*, 49:213, 2003. {7}
- [17] G. Barkhordarian, T. Klassen, and R. Bormann. Effect of Nb₂O₅ content on hydrogen reaction kinetics of Mg. *J. Alloy. Compd.*, 364:242, 2004. {7}
- [18] N. Hanada, T. Ichikawa, S. Hino, and H. Fujii. Remarkable improvement of hydrogen sorption kinetics in magnesium catalyzed with Nb₂O₅. *J. Alloy. Compd.*, 420:46, 2006. {7}
- [19] W. Oelerich, T. Klassen, and R. Bormann. Metal oxides as catalysts for improved hydrogen sorption in nanocrystalline Mg-based materials. *J. Alloy. Compd.*, 315:237, 2001. {7}
- [20] H.G. Schimmel, J. Huot, L.C. Chapon, F.D. Tichelaar, and F.M. Mulder. Hydrogen cycling of niobium and vanadium catalyzed nanostructured magnesium. *J. Am. Chem. Soc.*, 127:14348, 2005. {7, 9, 11, 86, 88, 97, 114, 129, 130, 137, 138, 140}
- [21] Z. Dehouche, R. Djaozandry, J. Huot, S. Boily, J. Goyette, T.K. Bose, and R. Schulz. Influence of cycling on the thermodynamic and structure properties of nanocrystalline magnesium based hydride. *J. Alloy. Compd.*, 305:264, 2000. {7}
- [22] B. Bogdanović, R.A. Brand, A. Marjanović, M. Schwickardi, and J.Tolle. Metal-doped sodium aluminium hydrides as potential new hydrogen storage materials. *J. Alloy. Compd.*, 302:36, 2000. {8, 73}
- [23] B. Bogdanović and M. Schwickardi. Ti-doped alkali metal aluminium hydrides as potential novel reversible hydrogen storage materials. *J. Alloy. Compd.*, 253-254:1, 1997. {8, 73, 98}
- [24] J.J. Vajo, F. Mertens, C.C. Ahn, R.C. Bowman Jr., and B. Fultz. Altering hydrogen storage properties by hydride destabilization through alloy formation: LiH and MgH₂ destabilized with Si. *J. Phys. Chem. B*, 108:13977, 2004. {9, 70, 113}

- [25] O. Friedrichs, T. Klassen, J.C. Sánchez-López, R. Bormann, and A. Fernández. MgH₂ with Nb₂O₅ as additive, for hydrogen storage: Chemical, structural and kinetic behavior with heating. *Acta Mater.*, 54:105, 2006. {9, 114, 129}
- [26] N. Iqbal, N.H. van Dijk, T. Hansen, L. Katgerman, and G.J. Kearley. The role of solute titanium and TiB₂ particles in the liquid-solid phase transformation of aluminum alloys. *Mater. Sci. Eng. A-Struct.*, 386:20, 2004. {10, 89}
- [27] N. Iqbal, N.H. van Dijk, S.E. Offerman, M.P. Moret, L. Katgerman, and G.J. Kearley. Real-time observation of grain nucleation and growth during solidification of aluminium alloys. *Acta Mater.*, 53:2875, 2005. {10, 89}
- [28] M. Wagemaker, W.J.H. Borghols, and F.M. Mulder. Large impact of particle size on insertion reactions. A case for anatase Li_xTiO₂. *J. Am. Chem. Soc.*, 129:4323, 2007. {11, 88, 97}
- [29] Fritsch GmbH. *Operating Instructions: Planetary Mono Mill "Pulverisette 6"*, 2005. <http://www.fritsch.de>. {16}
- [30] M.W. Zandbergen. Nano-structured Mg and LiAl films for hydrogen storage. Master's thesis, Delft University of Technology, March 2004. {18, 50, 54}
- [31] R. Kind. Depth sensitive analysis of Si-destablized MgH₂ thin films upon reversible H₂-sorption. Technical report, Delft University of Technology, July 2008. Bachelor's thesis. {18}
- [32] M. Ohring. *Materials Science of Thin Films*. Academic Press, San Diego, 2002. {19, 20}
- [33] P. Mosaner, N. Bazzanella, M. Bonelli, R. Checchetto, and A. Miotello. Mg:Nb films produced by pulsed laser deposition for hydrogen storage. *Mater. Sci. Eng. B*, 108:33, 2004. {19, 67}
- [34] J. Paillier and L. Roue. Hydrogen electrosorption and structural properties of nanostructured Pd-Mg thin films elaborated by pulsed laser deposition. *J. Alloy. Compd.*, 404—406:473, 2005. {19}
- [35] A.C. Larson and R.B.V. Dreele. *General Structure Analysis System (GSAS)*, 2000. {22, 36, 39, 76}
- [36] S.W. Lovesey. *Theory of neutron scattering from condensed matter; nuclear scattering*, volume 1. Oxford University Press, New York, 1984. {33}

- [37] G.L. Squires. *Introduction to the theory of thermal neutron Scattering*. Cambridge University Press: Cambridge London New York Melbourne, 1978. {33}
- [38] W.G. Williams, R.M. Ibberson, P. Day, and J.E. Enderby. GEM—general materials diffractometer at ISIS. *Physica B*, 241—243:234, 1998. {34, 76}
- [39] ISIS. <http://www.isis.rl.ac.uk/>. {34–36}
- [40] W. Kohn and L.J. Sham. Self-consistent equations including exchange and correlation effects. *Phys. Rev.*, 140:A1133, 1965. {39–41, 98}
- [41] P. Hohenberg and W. Kohn. Inhomogeneous electron gas. *Phys. Rev.*, 136:B864, 1964. {39, 40, 98}
- [42] M. Born and R. Oppenheimer. Zur Quantentheorie der Molekeln. *Ann. Phys.*, 84:457, 1927. {39}
- [43] P. Ziesche, S. Kurth, and J.P. Perdew. Density functionals from LDA to GGA. *Comp. Mater. Sci.*, 11:122, 1998. {41}
- [44] G. Kresse and J. Furthmüller. *Vienna Ab-initio Simulation Package*. Institut für Materialphysik, Universität Wien, Sensengasse 8, A-1130 Wien, Austria, August 2005. <http://cms.mpi.univie.ac.at/vasp/>. {41–43, 98}
- [45] R.M. Nieminen. *Chapter 4: The fate of slow positrons in condensed matter*. World Scientific Singapore New Jersey London Hong Kong, 1999. {44}
- [46] Positron Beam Laboratory. <http://www.uwo.ca/isw/facilities/Positron/analysis.htm>. {44}
- [47] A. Rivera. *Hydrogen interactions with silicon-on-insulator materials*. PhD thesis, Delft University of Technology, 2002. {45}
- [48] P. Coleman, editor. *Positron beams and their applications*. World Scientific Singapore New Jersey London Hong Kong, 1999. {46}
- [49] P.J. Schultz and K.G. Lynn. Interaction of positron beams with surfaces, thin films, and interfaces. *Rev. Mod. Phys.*, 108:33, 1988. {46}
- [50] K. Higuchi, H. Kajioka, K. Toiyama, H. Fujii, S. Orimo, and Y. Kikuchi. In situ study of hydriding-dehydriding properties in some Pd/Mg thin films with different degree of Mg crystallization. *J. Alloy. Compd.*, 293—295:484, 1999. {49}
- [51] K. Higuchi, K. Yamamoto, H. Kajioka, K. Toiyama, M. Honda, S. Orimo, and H. Fujii. Remarkable hydrogen storage properties in three-layered Pd/Mg/Pd thin films. *J. Alloy. Compd.*, 330—332:526, 2002. {49, 53}

- [52] L. Aballe, C. Rogero, and K. Horn. Quantum size effects in ultrathin epitaxial Mg films on Si (111). *Phys. Rev. B*, 65:125319, 2002. {52}
- [53] K. Saiki, K. Nishita, Y. Ariga, and A. Koma. Growth of Mg films on H-terminated Si (111). *J. Vac. Sci. Technol. A*, 17:2911, 1999. {52}
- [54] H.G. Schimmel, M.R. Johnson, G.J. Kearley, A.J. Ramirez-Cuesta, J. Huot, and F.M. Mulder. The vibrational spectrum of magnesium hydride from inelastic neutron scattering and density functional theory. *Mater. Sci. Eng. B*, 108:38, 2004. {53}
- [55] J. Huot. *Nanocrystalline Materials for Hydrogen Storage in Nanoclusters and Nanocrystals*. American Scientific Publishers, Stevenson Ranch, CA, 2003. Chapter 2, pp.53—85. {54}
- [56] D.R. Lide. *CRC Handbook of Chemistry and Physics*. CRC press, Boca Raton, Florida, 84th edition, 2003—2004. pp.12/219—12/220. {59}
- [57] A. van Veen, H. Schut, J. de Vries, R.A. Hakvoort, and M.R. Ijpma. Analysis of positron profiling data by means of "VEPFIT". In P.J. Schultz, editor, *4th International workshop on: Slow-positron beam techniques for solids and surfaces*, volume 218, page 171. AIP, New York, July 1990. {61, 120}
- [58] Y. Garreau and G. Loupiau. Compton profile of MgH₂. *Solid State Commun.*, 74:583, 1990. {61}
- [59] S.W.H. Eijt, R. Kind, S. Singh, H. Schut, W.J. Legerstee, R.W.A. Hendrikx, V.L. Svetchnikov, R.J. Westerwaal, and B. Dam. Positron depth profiling of the structural and electronic structure transformations of hydrogenated Mg-based thin films. *J. Appl. Phys.*, 105:043514, 2009. {63, 64}
- [60] R. Checchetto, N. Bazzanella, A. Miotello, R.S. Brusa, A. Zecca, and A. Mengucci. Deuterium storage in nanocrystalline magnesium thin films. *J. Appl. Phys.*, 95:1989, 2004. {63}
- [61] S. Hao and D.S. Sholl. Hydrogen diffusion in MgH₂ and NaMgH₃ via concerted motions of charged defects. *Appl. Phys. Lett.*, 93:251901, 2008. {63}
- [62] J.L. Slack, J.C.W. Locke, S.W. Song, J. Ona, and T.J. Richardson. Metal hydride switchable mirrors: Factors influencing dynamic range and stability. *Sol. Energ. Mat. Sol. C.*, 90:485, 2006. {64}
- [63] P.I. Kripyakevich and E.I. Gladyshevskii. *Sov. Phys. Crystallogr.*, 5:552, 1960. {68}

- [64] W. Lohstroh, R.J. Westerwaal, J.L.M. van Mechelen, C. Chacon, E. Johansson, B. Dam, and R. Griessen. Structural and optical properties of Mg_2NiH_x switchable mirrors upon hydrogen loading. *Phys. Rev. B*, 70:165411, 2004. {70}
- [65] W. Lohstroh, R.J. Westerwaal, B. Noheda, S. Enache, I.A.M.E. Giebels, B. Dam, and R. Griessen. Self-organized layered hydrogenation in black Mg_2NiH_x switchable mirrors. *Phys. Rev. Lett.*, 93:197404, 2004. {70}
- [66] W.K. Chu, S.S. Lau, J.W. Mayer, and H. Müller. Implanted noble gas atoms as diffusion markers in silicide formation. *Thin Solid Films*, 25:393, 1975. {70}
- [67] P.L. Janega, J. McCaffrey, D. Landheer, M. Buchanan, M. Denhoff, and D. Mitchel. Contact resistivity of some magnesium/silicon and magnesium silicide/silicon structures. *Appl. Phys. Lett.*, 53:2056, 1988. {70}
- [68] B. Bogdanović, M. Felderhoff, S. Kaskel, A. Pommerin, K. Schlichte, and F. Schüth. Improved hydrogen storage properties of Ti-doped sodium alanate using titanium nanoparticles as doping agents. *Adv. Mater.*, 15:1012, 2003. {73, 98}
- [69] K.J. Gross, S. Guthrie, S. Takara, and G.J. Thomas. In situ X-ray diffraction study of the decomposition of NaAlH_4 . *J. Alloy. Compd.*, 297:297, 2000. {73}
- [70] C.M. Jensen and K.J. Gross. Development of catalytically enhanced sodium aluminum hydride as a hydrogen-storage material. *Appl. Phys. A*, 72:213, 2001. {73}
- [71] G. Sandrock, K.J. Gross, G.J. Thomas, C.M. Jensen, D. Meeker, and S. Takara. Dynamic in situ X-ray diffraction of catalyzed alanates. *J. Alloy. Compd.*, 330:696, 2002. {73}
- [72] K.J. Gross, G.J. Thomas, and C.M. Jensen. Catalyzed alanates for hydrogen storage. *J. Alloy. Compd.*, 330—332:683, 2002. {74}
- [73] T. Kiyobayashi, S.S. Srinivasan, D. Sun, and C.M. Jensen. Kinetic study and determination of the enthalpies of activation of the dehydrogenation of titanium- and zirconium-doped NaAlH_4 and Na_3AlH_6 . *J. Phys. Chem. A*, 107:7671, 2003. {74}
- [74] J. Graetz, J.J. Reilly, J. Johnson, A.Y. Ignatov, and T.A. Tyson. X-ray absorption study of Ti-activated sodium aluminum hydride. *Appl. Phys. Lett.*, 85:500, 2004. {74, 89}

- [75] A. León, O. Kircher, J. Rothe, and M. Fichtner. Chemical state and local structure around titanium atoms in NaAlH₄ doped with TiCl₃ using X-ray absorption spectroscopy. *J. Phys. Chem. B*, 108:16372, 2004. {74}
- [76] J. Iniguez and T. Yildirim. First-principles study of Ti-doped sodium alanate surfaces. *Appl. Phys. Lett.*, 86:103109, 2005. {74}
- [77] D. Sun, T. Kiyobayashi, H.T. Takeshita, N. Kuriyama, and C.M. Jensen. X-ray diffraction studies of titanium and zirconium doped NaAlH₄: Elucidation of doping induced structural changes and their relationship to enhanced hydrogen storage properties. *J. Alloy. Compd.*, 337:L8, 2002. {74}
- [78] G.J. Thomas, K.J. Gross, N.Y.C. Yang, and C. Jensen. Microstructural characterization of catalyzed NaAlH₄. *J. Alloy. Compd.*, 330-332:702, 2002. {74}
- [79] O. Palumbo, A. Paolone, R. Cantelli, C.M. Jensen, and M. Sulic. Fast H-vacancy dynamics during alanate decomposition by anelastic spectroscopy. proposition of a model for Ti-enhanced hydrogen transport. *J. Phys. Chem. B*, 110:9105, 2006. {74, 88, 97}
- [80] A. Peles and C.G. van de Walle. Hydrogen-related defects in sodium alanate. *J. Alloy. Compd.*, 446-447:459, 2007. {74, 88, 98}
- [81] A. Peles and C.G. van de Walle. Role of charged defects and impurities in kinetics of hydrogen storage materials: A first-principles study. *Phys. Rev. B*, 76:214101, 2007. {74, 97}
- [82] S. Singh, S.W.H. Eijt, J. Huot, W.A. Kockelmann, M. Wagemaker, and F.M. Mulder. The TiCl₃ catalyst in NaAlH₄ for hydrogen storage induces grain refinement and impacts on hydrogen vacancy formation. *Acta Mater.*, 55:5549, 2007. {75, 97, 100, 104, 108, 110, 114, 129, 140}
- [83] G. Blake. Sequentz program for sequential refinement using GSAS. Annual report, ISIS facility, 2004. {76}
- [84] B. Bogdanović and B. Spliethoff. Active MgH₂-Mg-systems for hydrogen storage. *Int. J. Hydrogen Energ.*, 12:863, 1987. {85, 140}
- [85] K.J. Gross, P. Spatz, A. Züettel, and L. Schlapbach. Mechanically milled Mg composites for hydrogen storage—the transition to a steady state composition. *J. Alloy. Compd.*, 240:206, 1996. {85, 140}
- [86] J. Huot, G. Liang, S. Boily, A. van Neste, and R. Schulz. Structural study and hydrogen sorption kinetics of ball-milled magnesium hydride. *J. Alloy. Compd.*, 293-295:495, 1999. {85}

- [87] C.P. Baldé, B.P.C. Hereijgers, J.H. Bitter, and K.P. de Jong. Facilitated hydrogen storage in NaAlH₄ supported on carbon nanofibers. *Angew. Chem. Int. Edit.*, 45:3501, 2006. {85, 140}
- [88] C.M. Araújo, S. Li, R. Ahuja, and P. Jena. Vacancy-mediated hydrogen desorption in NaAlH₄. *Phys. Rev. B*, 72:165101, 2005. {86}
- [89] S. Li, P. Jena, and R. Ahuja. Effect of Ti and metal vacancies on the electronic structure, stability, and dehydrogenation of Na₃AlH₆: Supercell band-structure formalism and gradient-corrected density-functional theory. *Phys. Rev. B*, 73:214107, 2006. {86}
- [90] C. Weidenthaler, A. Pommerin, M. Felderhoff, B. Bogdanović, and F. Schüth. On the state of the titanium and zirconium in Ti- or Zr-doped NaAlH₄ hydrogen storage material. *Phys. Chem. Chem. Phys.*, 5:5149, 2003. {89}
- [91] A.B. Belonoshko, N.V. Skorodumova, A. Rosengren, and B. Johansson. Melting and critical superheating. *Phys. Rev. B*, 73:012201, 2006. {89}
- [92] H.W. Brinks, C.M. Jensen, S.S. Srinivasan, B.C. Hauback, D. Blanchard, and K. Murphy. Synchrotron X-ray and neutron diffraction studies of NaAlH₄ containing Ti additives. *J. Alloy. Compd.*, 376:215, 2004. {89}
- [93] H.W. Brinks, M. Sulic, C.M. Jensen, and B.C. Hauback. TiCl₃-enhanced NaAlH₄: Impact of excess al and development of the Al_{1-y}Ti_y phase during cycling. *J. Phys. Chem. B*, 110:2740, 2006. {89}
- [94] A.G. Haiduc, H.A. Stil, M.A. Schwarz, P. Paulus, and J.J.C. Geerlings. On the fate of the Ti catalyst during hydrogen cycling of sodium alanate. *J. Alloy. Compd.*, 393:252, 2005. {91}
- [95] J.M. Colbe von Bellosta, W. Schmidt, M. Felderhoff, B. Bogdanović, and F. Schüth. Hydrogen-isotope scrambling on doped sodium alanate. *Angew. Chem. Int. Edit.*, 45:3663, 2006. {94}
- [96] G. Sandrock. A panoramic overview of hydrogen storage alloys from a gas reaction point of view. *J. Alloy. Compd.*, 293—295:877, 1999. {94}
- [97] S. Chaudhuri and J.T. Muckerman. First-principles study of Ti-catalyzed hydrogen chemisorption on an Al surface: A critical first step for reversible hydrogen storage in NaAlH₄. *J. Phys. Chem. B*, 109:6952, 2005. {94}
- [98] R.J. Borg and G.J. Dienes. *An Introduction to Solid State Diffusion*. Academic Press, Boston, 1988. {97}

- [99] F.A. Kroger. *The Chemistry of Imperfect Crystals*. North Holland, Amsterdam, 1964. {97}
- [100] Q. Shi, J. Voss, H.S. Jacobson, K. Lefmann, M. Zamponi, and T. Vegge. Point defect dynamics in sodium aluminum hydrides—A combined quasielastic neutron scattering and density functional theory study. *J. Alloy. Compd.*, 446-447:469, 2007. {97}
- [101] A. Borgschulte, U. Bösenberg, G. Barkhordarian, M. Dornheim, and R. Bormann. Enhanced hydrogen sorption kinetics of magnesium by destabilized $\text{MgH}_{2-\delta}$. *Catal. Today*, 120:262, 2007. {97, 114, 129, 140}
- [102] S. Singh, S.W.H. Eijt, M.W. Zandbergen, W.J. Legerstee, and V.L. Svetchnikov. Nanoscale structure and the hydrogenation of Pd-capped magnesium thin films prepared by plasma sputter and pulsed laser deposition. *J. Alloy. Compd.*, 441:344, 2007. {98, 113, 116, 124}
- [103] M. Felderhoff, K. Klementiev, W. Grunert, B. Spliethoff, B. Tesche, J.M. Belosta von Colbe, B. Bogdanović, M. Hartel, A. Pommerin, F. Schüth, and C. Weidenthaler. Combined TEM-EDX and XAFS studies of Ti-doped sodium alanate. *Phys. Chem. Chem. Phys.*, 6:4369, 2004. {98}
- [104] J.P. Perdew and Y. Wang. Accurate and simple analytic representation of the electron-gas correlation energy. *Phys. Rev. B*, 45:13244, 1992. {98}
- [105] J.P. Perdew, K. Burke, and M. Ernzerhof. Generalized gradient approximation made simple. *Phys. Rev. Lett.*, 77:3865, 1996. {98}
- [106] H.J. Monkhorst and J.D. Pack. Special points for brillouin-zone integrations. *Phys. Rev. B*, 13:5188, 1976. {99}
- [107] W.H. Bragg and W.L. Bragg. The reflection of x-rays by crystals. In *Proceedings of the Royal Society of London. Series A, Containing Papers of a Mathematical and Physical Character*, volume 88/Number 605, page 428. The Royal Society, 1913. ICSD database. {99}
- [108] C.G. Shull, E.O. Wollan, G.A. Morton, and W.L. Davidson. Neutron diffraction studies of NaH and NaD. *Phys. Rev.*, 73:842, 1948. {99}
- [109] X. Ke and I. Tanaka. Decomposition reactions for NaAlH_4 , Na_3AlH_6 , and NaH: First-principles study. *Phys. Rev. B*, 71:024117, 2005. {99, 103}
- [110] C.G. van de Walle and J. Neugebauer. First-principles calculations for defects and impurities: Applications to III-nitrides. *J. Appl. Phys.*, 95:3851, 2004. {99}

- [111] S.B. Zhang and J.E. Northrup. Chemical potential dependence of defect formation energies in GaAs: Application to Ga self-diffusion. *Phys. Rev. Lett.*, 67:2339, 1991. {99}
- [112] B.J. Kooi, A. van Veen, J.Th.M. de Hosson, H. Schut, A.V. Fedorov, and F. Labohm. Rectangular nanovoids in helium-implanted and thermally annealed MgO (100). *Appl. Phys. Lett.*, 76(9):1110, 2000. {108}
- [113] S.W.H. Eijt, J. de Roode, H. Schut, B.J. Kooi, and J.Th.M. de Hosson. Formation and stability of rocksalt ZnO nanocrystals in MgO. *Appl. Phys. Lett.*, 91:201906, 2007. {108}
- [114] C.V. Falub, P.E. Mijnders, S.W.H. Eijt, M.A. van Huis, A. van Veen, and H. Schut. Electronic structure and orientation relationship of Li nanoclusters embedded in MgO studied by depth-selective positron annihilation two-dimensional angular correlation. *Phys. Rev. B*, 66:075426, 2002. {108}
- [115] A.V. Sugonyako, D.I. Vainshtein, A.A. Turkin, H.W. den Hartog, and A.A. Bukharaev. Melting of sodium clusters in electron irradiated NaCl. *J. Phys.: Condens. Matter.*, 16:785, 2004. {108, 110}
- [116] M. Wagemaker, F.M. Mulder, and A. van der Ven. The role of surface and interface energy on phase stability of nano-sized insertion compounds. *Adv. Mater.*, 2009. accepted. {109}
- [117] D. Chen, X.L. Ma, and Y.M. Wang. First-principles study of the interfacial structures of Au/MgO(001). *Phys. Rev. B*, 75:125409, 2007. {109}
- [118] R. Gaudoin, W.M.C. Foulkes, and G. Rajagopal. Ab initio calculations of the cohesive energy and the bulk modulus of aluminium. *J. Phys.: Condens. Matter.*, 14:8787, 2002. {109}
- [119] S.J. Duclos, Y.K. Vohra, and A.L. Ruoff. High-pressure studies of NaH to 54 GPa. *Phys. Rev. B*, 36:7664, 1987. {110}
- [120] S.R. Elliott. *The Physics and Chemistry of Solids*. John Wiley & Sons, 1998. p.193. {110}
- [121] Y. Xie, J.S. Tse, T. Cui, A.R. Oganov, Z. He, Y. Ma, and G. Zou. Electronic and phonon instabilities in face-centered cubic alkali metals under pressure studied using ab initio calculations. *Phys. Rev. B*, 75:064102, 2007. {110}
- [122] U. Eberle, G. Arnold, and R. von Helmolt. Hydrogen storage in metal-hydrogen systems and their derivatives. *J. Power Sources*, 154:456, 2006. {113}

- [123] W. Grochala and P.P. Edwards. Thermal decomposition of the non-interstitial hydrides for the storage and production of hydrogen. *Chem. Rev.*, 104:1283, 2004. {113}
- [124] F. Schüth, B. Bogdanović, and M. Felderhoff. Light metal hydrides and complex hydrides for hydrogen storage. *Chem. Commun.*, 20:2249, 2004. {113}
- [125] S.V. Alapati, J.K. Johnson, and D.S. Sholl. Predicting reaction equilibria for destabilized metal hydride decomposition reactions for reversible hydrogen storage. *J. Phys. Chem. C*, 111:1584, 2007. {113}
- [126] R. Janot, F. Cuevas, M. Latroche, and A. Percheron-Guégan. Influence of crystallinity on the structural and hydrogenation properties of Mg_2X phases ($X=Ni, Si, Ge, Sn$). *Intermetallics*, 14:163, 2006. {113, 114}
- [127] O. Friedrichs, T. Klassen, J.C. Sánchez-López, R. Bormann, and A. Fernández. Hydrogen sorption improvement of nanocrystalline MgH_2 by Nb_2O_5 nanoparticles. *Scripta Mater.*, 54:1293, 2006. {114, 129}
- [128] T. Serikawa, M. Henmi, T. Yamaguchi, H. Oginuma, and K. Kondoh. Depositions and microstructures of Mg-Si thin film by ion beam sputtering. *Surf. Coat. Tech.*, 200:4233, 2006. {126}
- [129] K. Yoshimura, S. Nakano, S. Uchinashi, S. Yamaura, H. Kimura, and A. Inoue. A hydrogen sensor based on Mg-Pd alloy thin film. *Meas. Sci. Technol.*, 18(11):3335, 2007. {126}
- [130] B. Clemens. Thermodynamically tuned nanophase materials for reversible hydrogen storage: Structure and kinetics of nanoparticle and model system materials. DOE Annual Progress Report IV.A.4L, Stanford University, 2006. http://www.hydrogen.energy.gov/pdfs/progress06/iv_a_4l_clemens.pdf. {127}
- [131] M.J. Puska and R.M. Nieminen. Theory of positrons in solids and on solid surfaces. *Rev. Mod. Phys.*, 66:841, 1994. {127}
- [132] S. Jin, J. Shim, Y.W. Cho, and K. Yi. Dehydrogenation and hydrogenation characteristics of MgH_2 with transition metal fluorides. *J. Power Sources*, 172:859, 2007. {129}
- [133] L. Ma, P. Wang, and H. Cheng. Improving hydrogen sorption kinetics of MgH_2 by mechanical milling with TiF_3 . *J. Alloy. Compd.*, 432:LI, 2007. {129, 132, 135}

- [134] N. Recham, V.V. Bhat, M. Kandavel, L. Aymard, J.-M. Tarascon, and A. Rougier. Reduction of hydrogen desorption temperature of ball-milled MgH_2 by NbF_5 addition. *J. Alloy. Compd.*, 464:377, 2008. {129}
- [135] L. Xie, Y. Liu, Y.T. Wang, J. Zheng, and X.G. Li. Superior hydrogen storage kinetics of MgH_2 nanoparticles doped with TiF_3 . *Acta Mater.*, 55:4585, 2007. {129}
- [136] F.H. Ellinger, C.E. Holley, B.B. McInteer, D. Pavone, R.M. Potter, E. Staritzky, and W.H. Zachariasen. The preparation and some properties of Magnesium Hydride. *J. Am. Chem. Soc.*, 77:2647, 1955. {130, 140}
- [137] G. Vidal-Valat, J.-P. Vidal, C.M.E. Zeyen, and K. Kurki-Suonio. Neutron diffraction study of Magnesium Fluoride single crystals. *Acta Mater.*, B35:1584, 1979. {130, 140}
- [138] S. Fukada and M. Nishikawa. Semi-empirical equations for pressure-composition-temperature curves of the Ti-H system. *J. Alloy. Compd.*, 209:L23, 1994. {135}
- [139] U. Stuhr, D. Steinbinder, H. Wipf, and B. Frick. Hydrogen diffusion in f.c.c. TiH_x and YH_x : Two distinct examples for diffusion in a concentrated lattice gas. *J. Alloy. Compd.*, 310:190, 2000. {137}
- [140] H. Wipf, B. Kappesser, and R. Werner. Hydrogen diffusion in titanium and zirconium hydrides. *J. Alloy. Compd.*, 310:190, 2000. {137}
- [141] M. Wagemaker, A.P.M. Kentgens, and F.M. Mulder. Lithium transport for equilibrium between nano-crystalline phases in intercalated TiO_2 anatase. *Nature*, 418:397, 2002. {138}

List of publications

- S.Singh, S.W.H. Eijt, and F.M. Mulder, Grain refinement and deuterium vacancies in TiF_3 -catalyzed MgD_2 , *in preparation*.
- S.Singh, S.W.H. Eijt, Hydrogen vacancies facilitate hydrogen transport kinetics in sodium hydride nano-crystallites, *Phys. Rev. B*, 78(22):224110, 2008.
- S.W.H. Eijt, R. Kind, S. Singh, H. Schut, and W.J. Legerstee, R.W.A. Hendrikx, V.L. Svetchnikov, R.J. Westerwaal and B. Dam, Positron depth profiling of the structural and electronic structure transformations of hydrogenated Mg-based thin films, *J. Appl. Phys.*, 105(3): 043514, 2009.
- S. Singh, S.W.H. Eijt, J. Huot, W.A. Kockelmann, M. Wagemaker, and F.M. Mulder, The TiCl_3 catalyst in NaAlH_4 for hydrogen storage induces grain refinement and impacts on hydrogen vacancy formation, *Acta Mater.*, 55:5549, 2007.
- S. Singh, S.W.H. Eijt, M.W. Zandbergen, W.J. Legerstee, and V.L. Svetchnikov, Nanoscale structure and the hydrogenation of Pd-capped Magnesium thin films prepared by plasma sputter and pulsed laser deposition, *J. Alloy. Compd.*, 441:344, 2007.

About the author

arita was born on May 22, 1979 in Haridwar, India. From 1994 to 1997, she attended secondary school at Vidya Mandir Inter College, Haridwar. In 1997, she moved to Chandigarh to study pharmacy at the Government Polytechnic for Women, which she completed with honors in 1999. To pursue her interest in science, she joined the Government College for Girls of Panjab University in 1999, and graduated in 2002 with a Bachelor of Science degree. Starting from 2002, she studied at Indian Institute of Technology Madras, and received a Master of Science (MSc) degree in Physics in 2004. The MSc thesis was entitled HYDROGEN ABSORPTION AND DIFFUSION STUDIES IN $\text{Ti}_{0.1}\text{Zr}_{0.9}\text{CrFe}_{0.5}\text{Ni}_{0.5}$. She attended a summer program in physics at Raman Research Institute in Bangalore from May to June 2003. There, she conducted a project on lunar occultation with Prof. Dr. C.R. Subhramanyam at the department of Astronomy and Astrophysics.

As a visiting scientist, Sarita conducted research in Prof. Dr. H. Züchner's group at "*Institut für Physikalische Chemie*" within the International Graduate School of Chemistry in Münster for the period of October 2004 to December 2004. In March 2005, she joined the department of Radiation, Reactors & Radionuclides at Delft University of Technology as a PhD researcher. This thesis is a documentation of the research she performed under the guidance of Dr. S.W.H. Eijt and Prof. Dr. F.M. Mulder.

The global energy issues can be solved by the abundantly available hydrogen on earth. Light metals are a compact and safe medium for storing hydrogen. This makes them attractive for vehicular use. Unfortunately, hydrogen uptake and release is slow in light metals at practical temperature and pressure conditions. Catalysts are known to accelerate both processes. This book presents three mechanisms for catalyst actions: as grain refining agents, as a hydrogen vacancy formation facilitator, and (in its conventional role) as a hydrogen molecule splitter. Moreover, plentiful hydrogen vacancies are reported from experimental observations in nano-structured light metal hydrides. For specific storage systems, guidelines to select the optimal catalyst are developed based on the exploitable mechanisms.